UNIVERSITY OF LEEDS

The Electronic and Magnetic Properties of Thin Film Fe_3Sn_2

Callum Brennan-Rich

University of Leeds

School of Physics and Astronomy

Submitted in accordance with the requirements for the degree of

Doctor of Philosophy

January, 2026

This thesis is dedicated to my grandparents.
And to my lab partner, Tom, who will never get the chance to read it.
Step by step, the longest march.

Intellectual Property Statement

The candidate confirms that the work submitted is his own and that appropriate credit has been given where reference has been made to the work of others.

This copy has been supplied on the understanding that it is copyright material and that no quotation from the thesis may be published without proper acknowledgement.

The right of Callum Brennan-Rich to be identified as Author of this work has been asserted by him in accordance with the Copyright, Designs and Patents Act 1988.

Acknowledgements

I would like to thank my supervisors, Christopher Marrows, Sean Collins and Rik Drummond-Brydson whose guidance and patience have been more valuable than words can describe.

Specific thanks should also be given to Professor Gavin Burnell for his assistance in setting up Conda environments, Dr Mannan Ali for his expertise in repairing sputter deposition systems and both of the above for all the experimental and theoretical advice they have provided over the years. Dr Philippa Shepley and Dr Matthew Rodgers are due their credit as experimental officers, as no work in this thesis would have been possible without their diligence.

Along with them, fruitful advice and guidance has been provided by every academic (along with many postdoctoral researchers and PhD students) from the University of Leeds Condensed Matter Physics research group.

Finally, my deepest thanks is also extended to the academics and staff of the Leeds Electron Microscopy and Spectroscopy centre, specifically Dr Zabeada Aslam, Dr Stuart Micklethwaithe and Professor Andrew Brown.

Abstract

This thesis is an exploration of the growth and properties of thin film Fe_3Sn_2. Through precise stoichiometric deposition, this frustrated kagome ferromagnet can be grown with minimal impurities and intergrowths from the other Fe-Sn intermetallic alloys. The frustrated spin texture within the Fe_3Sn_2, and the reorientation these spins undergo with changes of field and temperature, have been predicted to produce the spin frustration needed to stabilise magnetic skyrmions. These skyrmions in turn have potential applications in new architectures for magnetic data storage and the development of neuromorphic computing. Beyond this, the electronic band structure of Fe_3Sn_2 is predicted to have many novel properties such as flat bands and Dirac-points within tantalising reach of the Fermi surface. The resulting contribution to the anomalous Hall effect as well as unique magnetoresistance curves could also feature in future spintronic devices in order to improve the energy efficiency of our already highly optimised computation methods.

To begin, high quality 80 nm to 100 nm epitaxial films of Fe_3Sn_2 are fabricated through sputter deposition on to heated single crystal sapphire substrates with a seed layers of epitaxial Pt. Using X-ray diffraction these films were found to be strongly orientated in the (001) direction with large 30 nm grain sizes. Scanning transmission electron microscopy, combined with a custom phase matching technique, allows for spatial maps of these thin films to be produced covering 100s of nm of the film's cross section and with spatial resolution of 3 nm by 3 nm. This large scale crystal characterisation confirms the ability to control the phase content of the ferromagnetic Fe_3Sn_2 and the antiferromagnetic FeSn through the growth process. The ratio of power fed to the Fe and Sn magnetron guns alone, as opposed to temperature or growth rate, is found to be the determining factor that changes the resulting film composition, due to the precise control of growth rate that can achieved from each gun, that can then in turn lead to specific stoichiometries in the resulting films.

The highly pure, with over 97% crystalline content, Fe_3Sn_2 films were found to have saturation magnetisation of 777 emu/cm^3 $\pm$ 9 emu/cm^3 and very soft coercivity of 1.5 mT $\pm$ 0.2 mT. Analysis of the magnetic properties of the resulting films showed expected reduction in saturation magnetisation with increasing FeSn intergrowth, but an unexpected minima behaviour in the coercivity of highly

mixed Fe_3Sn_2 and FeSn film with changing temperature, indicating a strong ferromagnetic-antiferromagnetic coupling. Fitting to the Bloch-$\frac{3}{2}$ law allows a spin wave stiffness of $(4.1 \pm 0.2) \times 10^{-40}$ J/m^2 to be extracted. Further high temperature measurements reveal that a temperature of 750 K results in the Fe_3Sn_2 irreversibly breaking down, which in turn causes the appearance of a hitherto unseen magnetic transition at 120 K in the ZFC/FC measurements.

The electronic properties of ultra-thin 5nm thick Fe_3Sn_2 films are also explored, with surprisingly no orbital contribution to the anomalous Hall effect observed despite being strongly suggested in the literature. Instead, a carrier type change-over is confirmed by the change of sign of the ordinary Hall effect at 75 K. This critical temperature was found to correspond closely to the point of spin reorientation and an observed change in the scaling of the anomalous Hall effect. Along with this, a linear negative magnetoresistance that is observed to have its gradient decrease with increasing temperature is observed, with currently no established theoretical explanation with potential applications of such consistent linear magnetoresistance being part of the detector system in a high field magnetic sensor.

Contents

Abbreviations

AC	Alternating Current	AFM	Atomic Force Microscopy
AHE	Anomalous Hall Effect	ALD	Atomic Force Microscopy
ANE	Anomalous Nernst Effect	ARPES	Angle-Resolved Photoemission Spectroscopy
DC	Direct Current	DMI	Dzyaloshinskii-Moriya Interaction
DoG	Difference of Gaussians	DoS	Density of States
EDXS	Energy Dispersive X-ray Spectroscopy	FC	Field Cooled
FFT	Fast Fourier Transform	FIB	Focused Ion Beam
FM	Ferromagnet	FQH	Fractional Quantum Hall
FWHM	Full Width at Half Maximum	HAADF	High Angle Annular Dark Field
IP	In-Plane	IPA	Isopropyl Alcohol
IPHE	In-Plane Hall Effect	LAADF	Low Angle Annular Dark Field
LEMAS	Leeds Electron Microscopy And Spectroscopy centre	MBE	Molecular Beam Epitaxy
MR	Magnetoresistance	OHE	Ordinary Hall Effect
OOP	Out-Of-Plane	PED	Precession Electron Diffraction
RRR	Residual Resistivity Ratio	SQUID	Superconducting Quantum Interference Device
STEM	Scanning Transmission Electron Microscopy	TEM	Transmission Electron Microscopy
UHV	Ultra High Vacuum	VSM	Vibrating Sample Magnetometer
VTI	Variable Temperature Insert	XRD	X-Ray Diffraction
XRR	X-Ray Reflection	ZFC	Zero Field Cooled

Chapter 1

Introduction

When the work on this thesis began in 2021, humanity was emerging from a pandemic that had lasted two years and killed 5.2 million people [1]. These direct mortalities, as well as the associated measures the world took to mitigate there being more, were predicted to have long term impacts on the economy, education and society for the coming decades [2]. Many of these effects are no doubt present, but tangibly the world before and after the pandemic does not seem that drastically different.

In 2022 a reasonably small company called OpenAI released a chatbot called ChatGPT. History has yet to vindicate this view, but I believe that this development will be as significant to humanity as Johannes Gutenberg's invention of the printing press. In just a few months, ChatGPT, and other similar generative AI systems, had reached more than 100 million users [3, 4] and as of 2025, it has become the fifth most visited website on the internet [5] with over 5 billion visits a month. These generative AIs have already found their way into industry, with one survey showing 71% of businesses now use an AI as part of one of their services [6], with sectors such as health care, financial services, and educational technology already being heavily influenced [7].

This advancement comes saddled with an associated cost. The training and the implementation of these AIs are likely to be consuming massive amounts of electricity, with the exact amount not currently being disclosed by companies like Microsoft and Google [8]. Rough estimates for ChatGPT alone put the electricity consumption in the region of 40 million kWh a day [9] which would make a ChatGPT nation the 95th most power consuming country in the world (roughly the same energy consumption as Slovenia). Along with the direct power supply, there is also an associated expense of fresh water that is required to cool the data centres during use [10, 11], which is predicted to be roughly 5 billion cubic metres of water per annum by 2027, or approximately half the water consumption of the entire UK [12].

Methods and materials that offer the possibility of reducing the energy wastage in electrical devices would both offer a reduction in direct energy cost, and a reduction in water required to cool the waste heat that is produced. Spintronics, a portmanteau of spin and electronics, aims to use both the spin and the charge of the electron as a method of information transport [13], and in doing so, create these high efficiency devices. This field has brought us Giant Magnetoresistance [14], Tunnel Magneto Resistance [15], and Magnetic Random Access Memory [16] which have all contributed to the development of more efficient data storage devices [17]. In more recent years, there has also been a push towards "neuromorphic" computing [18] which aims to emulate the complex and evolving interplay that neurons in the brain use to make highly

efficient calculations.

It is interesting to be able to observe these spintronic effects in the bulk material, i.e. when the material samples' dimensions are so large that the material can effectively be treated as having infinite extent, but this is often not very conducive for an application in industry [19]. There, smaller devices down to the nano-scale are preferred due to their ability to be integrated into highly compact electronics that have become the standard in computer engineering. This means that it is of key interest to keep exploring spintronic and quantum materials in a thin film form [20]. The search is always active for new materials that can demonstrate unique spin-orbit, anomalous, spin texture based properties. A new candidate for these effects, that has become a focus of recent flurry of publications, is the kagome ferromagnet Fe_3Sn_2.

1.1 Thesis Outline

The work that this thesis reports had one aim, that being, the production and measurement of high-quality thin films of Fe_3Sn_2 and the measurement of their magnetic and electronic properties.

As was discovered over the course of this work, producing phase pure Fe_3Sn_2 offers a significant challenge in and of itself.

In chapter 2 a brief theoretical overview is provided of magnetism, magnons, domain walls, and magnetic skyrmions. A literature review is provided covering what is currently known about the crystallographic, magnetic and electronic properties of Fe_3Sn_2 and the closely related alloy, FeSn.

In chapter 3 the experimental methods used to produce the work in this thesis are discussed. A brief overview of the principles behind the techniques is explained and then the methods of analysis used are described.

In chapter 4 the reader will find the growth and characterisation of three thin films with composition varying from pure FeSn to pure Fe_3Sn_2. Evidence of the films' crystallographic quality is provided using standard X-ray measurements as well as indications of phase purity through the use of Scanning Transmission Electron Microscopy (STEM).

In chapter 5 the magnetic properties of the same three films in chapter 4 are reported, showing distinct magnetisations and coercivity behaviours. The potential influence of the crystallographic structures and their qualities discovered in chapter 4 are discussed in relation to these results.

In chapter 6 ultra thin films of Fe_3Sn_2 have their transport properties reported. Longitudinal

and transverse magnetoresistance measurements are shown for a range of temperatures and a carrier type change indicating a potential novel band structure is reported.

Finally, in chapter 7, all previous results are summarised and a possible future for this work is discussed.

1.2 Credit and Acknowledgement

In this thesis, the work attributed solely to the author was all sample depositions, sample optimisations, X-ray measurement and characterisation, loading and operation of the vibrating sample magnetometer and cryostat, as well as analysis and data selection of all TEM and STEM data included. Initial growth parameters were suggested by N. Satchell with reference to the work of D. Hong [21]. STEM measurements were performed in collaboration with S.M. Collins, Z. Aslam and A.P. Brown from the Leeds Electron Microscopy and Spectroscopy centre (LEMAS) with lamella preparation performed by S. Micklethwaite, also of LEMAS. Aberration-corrected TEM measurements were performed by T. Almeida at the University of Glasgow. All clean room optimisation and fabrication was performed by the author, with assistance in the ion milling step provided by R. Gilroy of the Leeds Nanotechnology Cleanroom.

Figures that are not the author's own work are described as either "reproduced", indicating an exact copy from the source, "adapted from", indicating some slight alterations to layout or labelling have been made to improve legibility, or "inspired by", which indicates the original concept for a diagram can be found in the referenced source, but significant development has been provided by the author.

[20] [22] [23] [24] [25]

Chapter 2

Theory and Literature Review

2.1 Introduction

In this chapter an introduction to the theory of magnetism is provided. The theory of ferromagnetism and antiferromagnetism is discussed first in general and then with a specific eye towards the Fe-Sn intermetallic magnets. Also accompanying this is a detailed discussion of current experimental and theoretical research in the literature as well as highlighting which underdeveloped areas this thesis intends to go some small way toward filling.

The theory of magnetism (as well as a broad overview of condensed matter physics) is discussed in the books of S. Simon [26]; N. Ashcroft and N. Mermin [27]; and C. Kittel [28]. An in depth focus on magnetism is provided by the book of S. Blundell [29] and a solid basis for the quantum mechanics required can be found in the book of J. Binney and D. Skinner [30].

2.2 Magnetism

Magnetism and its associated phenomena are the clearest manifestations of the quantum nature of our world. The Bohr-van Leeuwen theorem (independently developed by both Niels Bohr and Hendrika van Leeuwen in the 1910s) tells us that classical statistical mechanics forbids any system from having a net magnetisation. If this were true then ferromagnets, those materials that have some magnetisation in the absence of any external field, would certainly not exist. Along with them, paramagnets, materials that gain a magnetisation in the direction of an applied field, and diamagnets, those materials that gain a magnetisation opposing an external field, would also not be possible. To avoid such a contradiction to reality, quantum mechanics has to be introduced.

2.2.1 The Exchange Interaction

In general, if we want to describe a multi-particle system, we write the resulting wavefunction as a tensor product of the single particle wavefunctions. For example, for the two particle state of particles A and B, we could write:

$$|\psi\rangle = |\phi_{\mathrm{A}}\rangle \otimes |\phi_{\mathrm{B}}\rangle = |\phi_{\mathrm{A}}\phi_{\mathrm{B}}\rangle \,. \tag{2.1}$$

where $|\psi\rangle$ is the overall wavefunction, $\phi_{\mathrm{A,B}}$ are the wavefunctions of the particles A and B, and $\otimes$ indicated the tensor product between the two. However, it is not obvious that all products of the one particle states can lead to a valid two particle state, especially when both particles

are indistinguishable from each other. In this situation, if we consider the application of the exchange operator, $\hat{\boldsymbol{P}}$, whose action is to exchange the real space locations of these identical particles with each other, then it is apparent that there can have been no overall change to any observable associated with the wavefunction (i.e. the wavefunction only gains a phase under the action of this operator). Applying the operator twice should just return us to the initial wavefunction. It therefore follows that:

$$\hat{\boldsymbol{P}}\left|\psi\right\rangle = e^{i\theta}\left|\psi\right\rangle \text{ and } \hat{\boldsymbol{P}}^2\left|\psi\right\rangle = e^{2i\theta}\left|\psi\right\rangle = \left|\psi\right\rangle. \tag{2.2}$$

Since we know $e^{2\pi i} = 1$ we can immediately conclude that the eigenvalues of the exchange operator are ± 1. This means any multi-particle wavefunction of identical particles has to either be symmetric (eigenvalue 1) or antisymmetric (eigenvalue -1) under the action of the exchange operator.

For the case of fermions, the spin statistics theorem says that their wavefunction must always be antisymmetric, but we should also consider that a wavefunction is made up of the product of a spatial and spin component. For an $S = \frac{1}{2}$ particle like the electron, there are four possible direct product states with spin ups and downs symbolised by $\left|\uparrow\uparrow\right\rangle, \left|\uparrow\downarrow\right\rangle, \left|\downarrow\uparrow\right\rangle, \left|\downarrow\downarrow\right\rangle$. We can observe that the first and the last are symmetric under exchange, but for the middle two, a superposition is required. Depending on choice of how we superimpose we can either create a third symmetric state (that with the other two is known as the spin-triplet) or the antisymmetric state which is known as the spin-singlet:

$$\begin{aligned}
\left|\chi_T\right\rangle &= \begin{cases} \left|\uparrow\uparrow\right\rangle & s = 1 \\ \frac{\left|\uparrow\downarrow\right\rangle\left|\downarrow\uparrow\right\rangle + \left|\downarrow\uparrow\right\rangle\left|\uparrow\downarrow\right\rangle}{\sqrt{2}} & s = 0 \\ \left|\downarrow\downarrow\right\rangle & s = -1 \end{cases} \\
\left|\chi_S\right\rangle &= \frac{\left|\uparrow\downarrow\right\rangle\left|\downarrow\uparrow\right\rangle - \left|\downarrow\uparrow\right\rangle\left|\uparrow\downarrow\right\rangle}{\sqrt{2}} \quad s = 0.
\end{aligned} \tag{2.3}$$

Our total antisymmetric wavefunction can then be written as:

$$\begin{aligned}
\left|\Psi_S\right\rangle &= \frac{\left|\phi_{\mathrm{A}}(\boldsymbol{x})\phi_{\mathrm{B}}(\boldsymbol{x'})\right\rangle + \left|\phi_{\mathrm{A}}(\boldsymbol{x'})\right\rangle\left|\phi_{\mathrm{B}}(\boldsymbol{x})\right\rangle}{\sqrt{2}}\left|\chi_S\right\rangle \\
\left|\Psi_T\right\rangle &= \frac{\left|\phi_{\mathrm{A}}(\boldsymbol{x})\phi_{\mathrm{B}}(\boldsymbol{x'})\right\rangle - \left|\phi_{\mathrm{A}}(\boldsymbol{x'})\right\rangle\left|\phi_{\mathrm{B}}(\boldsymbol{x})\right\rangle}{\sqrt{2}}\left|\chi_T\right\rangle
\end{aligned}, \tag{2.4}$$

where we have paired the symmetric spatial wavefunction with the antisymmetric spin wavefunction and vice versa to ensure the total antisymmetry is preserved. The singlet state above

has $\boldsymbol{x} = \boldsymbol{x'}$ as a completely valid choice for the spatial coordinates, implying the particles can be arbitrarily close to each other provided their spins are antisymmetric. The triplet however would vanish to 0 if $\boldsymbol{x} = \boldsymbol{x'}$ and so in general the particles in a spin triplet will avoid each other's proximity. If the $S = \frac{1}{2}$ particle were a neutron, then this is where the story ends. However, for charged particles like the electron we find that the restrictions put on the spatial wavefunction often have a very significant effect acting to (generally) push the Coulomb energy of the spin singlet state higher than the spin triplet. If we imagine many such interacting electrons, that all have the same exchange energy and are also physically locked to a particular position, we can capture this interaction qualitatively using the Heisenberg Hamiltonian [26]:

$$\boldsymbol{H} = -\frac{1}{2} \sum_{\langle i,j \rangle} J \, \boldsymbol{S}_i \cdot \boldsymbol{S}_j \, , \tag{2.5}$$

where J is the exchange interaction energy and $\boldsymbol{S_i}$ represents the angular momentum on site i (it is important to note that although almost universally notated as "$\boldsymbol{S}$", this term will in the case of electrons orbiting atoms also contain contributions from the orbital angular momentum $\boldsymbol{L}$). The summation is being performed over all i,j that are neighbours to each other, indicated by the chevroned brackets. This Hamiltonian captures the idea that there will be some energy reduction from having $\boldsymbol{S}_i$,$\boldsymbol{S}_j$ aligned and an energy increase in having them anti-aligned, provided that J is a positive number. In some systems, J is in fact negative and in this case anti-alignment, i.e., antiferromagnetism is preferred.

If all systems obeyed this maxim perfectly then the world would be full of spin-triplets all perfectly aligning their moments with each other and ferromagnets would abound. We know in reality that only three elements are ferromagnetic (at room temperature): Fe, Co and Ni. A simple argument that complicates things is shown in Figure 2.1 where we see that the combination of two atomic potentials (modeled as infinite potential wells) containing an electron each will cause these spins to anti-align if the electrons are allowed to spread their wavefunction over both atoms evenly. An even further complication comes from the itinerant (moving) nature of these spins as the electrons providing them are often free to flow through crystal structures they inhabit if the magnetic material is a metal.

It was the work of Edmund Stoner [31] that first showed that a spontaneous magnetisation could form in a material provided that the energy reduction from the exchange interaction aligning the spins was greater than energy gain from the increase in kinetic energy that having an imbalance of spin up and spin down produces. The famous Stoner criterion is:

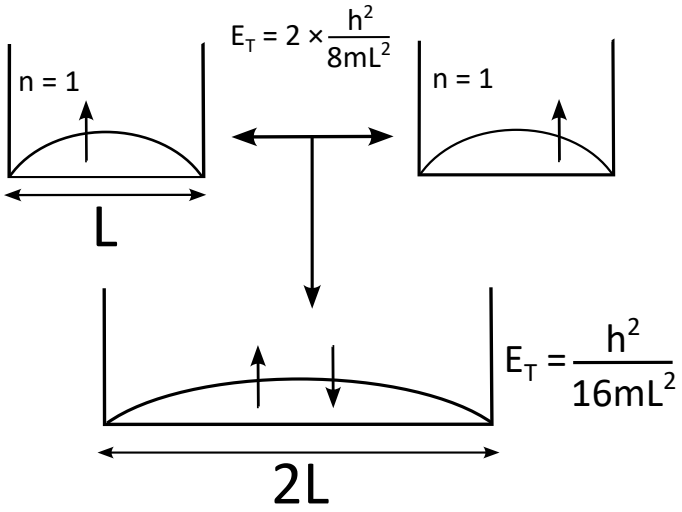

Figure 2.1: Toy model for the formation of a covalent bond between two atoms. Allowing the electron to delocalise across both atomic sites (represented as infinite potential wells) causes a reduction in energy but also causes both electrons to anti-align their spins so they can occupy the degenerate ground state. This argument is taken from the book of S. Blundell [29].

$$JD(E_{\mathrm{F}}) > 1, \tag{2.6}$$

where J is the exchange interaction energy per unit volume and $D(E_F)$ is the Density of States (DoS), the number of states per energy per volume at the Fermi surface. At room temperature, only the aforementioned Fe, Co and Ni have sufficiently high DoS and exchange interaction to be naturally ferromagnetic. Some elements such as Pt are very close to satisfying the Stoner criterion and so in the presence of a ferromagnet will actually gain a proximity magnetisation themselves. This magnetisation and its relevance in this work is calculated in section 4.3.

2.2.2 Domains, Domain Walls and Hysteresis

Even when we find lumps of iron containing minerals in nature, it is very rare for these to have an overall net magnetisation. The basic reason for this is that the energy stored in an external magnetic field is proportional to the strength of that magnetic field squared. At some point, it may become more energetically favourable for the moments within a material to not align with each other (sacrificing the stability they gained from the exchange interaction) if this will in turn reduce the overall magnetic field strength. This leads to the development of regions

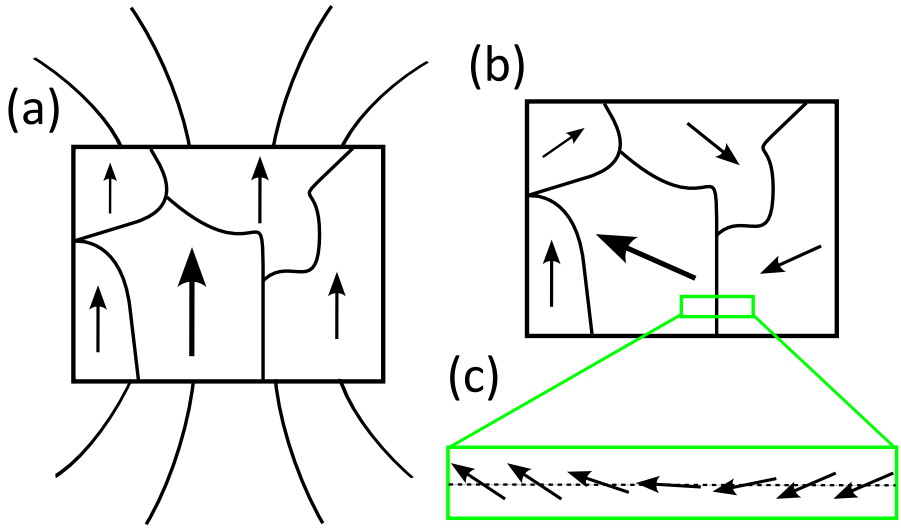

Figure 2.2: Illustration of (a) a magnetised sample in which all the domains are aligned to produce an external magnetic field (b) a sample in which the domains have relaxed into an arrangement that produces no net external magnetic field and (c) a zoomed in view of the domain wall between domains. It is worth noting a domain wall width will typically be many hundreds of atoms.

within a material called domains. Within a domain, the exchange interaction is dominant and all the moments more or less align. The sample overall, however, may be made of millions of domains that do not align with each other. The regions between domains, called domain walls, are places where moments will gradually re-orientate over many hundreds of atoms to transition from one domain's direction to another. A simplified illustration is shown in Figure 2.2. It is worth noting that although the domain shapes and sizes remain the same between (a) and (b) in the figure, this is not necessarily the case. When an external magnetic field is applied to a sample, domains will often grow or shrink and the corresponding domain walls will sweep through the sample (unless something like a crystal defect happens to pin them to a specific site). The dynamics of domain walls, including their ability to be manipulated by current, temperature gradient and mechanical stress, is a topic entirely to itself. For a review of this topic focusing on its use for data storage see the review article of S. Parkin [32].

This behaviour is key to understanding the features of a magnetic hysteresis loop. When a strong magnetic field is applied to any material we would expect this to dominate any internal interactions and produce a (more or less) uniformly magnetised state with all the moments aligned. At this point, there are no more available moments to be aligned with the field and so

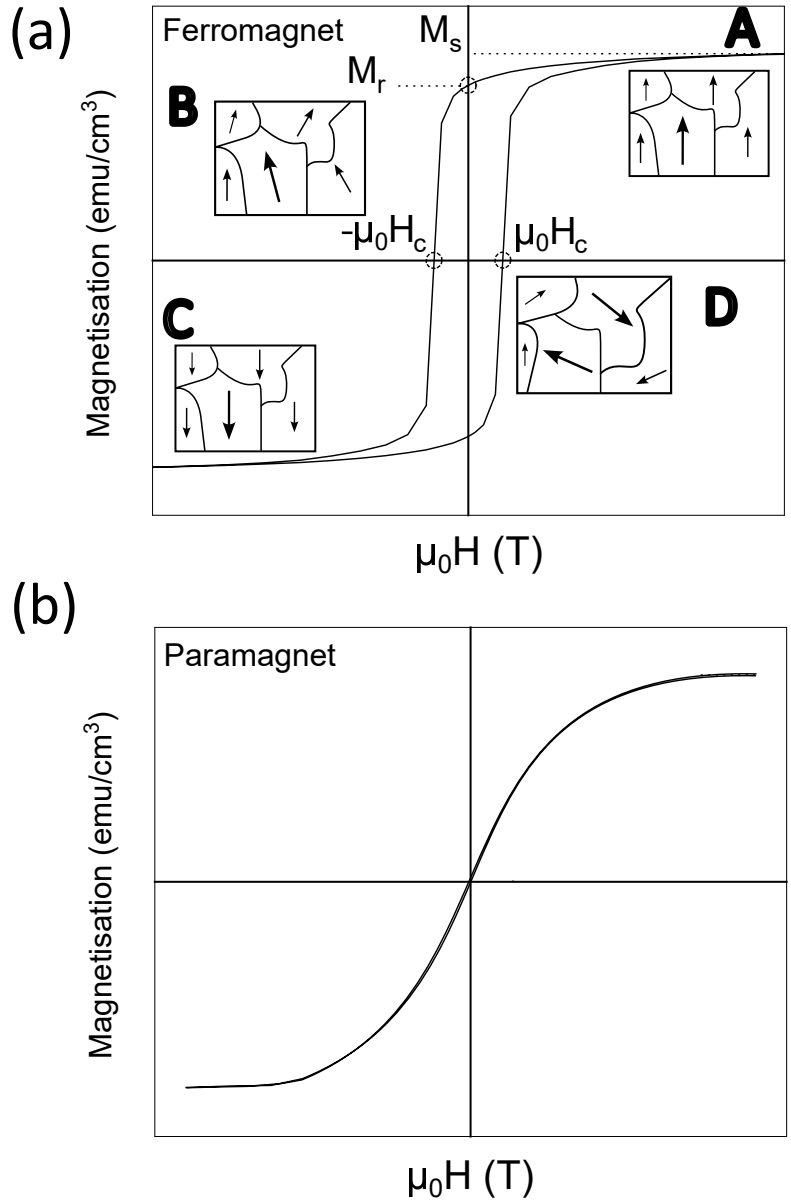

Figure 2.3: A diagram of (a) a ferromagnetic hysteresis loop showing the key features. Starting at A, the fully saturated state, a reduction in external magnetic field introduces some magnetic disorder and a corresponding reduction in magnetisation until we reach B, the remanent magnetisation in no external field. If the external magnetic field is large and negative we reach the saturated state in the opposite direction at point C. The label D indicates the intermediate state where the external magnetic field opposing the magnetisation has just introduced enough disorder to result in zero net magnetisation. In (b) there is the paramagnetic response in which no hysteresis can be observed.

we have reached what is called the saturation magnetisation M_s, where any further magnetic field will not increase the sample's magnetic moment further. If the external field is then reduced back to zero at a temperature below the Curie temperature, some of these aligned domains will remain aligned and so the material will maintain some remanent magnetisation M_r. If the external field direction is reversed, it will take some finite magnetic field to begin reorientating and changing the size of the domains to reduce the magnetisation of the sample back down to zero which is known as the coercive field $\mu_0 H_c$.

The Curie temperature, as mentioned above, is the temperature above which a material loses its ferromagnetic properties. According to the model proposed by Weiss [33], we should think of each moment in a ferromagnet experiencing a net magnetic field from all the moments that surround it. Then, as thermal agitation is introduced (generally causing some non-zero percentage chance for a given moment to flip direction), this overall molecular field will reduce in strength until eventually becoming insufficient to maintain a fixed direction for our considered moment. Since this argument applies across all moments in the sample, they have all lost their coherence and no net magnetisation remains.

2.2.3 Magnons and the Bloch-$\frac{3}{2}$ Law

In a crystal, excited lattice vibrations are known as phonons [28]. If these phonons are acoustic and described by the dispersion relation:

$$\omega = ck = \frac{2\pi c}{\lambda}\,, \tag{2.7}$$

where ω is the phonon's frequency, k is its wavevector, and λ is its wavelength, then it should hopefully be clear that it requires arbitrarily small energy above $T = 0$ K to excite an arbitrarily large wavelength phonon.

In an analogous way, at $T = 0$ K all the moments of a ferromagnet will align with each other but if any thermal energy is introduced, it will act to flip the moments and we can think of this as a boson called a magnon [29]. It is worth noting that this flipping should be thought of as a single flipped moment that then due to interatomic transport can delocalise across many atoms, which is distinctly different from large regions of uniformly orientated moments that make up a domain.

If we start with the Heisenberg Hamiltonian in equation 2.5, then for a one-dimensional chain, with the initial assumption that $T = 0$ K it is possible to write:

$$\boldsymbol{H} = -\sum_i J\left(\mathrm{S}_i^z\mathrm{S}_{i+1}^z + \frac{1}{2}(\mathrm{S}_i^+\mathrm{S}_{i+1}^- + \mathrm{S}_i^-\mathrm{S}_{i+1}^+)\right) , \tag{2.8}$$

where we have made use of the fact that on a one-dimensional chain all the interactions are contained in the sum between the spin S_i and the spin S_{i+1}. If we consider the action of this Hamiltonian on the ground state $|0\rangle$ where all the spins align, it's clear the lowering operators in the 2nd and 3rd term of 2.8 will reduce these terms to 0 and so all that is left is the N spins of the chain each returning the eigenvalue S^2 from the first term leading to the energy eigenvalue $E_0 = -NS^2J$. If we now consider the state $|n\rangle$ which we will define as the ground state, but where the n^{th} spin has been flipped, it is possible to see that the lowering operators will now have a chance to return a non-zero contribution (and the associated neighbour raising operator will lift that state) leading to:

$$\boldsymbol{H}\,|n\rangle = (-NS^2J + 2SJ)\,|n\rangle - SJ\,|n+1\rangle - SJ\,|n-1\rangle \ . \tag{2.9}$$

It is clear that $|n\rangle$ is not an eigenvalue of the Hamiltonian. In order to progress, we can move into momentum space and look at the Fourier series on $|n\rangle$ defined as:

$$|n\rangle = \frac{1}{\sqrt{N}}\sum_k e^{-ikx_n}\,|k\rangle \ . \tag{2.10}$$

Substituting this in, and remembering that in real space $x_{n+1} = x_n + a$ (where a is the lattice constant of the chain), we can show with some algebra that the dispersion relation is given by:

$$E = -NS^2J + 2SJ - SJe^{-ka} - SJe^{ka} , \tag{2.11}$$

where this first term is the ground state energy eigenvalue as mentioned above. Taylor expanding these exponentials we can find the low k excitations from the ground state go as:

$$E = Dk^2 , \tag{2.12}$$

where $D = SJa^2$, is known as the exchange interaction stiffness or spin wave stiffness. A lot of assumptions have already gone into extracting this result, but it is actually remarkably robust so long as the material supports plane wave solutions allowing for the substitution 2.10. Neutron spectroscopy measurements have confirmed a quadratic dispersion relation exists in Fe_3Sn_2 [34], providing evidence that this theory so far is at least a reasonable approximation. Now, since each magnon reduces the total overall moment, it's possible to relate the magnetisation,

M, related to the number of magnons n with:

$$M = \frac{g\mu_B}{V}(NS - n)\,, \tag{2.13}$$

where g is the g-factor, μ_B is the Bohr magneton, and V is the total volume.

Since we have the dispersion relation 2.12 we can use the DoS as well as Bose-Einstein statistics to write:

$$n = D\left(\frac{k_B T}{\hbar}\right)^{\frac{3}{2}} \int_0^\infty \frac{x^{\frac{1}{2}}}{e^x - 1} dx\,, \tag{2.14}$$

where the integral evaluates to ≈ 0.678. Here, we have shifted from a one-dimensional initial model to a three-dimensional density of states. This can be easily justified since the dispersion relation 2.12 is actually independent of dimension, but in reality we actually want to model three-dimensional magnets. Combining 2.13 and 2.14 we can conclude that the magnetisation goes as:

$$M = M_0(1 - bT^{\frac{3}{2}})\,, \tag{2.15}$$

which is known as the Bloch-$\frac{3}{2}$ law. It is worth noting that three major assumptions have gone in to producing this result. The first, that being the existence of plane wave solutions that lead directly to the quadratic dispersion relation, has already been mentioned as being remarkably robust across many different materials. The second, the implicit assumption of isotropy is weaker and often adjustments might need to be made to consider the exchange interaction stiffness along different crystallographic axis. The third, and most important, is that these calculations rely on low temperature linear excitations of the magnon spectrum. At temperatures above about a third of a material's Curie temperature ($\frac{T_C}{3}$) effects like magnon-magnon interactions will significantly alter the magnetisation curve, so equation 2.15 should be seen as a low temperature expansion only.

2.2.4 Electron-Magnon Scattering

The effect of introducing a magnetic field to the Hamiltonian 2.8 is to eventually produce a gapping in the dispersion relation 2.12, which in turn results in a reduction in the magnon population density integral 2.14 for increasing field strength. It can be intuited that a higher magnetic field will therefore reduce the number of magnon-electron scattering events that happen in a ferromagnet, and produce a negative Magnetoresistance (MR). This is a large simplification, and in practice the theoretical calculations for a real $3d$ ferromagnet require

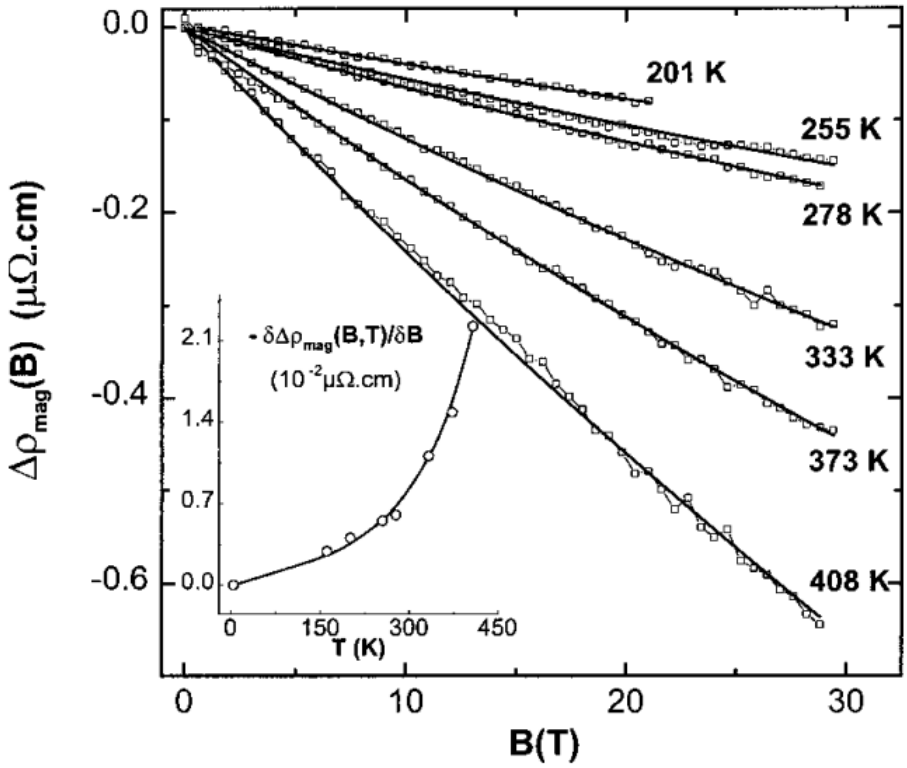

Figure 2.4: Change in resistivity in an 80 nm Fe thin film under a magnetic field over a range of temperatures. The inset shows the difference between the experimental and theoretically predicted slopes in the linear high field region. Reproduced from the work of B. Raquet *et al.* [35].

considerations of interband diffusion and magnon mass renormalisation which is presented in the work of B. Raquet *et al.* [35]. Figure 2.4 shows the change in resistivity with field across a range of temperatures for a Fe sample, providing evidence for the intuition above, that a higher magnetic field will suppress magnon-electron scattering events, and therefore decrease the resistivity of the ferromagnet. Reports of negative MR are present for Fe_3Sn_2 with a particularly distinct work being that of N. Kumar *et al.* [36] which measures the MR of single crystals of Fe_3Sn_2 along different crystal orientations. They report a competition between the regular Lorentz MR which is quadratic and positive and a linear negative MR which they associate with magnon suppression as described by B. Raquet.

2.2.5 Frustration

Frustration in a material is the situation in which the magnetic moments cannot simultaneously minimise the energies associated with each of their interactions. The simplest example would be 1D chain of moments in which nearest neighbours experience a ferromagnetic exchange and the next nearest neighbours experience an antiferromagnetic exchange. This would be described as frustration arising from competing interaction; a slightly more subtle example would be the geometric frustration that can arise due to the structure of the underlying crystal lattice. The classic example is the triangular lattice (or the Kagome structure discussed in 2.3). For moments arranged on a lattice of triangles, such that each moment experiences antiferromagnetic nearest neighbour interactions, no orientation can be provided that will anti-align all three spins on the triangle simultaneously. This means that some compromising frustrated state ends up forming that attempts to minimise the overall total of the interaction energy while each individual moment is itself not minimised.

To formalise this concept of frustration further, the concepts of symmetry and order parameters have to be invoked. As a general rule, if the symmetry of a magnetic system does not forbid a non-collinear alignment (alignment along a single axis, whether that is ferromagnetic or antiferromagnetic) in the ground state, then frustration of some magnitude will be present in the magnetic structure.

2.2.6 Skyrmions

Skyrmions, originally named after Tony Skyrme who proposed a topological solution to pion fields in particle physics [38], are a quasi-particle that can exist within the spins in a magnetic material (the arrangement of these spins is often called the "magnetic texture" of the material). The most simple magnetic texture has already been discussed in the preceding section, the situation where all moments align with each other in a given region which could be called topologically flat.

In Figure 2.5 we see three examples of spin textures on a 1D chain of spins. The first is the flat case as mentioned and the second, although appearing twisted at first glance, is actually also topologically flat as this twisting can be unwound through an anti-clockwise rotation of all the central spins. The third example does have a non trivial topology as the rotation cannot be unwound. Any attempt to rotate the central spin will only act to push the twist along the chain (a clockwise rotation will shift the texture left, an anticlockwise rotation will shift the texture right). Only by breaking the exchange interaction and forcing two spins to

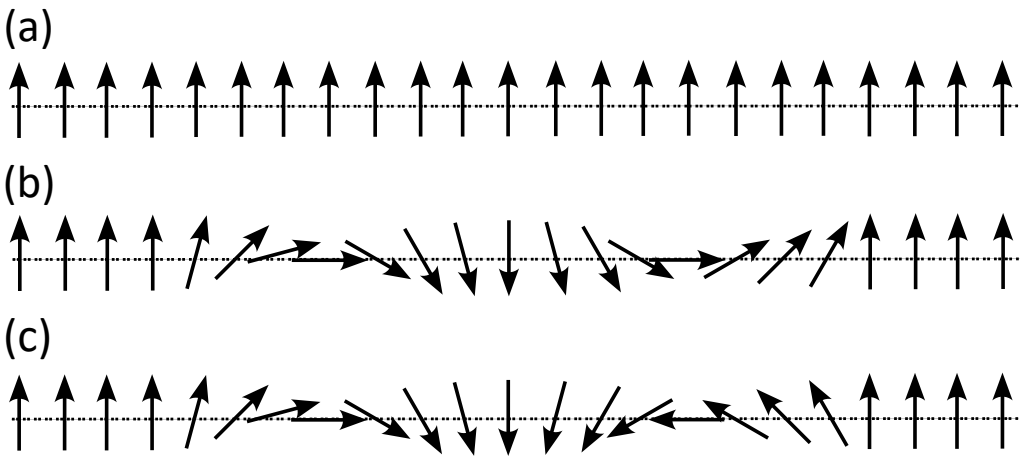

Figure 2.5: Spin textures in 1D. (a) a topologically trivial "flat" spin texture where all the spins align. (b) a spin texture that at first seems more complicated but in fact has the same topology as (a) due to the fact that the rotation changes direction at the midway point. (c) a truly topological texture. There is no way to remove the twisting from the spin chain through gradual rotation.

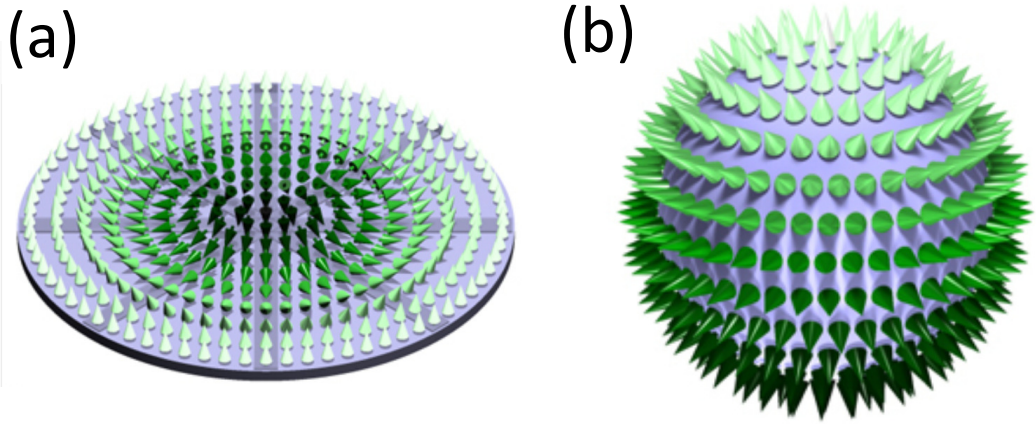

Figure 2.6: Cartoon illustrations of skyrmions in both (a) 2D and (b) 3D, with the spikes indicating spin direction. Reproduced from the work of M. Hoffmann [37].

undergo opposite sense rotations can this texture be unwound. This concept can be extended upwards into two and three dimensions where the resulting texture is known as the magnetic skyrmion which is shown in Figure 2.6. The idea that such a topological quasi-particle could exist in a magnetic material was first suggested by A. Bogdanov and U. Rößler in the early 2000s [39, 40]. In 2009, S. Mühlbauer *et al.* showed the first experimental results for skyrmions in MnSi at temperatures below 29.5 K [41] and they have since been found in a wide array of material systems and at a wide range of temperatures [42–45].

In the initial theory, in order for a twisting between magnetic moments to form a stable structure, the system would have to have preference for moments to orientate with some angle between them. In the discussion of exchange interaction in section 2.2.1, only the situation of complete aligning or anti-aligning was discussed. It was the work of I. Dzyaloshinskii and T. Moriya [46, 47] which showed that an antisymmetric term could exist in the exchange interaction as the result of spin-orbit coupling (the coupling of an electron's spin to the magnetic field it experiences due to moving at relativistic speeds around the charged nucleus. See the textbook by J. Binney and D. Skinner [30] for more details). This interaction, often called the Dzyaloshinskii-Moriya Interaction (DMI), introduces an extra term to the Heisenberg Hamiltonian in equation 2.5, with the qualitative form:

$$\boldsymbol{H}_{DMI} = -\frac{1}{2}\sum_{\langle i,j\rangle} \boldsymbol{D}_{i,j} \cdot \left(\boldsymbol{S}_i \times \boldsymbol{S}_j\right). \tag{2.16}$$

Here, $\boldsymbol{D}_{i,j}$ provides the magnitude and sign of the antisymmetric exchange. The cross product favours orientations of spins that are perpendicular to each other, and so when combined with the regular symmetric exchange the result is a rotation to some canted angle. It's worth noting that in crystals that are inversion symmetric, the magnitude of $\boldsymbol{D}_{i,j}$ is 0 and so DMI sometimes needs to be induced through the presence of boundaries that break this symmetry [48, 49]. The presence of DMI is often described as "stabilising" the skyrmions as without it a skyrmion state would not be energetically favourable.

Over the last two decades the creation, destruction and movement of skyrmions in both 2D and 3D has been a highly studied topic [50–54] with a particular eye towards the compact and energy efficient storage of magnetic data [55–57], as well as applications in neuromorphic computing [58–61].

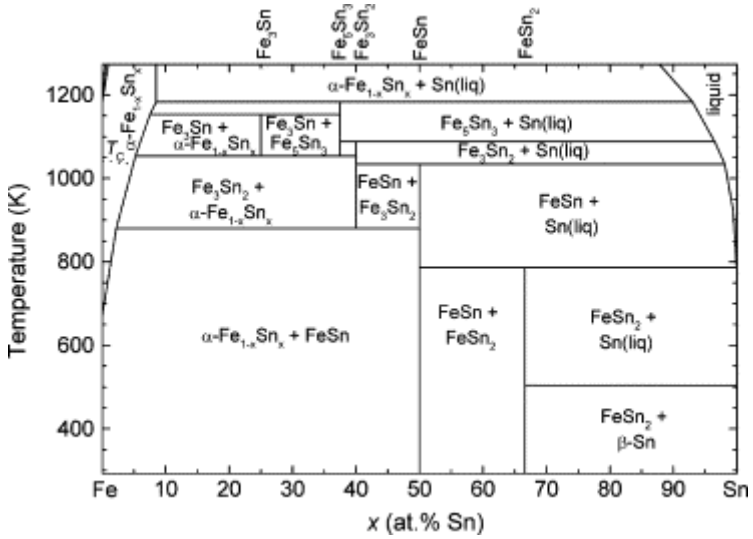

Figure 2.7: Computed phase diagram for the Fe-Sn intermetallic compounds reproduced from the work of H. Giefers and M. Nicol [22]. Originally based on the phase diagram presented by H. Kumar [63].

2.3 The Crystallography of Fe_3Sn_2 and FeSn

Due to Fe_3Sn_2 and FeSn being the two key phases discussed in this work, it is worth taking a moment to fully appreciate their crystallographic structure. There are in fact five Fe-Sn intermetallic alloys: $FeSn_2$, FeSn, Fe_3Sn_2, Fe_5Sn_3, and Fe_3Sn [22, 62] whose unit cells are presented in appendix A. The phase diagram [22, 63] for Fe-Sn is shown in Figure 2.7. It is worth noting that the Fe_3Sn_2 phase is not stable at room temperature while the FeSn and $FeSn_2$ phases are. In this work, materials will be grown at elevated temperatures above 700 K to try and position within the Fe_3Sn_2 region of the phase diagram.

FeSn is a hexagonal crystal with the $P6/mmm$ space group and lattice constants $a = b = 5.298\,\text{Å}$ and $c = 4.448\,\text{Å}$ [22]. It is formed of two distinct layers that stack alternately [66]. The first is a pure Sn layer arranged in a honeycomb of hexagons (when isolated, this individual layer is sometimes called a "stanene layer" as an analogy to graphene [67]). The other layer has the chemical composition Fe_3Sn and has a more complicated structure with Sn atoms being found at the corners of each cell of the repeating rhombus [68]. The more interesting feature is that this results in the Fe atoms being held in a kagome structure, a structure of regular triangles separated by hexagons as shown in Figure 2.8. Since Sn atoms have no net moment, the magnetic properties are completely determined by the spins in the Fe_3Sn and

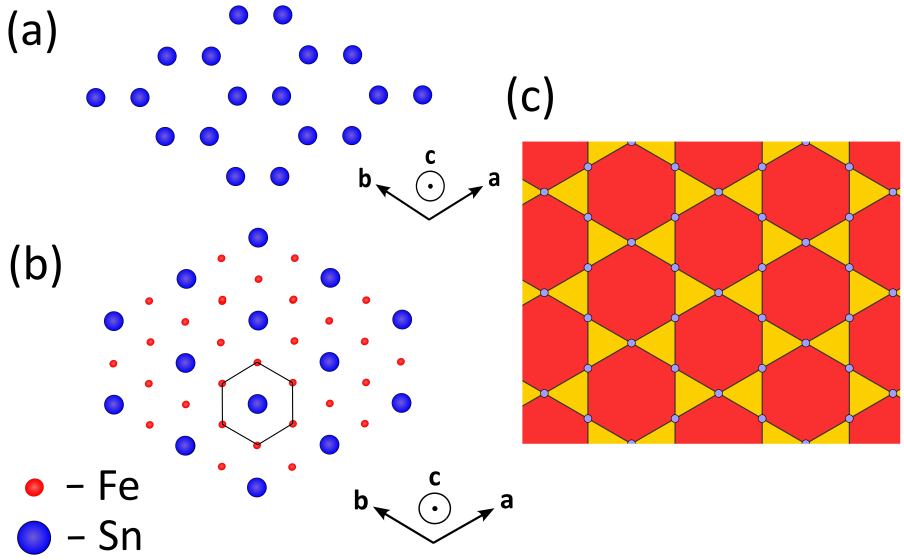

Figure 2.8: Diagrams of (a) the pure Sn stanene layer with its clear hexagonal structure; (b) the Fe_3Sn layer with its rhombohedral Sn and kagome Fe structure. A hexagon of Fe atoms has been indicated to help draw the eye to the similarities to (c), an illustration of the kagome pattern originally illustrated by T. Piesk [64].

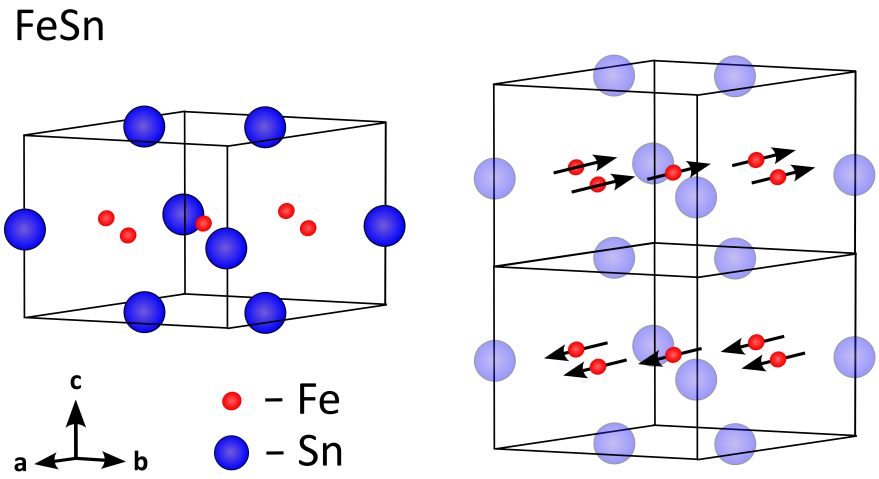

Figure 2.9: Diagrams of (a) the crystallographic unit cell of FeSn and (b) the magnetic unit cell formed by repeating the regular unit cell along the c-axis to produce an A-type antiferromagnet. Magnetic moments are restricted to Fe atoms and are represented by arrows. Notice that the basis of this unit cell is a parallelogram and not a square structure and so the layers form the structures as seen in Figure 2.8.

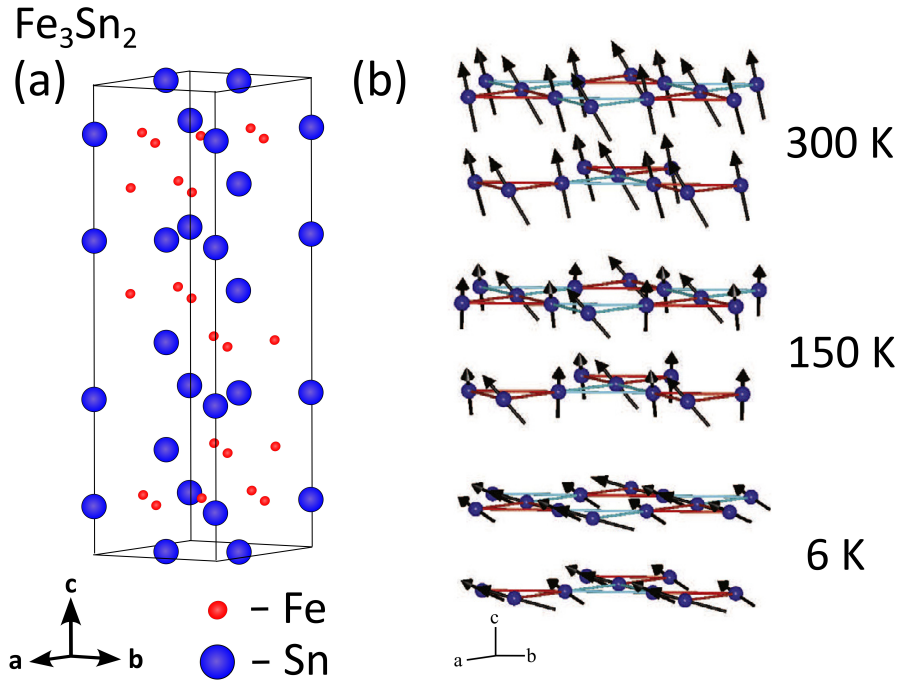

Figure 2.10: Diagrams of (a) the crystallographic unit cell of Fe_3Sn_2 and (b) the temperature dependent spin orientation from the simulations performed by L. Fenner [65].

their interactions. For FeSn all moments within a given Fe_3Sn plane couple ferromagnetically, but moments between planes couple antiferromagnetically [24] as shown in Figure 2.10. This results in FeSn being an A-type antiferromagnet with a Néel temperature of 370 K [69].

Fe_3Sn_2, rather than just having alternating stanene and Fe_3Sn layers, has a more complicated layered structure with each stanene layer separated by two layers of Fe_3Sn and each Fe_3Sn to Fe_3Sn stacking being displaced by the stacking vector $\begin{pmatrix}1/3 & 1/3 & h\end{pmatrix}^T$ (in fractional lattice coordinates [70], where h is the separation between layers in said coordinates). This shifting in the basal plane reduces the symmetry and means that Fe_3Sn_2 is actually not hexagonal but trigonal with the space group $R\bar{3}m$ and lattice constants $a = b = 5.340$ Å and $c = 19.797$ Å [22]. This results in a total unit cell volume of $V = 497.13$ Å^3 with 18 Fe atoms and 12 Sn atoms for a total atomic number density of 6.034×10^{28} m^{-3}. Due to the bilayer of Fe_3Sn within its structure, Fe_3Sn_2 is a ferromagnet with a Curie temperature of about 657 K [23]. There is a temperature dependent reorientation of these moments from orientation along the c-plane at room temperature and above to lying almost entirely in the basal plane at temperatures below 60 K [71, 72]. Through examining the irreducible representation for the $R\bar{3}m$ group, L. Fenner [65] showed that this reorientation produces a frustrated arrangement of the spins rather than a collinear arrangement as previously expected.

2.4 Fe_3Sn_2 as a Skyrmion Host

The DMI interaction of equation 2.16 is one way that the canted spin state, and therefore skyrmions, can be present within a material; but another way that a non-collinear spin arrangement can form is through the frustration described above. This has been shown to successfully stabilise skyrmions in a range of systems [73–75] with an added advantage being that frustration stabilised skyrmions should have a free chirality that can be manipulated without necessarily having to change any other characteristic of the skyrmion such as its size. In the case of Fe_3Sn_2, this would likely manifest as being able to control the chirality of a forming skyrmion by using electrical pulses to deliver short bursts of magnetic field that can bias the skyrmion to form with either one chirality or the other.

2.4.1 Initial Observation and Chirality Switching

With this in mind, the presence of skyrmions within Fe_3Sn_2 were first predicted by M. Periero [76] and then later verified experimentally by Z. Hou *et al.* [77]. In a further work by Z.

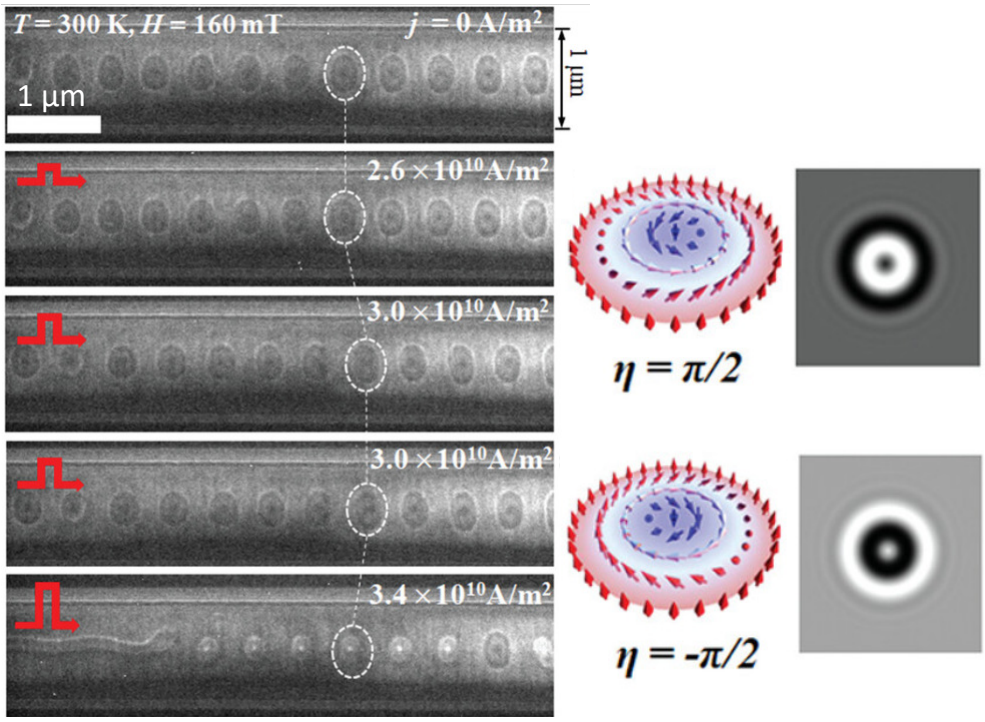

Figure 2.11: Observation of current pulse induced skyrmion helicity switching. Diagrams lightly adapted from the work of Z. Hou *et al.* [78].

Hou *et al.* [78] a Focused Ion Beam (FIB) technique was used to carve a nanotrack from the surface of an Fe_3Sn_2 sample which was then observed with Lorentz Transmission Electron Microscopy (LTEM). The hope was that by restricting the nanotrack to be no larger than 1 μm wide, domain walls and other undesired textures could be suppressed. This seems to have been very successful with the only textures present being the skyrmions to be observed. The skyrmions present in these devices were shown to have a helicity that could be reversed through the application of current pulses as seen in Figure 2.11. It is worth noting that at high current densities there seems to be evidence that the skyrmions are breaking down into more of a line domain. This is briefly commented on in the paper, but not expanded upon. However, further work by the same group [79] has begun to investigate the effect of current pulses on skyrmion splitting.

A closely related piece of work worth comparing to is that of Q. Du *et al.* [80] which also uses LTEM to study the skyrmions in Fe_3Sn_2. Again, bulk single crystals of Fe_3Sn_2 grown at 1150°C were used as a starting point, though this paper goes into slightly more detail of

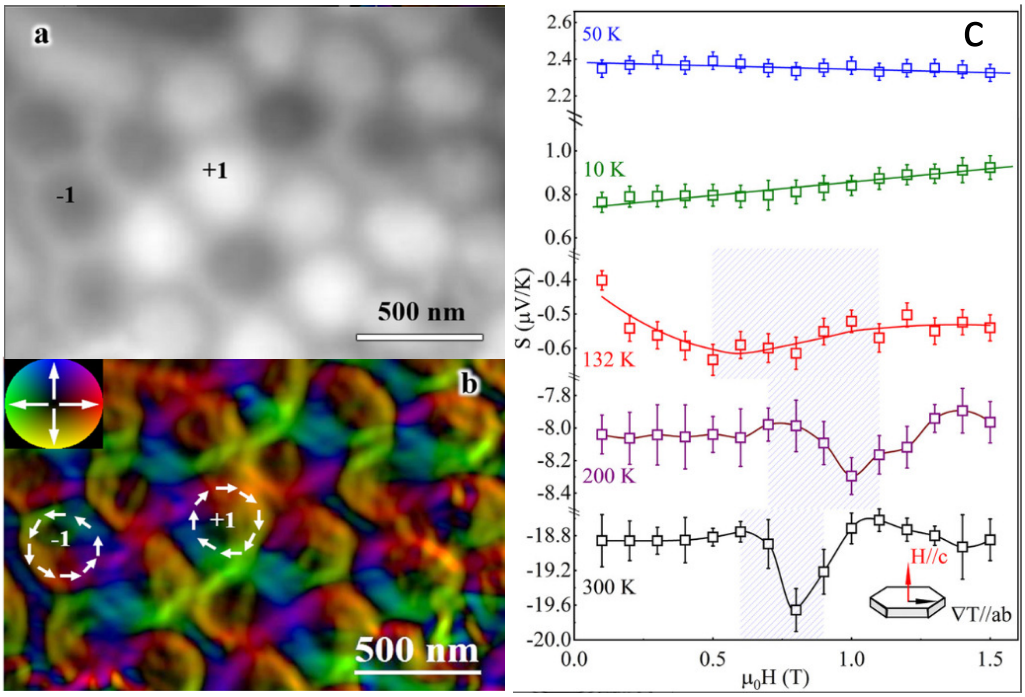

Figure 2.12: (a) LTEM phase shift image (b) colour contour image highlighting the topology of the bubbles. Both taken in 11.7 mT. (c) Seebeck coefficient versus magnetic field for a range of temperatures. The shadow area indicates conditions where the skyrmionic phase is present. Diagrams lightly adapted from the work of Q. Du *et al.* [80].

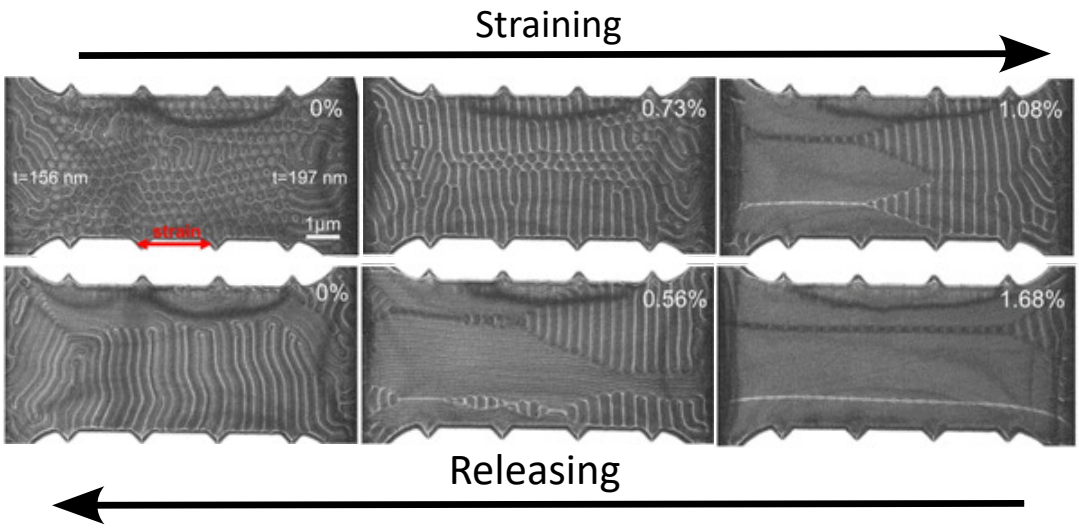

Figure 2.13: The effect of applying and releasing strain on an Fe_3Sn_2 lamella, viewed parallel to the c-axis. The initial skyrmion state is seen to dissolve and fails to reform on the releasing of the strain. Diagrams lightly adapted from the work of D. Kong *et al.* [81].

the characterisation steps showing both powder and single crystal X-ray Diffraction (XRD) patterns for their samples. Rather than using geometric confinement, the goal of this work was to examine the effect of temperature gradient on the skyrmions and in particular to see if a thermoelectric measurement could be made. The conclusion was that at room temperature, electron diffusion was the main component of the Seebeck coefficient (the ratio of generated voltage to temperature gradient) as opposed to magnon or phonon contributions. In Figure 2.12, it can be seen that the Seebeck coefficient was observed to change by up to 4% as the skyrmion state was entered (indicated by the shaded regions), which the paper associated with an increase in the entropy of the crystal lattice. In particular, this paper does an impressive job of explaining the low temperature to high temperature behaviour and the fitting of the electron and phonon behaviour below the 124 K transition is very well done.

2.4.2 Current Free Control

A final pair of papers that are worth mentioning are that of L. Kong and J. Tang *et al.* [82] and D. Kong *et al.* [81] (no relation). Again, as above, single crystals of Fe_3Sn_2 were grown through vapour deposition at a temperature of 800°C. In the work of L. Kong and J. Tang, rather than a nanotrack like the work of Z. Hou, a nanodisk was created through a similar

FIB process to produce the geometric confinement. These disks were typically 150 nm thick and 510 nm in diameter. Again, skyrmions could be imaged using LTEM and in this case a phase diagram describing the changes from a skyrmion state and a topologically trivial bubble state was produced. The state changes were controlled through the application of different magnetic field strengths at different incidence angles to the nanodisks. Finally, the work of D. Kong *et al.*, published in February of 2025, is a study into the effects of strain for skyrmion control. Since very thin lamellae need to be made for the electron imaging process, it is then possible to load them into a straining device that can produce strain in the material during imaging through which it was shown that the stripe domains did not return to the skyrmion state after release, as seen in Figure 2.13. The most surprising result, as highlighted in the paper, was that under strain the domain walls ended up forming perpendicular to the strain direction as opposed to parallel to it as was initially predicted. A large focus was put on the observation of skyrmion merging mechanisms under moderate strain conditions (as seen in the second panel of Figure 2.13), but I feel the most interesting result of the paper was the observation that strain induced a rotation of the moments from out-of-plane to in-plane and that this process was reversible while the skyrmion destruction process was not.

2.4.3 Conclusion

The observation of skyrmions within Fe_3Sn_2 is now well established, with a favoured method of observation being LTEM. For a review article on the use of LTEM for skyrmion imaging, there is the work of J. Tang *et al.* [83]. All of these observations have only been performed in bulk crystals that have been milled down to the desired geometries for the work required.

2.5 The Electronic Band Structure of Fe_3Sn_2

If a magnetic field is applied perpendicular to the current direction of a conducting material, the charge carriers will experience the Lorentz force [84] which will act to push them on the axis perpendicular to both current and field. This effect, known as the ordinary Hall effect, acts to set up a transverse voltage across the sample. Due to the Lorentz force having the form $\boldsymbol{F} = q(\boldsymbol{E} + \boldsymbol{v} \times \boldsymbol{B})$, we would expect the transverse resistivity ρ_{xy} to scale proportional to $|\boldsymbol{B}|$. In practice, it is often found that materials actually experience a secondary source of transverse resistivity which is called the Anomalous Hall Effect (AHE) that is (to first order) proportional to the magnetisation of the material M [29]. The form of the transverse resistivity

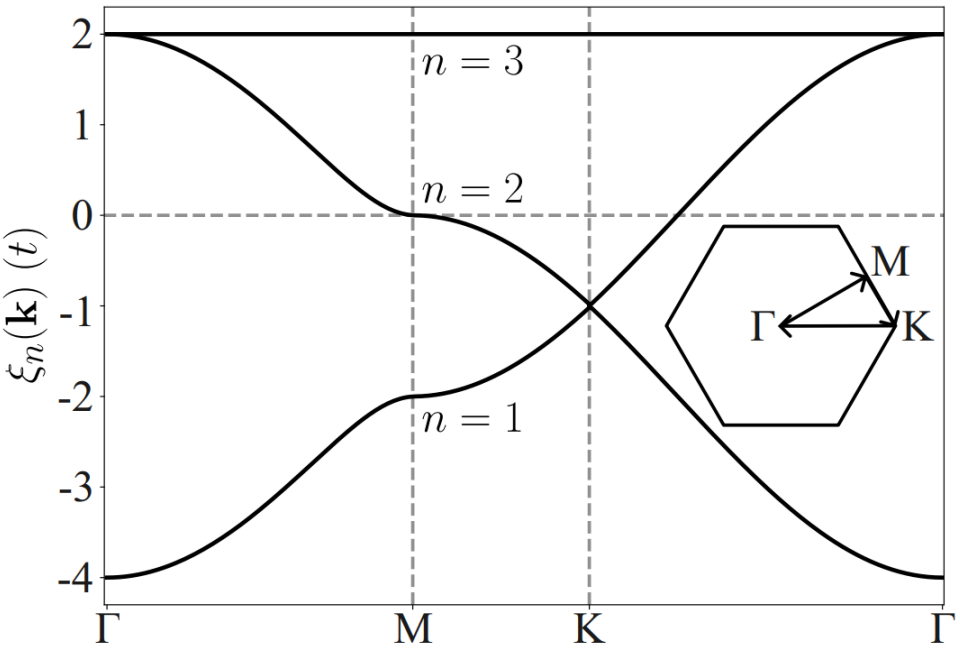

Figure 2.14: The electronic bands of the kagome structure. The saddle points at M in bands 1 and 2 are associated with a divergence in the density of states as well as a divergence associated with the band 3 which is completely flat. There is also a Dirac point present in the crossing at K. Reproduced from the work of S. Holbæk [86].

can then be described qualitatively as:

$$\rho_{xy} = R_o B + R_a M. \tag{2.17}$$

Here, R_o and R_a are coefficients associated with the ordinary and anomalous Hall effect respectively. However, the anomalous Hall effect is actually a reasonably complex effect with five independent mechanisms being identified by the review article of N. Sinitsyn [85]. The terminology across the literature is also sometimes ambiguous and so for consistency the terminology present in this review article will be used. The most important distinction being that an intrinsic AHE is one produced through a fundamental trajectory that a charge carrier (or more strictly a wave packet) is obliged to follow due to a material's band structure when an external electric field is applied to the material. An extrinsic AHE is produced through the scattering off of impurities or defects within the crystal.

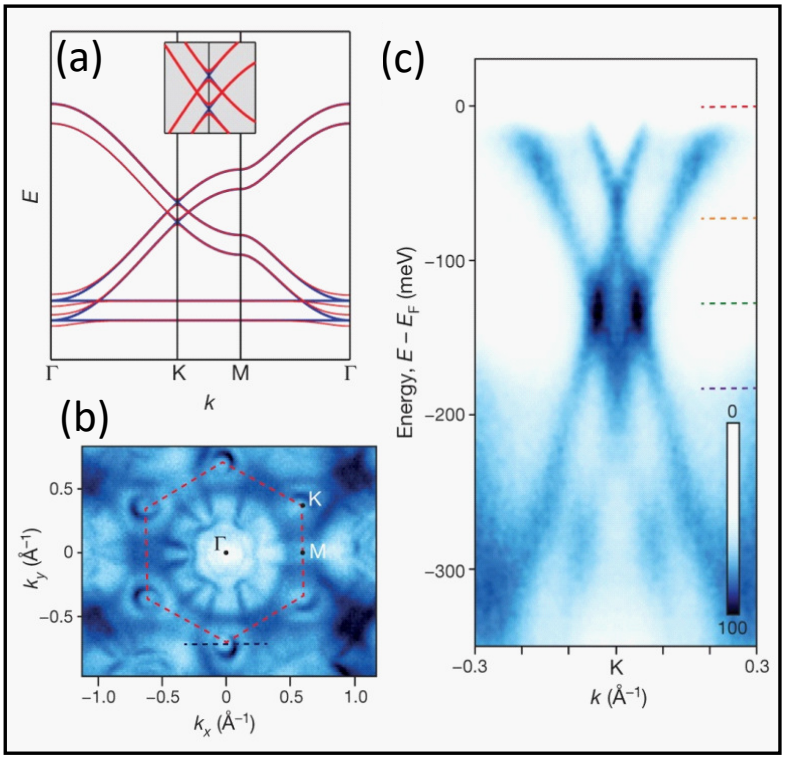

Figure 2.15: (a) is the tight-binding band model of the double-layer kagome lattice with in-plane hopping t and inter-plane hopping $0.3t$, the red and blue lines are with and without spin orbit coupling ($\lambda = 0.05t$). (b) is the experimentally measured Fermi surface of Fe_3Sn_2 with the Brillouin zone marked as the red hexagon. The black dotted line is the path for the symmetrised ARPES data that has been collected in (c). Lightly adapted from the work of L. Ye *et al.* [87].

By solving the tight-binding model on the kagome structure it is possible to produce a model for the electronic band structure which contains both Dirac points as well as flat bands [86]. The three bands of this model are shown in Figure 2.14 though it is worth noting that if spin-orbit coupling were to be introduced this would lead to an avoided crossing at the K point [87]. FeSn, with its single layers of Fe_3Sn separated by the stanene layers, has long been considered an ideal candidate for investigating the kagome band structure [88–91], being close to the model 2D condition.

2.5.1 Increased Anomalous Hall Effect

As discussed in section 2.3, Fe_3Sn_2 contains a more complicated bi-layer system than a standard kagome structure, so there will be some probability of hopping between the neighbouring Fe_3Sn layers. The work of L. Ye *et al.* [87] takes this into account and combines the theoretical results with electrical transport and Angle-Resolved Photoemission Spectroscopy (ARPES) measurements as shown in Figure 2.15. The main goal of this work was to examine the contribution of massive Dirac fermions (the result of the spin-orbit induced avoidant crossing mentioned above) to the Hall conductivity σ_{xy} (the off diagonal component of the inverted resistivity matrix). The experimentally measured AHE was $\sigma^a_{\mathrm{xy}} = 0.27 \pm 0.03 \frac{e^2}{\hbar}$ per bilayer while the relatively simple tight-binding model produced a value of $\sigma^a_{\mathrm{xy}} = 0.31 \pm 0.05 \frac{e^2}{\hbar}$ which is a very impressive agreement and the analysis of the different contributions to the anomalous Hall effect allowed for a clear separation of intrinsic and extrinsic contributions.

1050 - wang, Kida - 800 Two other works worth comparing are that of T. Kida *et al.* [92] and Q. Wang *et al.* [93] that are two of the earliest works on the electronic properties of Fe_3Sn_2 (coming out in 2011 and 2016 respectively). Both papers use a four-probe method on rectangular cuts from single crystals (grown at 800°C for Kida and 1050°C for Wang) and seek to study how the AHE resistivity depends on the longitudinal resistivity, ρ_{xx}, which can be an indicator of whether an intrinsic or extrinsic process is contributing to the event. The surprising result is that despite the similarity in method they record very different results. The most obvious being that T. Kida reports a relationship of $\rho^a_{\mathrm{xy}} \propto \rho^{3.15}_{\mathrm{xx}}$ while Q. Wang reports $\rho^a_{\mathrm{xy}} \propto \rho^{1.93}_{\mathrm{xx}}$ which Wang associates with the fact that their samples were single crystal as opposed to the polycrystalline samples of Kida. A slightly more subtle difference is that T. Kida reported a change in the sign of the ordinary Hall effect coefficient, R_{o}, with changing temperature. No values are given, but from Figure 2.16 it is clear that the change is very slight. Also shown for comparison are the results from Q. Wang which show no change in ordinary Hall effect. No comment is made on this difference in the later paper.

More recent work by Q. Du *et al.* [94] has used a FIB technique to form Hall bars out of a single crystal of Fe_3Sn_2. In a brilliant demonstration of the power of this technique, separate Hall bars were created from along both the basal plane and the c-axis of the crystal. Transport measurements taken with current flowing along this c-axis direction are basically a measurement of the effects of electron hopping between the kagome planes with strong evidence for an increase in the AHE coming from the real space non-collinearity of the spins.

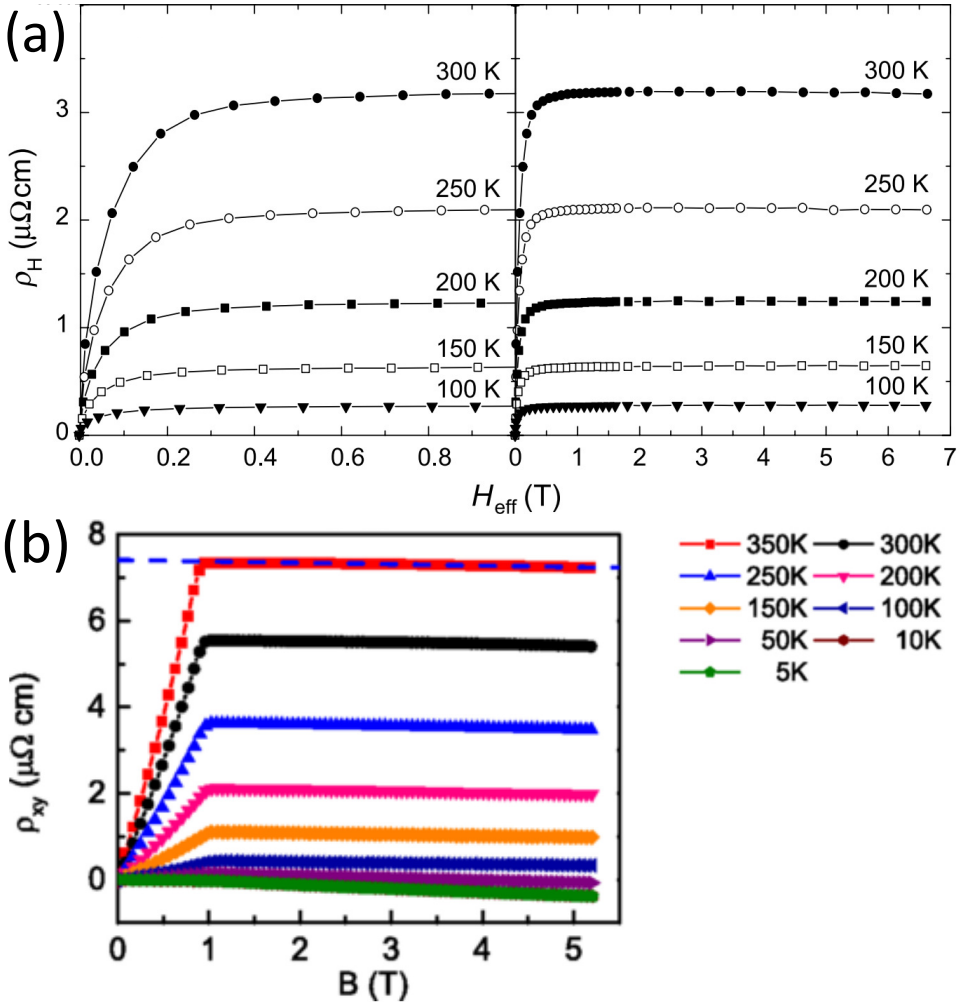

Figure 2.16: (a) is the Hall resistivity measurements of a polycrystalline sample over a range of temperatures, with the left box being the range 0 to 1 T and the right being from 0 to 7 T. Lightly adapted from T. Kida *et al.* [92]. (b) is the Hall resistivity measurements of a single crystal sample over a range of temperatures. Lightly adapted from the work of Q. Wang *et al.* [93].

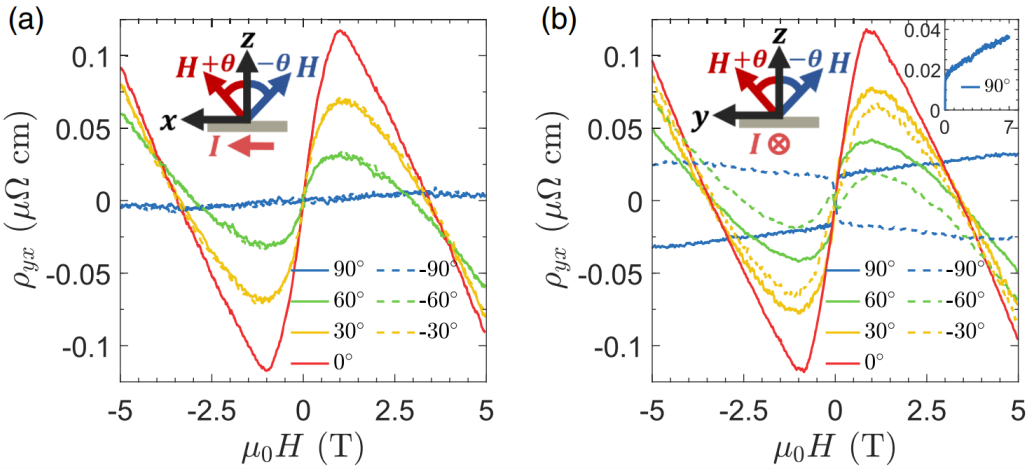

Figure 2.17: Hall resistivity, ρ_{xy}, measured as the field is rotated into the plane (a) parallel and (b) perpendicular to the current direction at a temperature of 50 K. The inset in (b) shows the roughly linear dependence of the $\theta = 90°$ on field. Lightly adapted from the work of L. Wang *et al.* [95].

2.5.2 In-Plane Anomalous Hall Effect and Magnetoresistivity

In the work of L. Wang *et al.* [95] a single crystal sample of Fe_3Sn_2 was grown at 770°C. This work reports a distinct difference in the In-Plane Hall effect (IPHE) when the field is orientated parallel and perpendicular to the current direction, as shown in Figure 2.17. This is a very interesting measurement, and attempts are made to replicate it in the results section of this work. The jump in ρ_{xy} which is seen in Figure 2.17 (b) at near 0 T, is described as being "clearly" due to AHE, though it is not made clear why the change in magnetisation direction should be any different in Figure 2.17 (a) which does not demonstrate this effect.

Another work on a similar topic is that of Y. Li *et al.* [96] who use a neutron scattering to first measure the bulk spin texture of the Fe_3Sn_2 samples and monitor its change under magnetic field. After this, magnetotransport measurements under an IP field were used to gather the angular dependence of the magnetoresistance. Highly anisotropic butterfly patterns were found though still only with a two fold symmetry and not the three fold or six fold symmetry we might expect from the kagome structure.

2.5.3 Fractional Quantum Hall Effect

Even if briefly, it is worth mentioning the theoretical results of E. Tang, J. Mei, and X. Wen [97] who showed that a Fractional Quantum Hall (FQH) state could exist in the flat band structure of Fe_3Sn_2 at high temperatures (the exceptionally large band gap between the flat bands likewise makes integer quantum Hall effect at high temperature likely). A requirement to set up these fractional states is the fractional filling of one of the bands with the paper's suggested method being doping; however in a thin film gating or charge transfer to a molecular interface could also provide this effect. Currently, there is no experimental work in the literature testing these theoretical results.

2.5.4 Conclusion

Fe_3Sn_2 has been shown to have an interesting and complicated band structure with an intrinsic component of the AHE being firmly established, though the exact magnitude and source is inconclusive. Also, other more exotic band states have been predicted by theory but still have not been experimentally recognised.

2.6 Thin Film Deposition of Fe_3Sn_2

Over the last few years, with the general increase in interest of Fe_3Sn_2 as a material containing the magnetic and transport properties as discussed above, there has also been an interest in producing thin films of this material. Thin films, as opposed to bulk samples, are often the way that novel materials find practical applications in spintronics, magnetic sensing and data storage. For a broad but thorough overview of thin films (both magnetic and not) and their plethora of uses there is the review article by S. Sakthinathan *et al.* [19].

2.6.1 Growth Through Molecular Beam Epitaxy

H. Inoue *et al.* [98] have demonstrated the growth of thin films in FeSn through the process of Molecular Beam Epitaxy (MBE). Due to the similarity in crystal structure, especially with the similar lattice constants in the basal plane, a growth process that works for epitaxial FeSn then has the potential to also work for epitaxial Fe_3Sn_2 with suitable adjustments to temperature and stochiometric ratio as to avoid producing one of the other four possible Fe-Sn intermetallic compounds. MBE is a process of very slow vacuum deposition where the Fe and Sn is evaporated into the chamber and allowed to gradually build up; ideally leading to

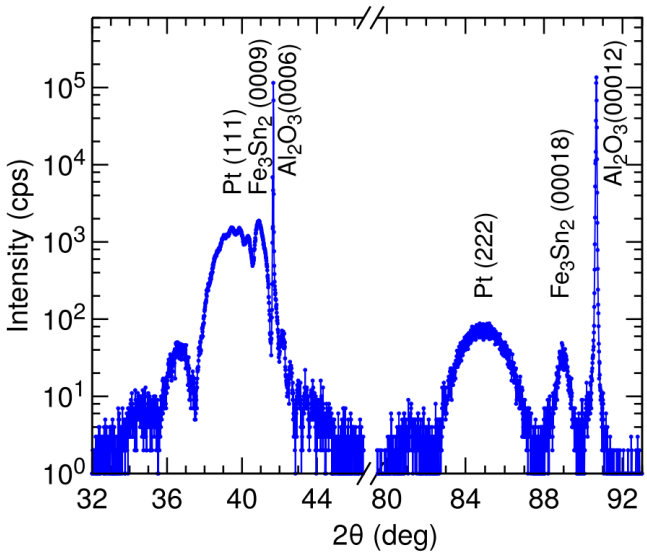

Figure 2.18: XRD pattern from an Fe_3Sn_2 film grown on sapphire with a Pt seed layer using MBE. The pattern is only shown from the 32° to 46° and 80° to 93° range, which means that the presence or absence of the other characteristic peaks of Fe_3Sn_2 are not visible. Reproduced from the work of S. Cheng [99].

lattice matching between the thin film and the substrate. The substrate chosen was $SrTiO_3$ (111), which is known to have a lattice constant 3.4% different from FeSn. A key goal of this paper was growth of pure FeSn with as few of the other Fe-Sn compounds present as possible. Alternatives to STO have also been investigated, such as the work of D. Hong *et al.* [21], who also applied MBE to the growth of FeSn but instead chose $LaAlO_3$ (111) as the substrate, which has lattice parameters matching those of FeSn to within 1%.

Both papers produce promising results, convincingly showing epitaxial growth on their chosen substrates with the presence of other orientations only being detected in small amounts. Overall, the analysis in D. Hong *et al.* [21] is more holistic however. The work of H. Inoue *et al.* limits itself to X-ray and electrical transport characteristics, leaving some doubt as to features such as coverage and smoothness of their film. Hong provides Reflection High-Energy Electron Diffraction (RHEED) and atomic force microscopy data to characterise smoothness and STEM and SEM images to provide evidence of the presence of FeSn islands. This further analysis leads to an interesting result for further exploration. The RHEED results showed an amorphous layer (50 nm) of Fe-Sn upon their substrate before crystalline growth takes over. This calls into question the strict epitaxy of these films. The cause and resulting effects of this

amorphous layer are something that likely needs to be understood for repeatable growth of single structure crystals in the future.

Another potential substrate to consider for epitaxial growth of Fe_3Sn_2 is sapphire (Al_2O_3) with Pt (111) buffer layers. The work of S. Cheng *et al.* [99] used MBE to sequentially layer Fe_3Sn followed by Sn_2 to build up the correct layer stacking. The use of RHEED during growth is highly convincing that the correct atomic layers are being produced, especially the RHEED signal against time graph that shows clear oscillations representing the Fe_3Sn and Sn_2 terminations. This paper also thoroughly describes its growth parameters such as rates, temperatures and substrate preparation and would form the starting off point of any future MBE growth. The main novelty of this paper was the use of Pt as a seed layer on the sapphire substrate which will be also discussed in the next section. The final thing worth noting is that the XRD characterisation presented, shown in Figure 2.18, does not cover the full range of angles in 2θ. This means that symmetry allowed (0003) and (0006) XRD peaks at low angles are not presented, perhaps because they are not observable for these films.

2.6.2 Growth Through Sputter Deposition

The deposition of thin film Fe-Sn intermetallic compounds through sputter deposition has also been attempted, with the initial work performed by Satake *et al.* [100]. This paper was interested in the applicability of Fe_3Sn_2 and Fe_3Sn in anomalous Hall effect (AHE) sensors for which thin films were a necessity. They attempted a cosputtering technique (see section 3.2) of embedding Fe chips into their Sn target, with the Fe content of the films adjusted by changing the chip number. Growth at 500 °C on a sapphire (0001) substrate resulted in films containing a mixture of the Fe-Sn compounds leading to films of the form Fe_xSn_{1-x} with x = 0.54, 0.62, and 0.78. The methods section says that Energy Dispersive X-ray (EDX) spectroscopy was used to obtain compositional analysis, though this data unfortunately is not presented in the paper or in the supplementary information. The paper "suggests the existence of Fe_3Sn_2-like domains in the nanocrystalline film with x=0.60" and so goes on to only consider the properties of the mixtures between the FeSn, Fe_3Sn_2 and Fe_3Sn phases. More detailed XRD analysis is provided in the supplementary information, though with the presence of multiple phases, some contributing quite broad polycrystalline peaks to the pattern, exact identification of phase content is difficult which is also commentated on in the supplementary information. Nevertheless this paper provides evidence that sputter deposition is a growth process worth investigating for Fe_3Sn_2, with an avenue of further work being to refine the process to produce

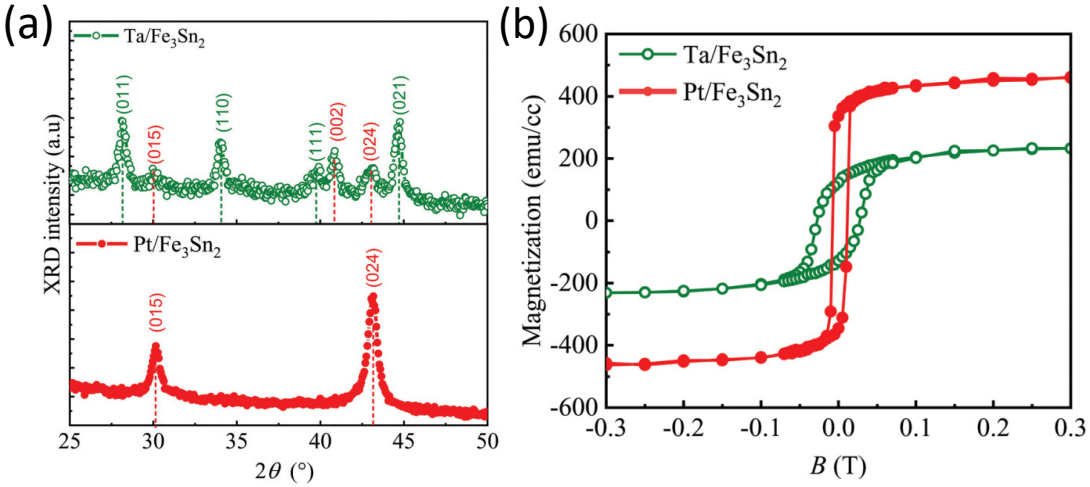

Figure 2.19: (a) XRD patterns comparing the diffraction peaks present in a film grown on a Ta or a Pt seed layer, represented in green and red respectively. Green dashed lines indicate peaks associated with FeSn and red with Fe_3Sn_2. (b) Magnetisation hysteresis loop comparing the films grown on the two seed layers. Lightly adapted from the work of K. Khan [101].

a finer crystallographic order and single phase within the films.

It is also worth noting the work of K. Khan *et al.* [101], published in the same month as the paper by S. Cheng [99], also suggests Pt as a good seed layer for Fe_3Sn_2. In particular, they study the difference in properties achieved by growing on either a Pt or a Ta seed layer. The films were grown on Si at room temperature with sputter deposition from an Fe_3Sn_2 target and then annealed at 500 °C. The strong conclusion to be drawn was that Pt was a far more suitable seed layer, at least for this growth method. The XRD and magnetisation loops from the two films are compared in Figure 2.19. The many XRD peaks from the FeSn phase in the Ta example, indicate that the Ta layer is inferior to the Pt layer for growing a uniform film content. The lack of FeSn XRD peaks in the Pt example, as well as the larger magnetisation and smaller coercivity indicate the Pt seed layer is likely to have produced a significantly higher quality film. Transport measurements, such as a significantly better Residual Resistivity Ration (RRR) for the Pt film compared to the Ta film (2.2 as opposed to 1.1) also corroborates this conclusion. It is also worth noting that the ordinary Hall coefficient, R_o, was found to be always positive for the film grown on the Pt seed layer.

More recently, a paper by Zhang *et al.* [102] uses magnetron sputtering from Fe_3Sn_2 targets to produce thin films of Fe_3Sn_2. These films were grown on sapphire and MgO substrates. The

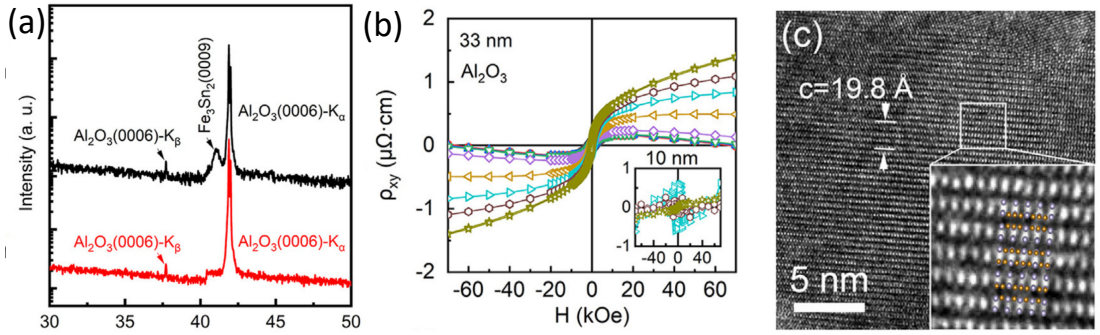

Figure 2.20: (a) XRD patterns comparing a clean substrate and a substrate with Fe_3Sn_2 film (in red and black respectively). (b) Measurement of the Hall resistivity ρ_{xy} at a range of temperatures. The change from a negative to positive gradient in the linear part of the graph indicates a carrier type change has occurred. (c) High resolution TEM image of Fe_3Sn_2 region with lattice constant labelled. Lightly adapted from the work of D. Zhang [102].

morphology and composition were then confirmed using XRD and Atomic Force Microscopy (AFM) measurements. As in the work of S. Cheng [99], the range of angles presented in the XRD data is not large enough to see the presence of any of the low angle peaks, as seen in Figure 2.20. An interesting result for later confirmation is the claim that thicker films develop consistent "hollows" in the surface reducing the expected volume of the films. Further detailed analysis of the samples was given by high resolution TEM to gain confirmation of the correct lattice constants being present and also a qualitative view into the atomic ordering. Squid magnetometry was used to check the magnetic properties, and transport measurements were then performed to measure the AHE. The paper claims to be able to extract an intrinsic contribution to the AHE that they associate with the presence of a skyrmion spin texture. Interestingly, as seen in Figure 2.20, the changing sign of the ordinary Hall coefficient is present in this work.

The final work worth discussing in detail is that of D. Khadkha *et al.* [103] which provides some of the strongest evidence for high quality Fe_3Sn_2 growth through magnetron sputtering. An adaption is made from the works of S. Cheng [99] and K. Khan [101] in that not only was a seed layer of Pt used on the sapphire substrate, but also, another seed layer of Ru was deposited. After this, films of about 60 nm were grown and characterised with XRD. In this work, the low angle (0003) and (0006) peaks are presented as well as the more intense (0009) peak. To support this, in-plane ϕ scans are also presented revealing the expected six peaks as shown in

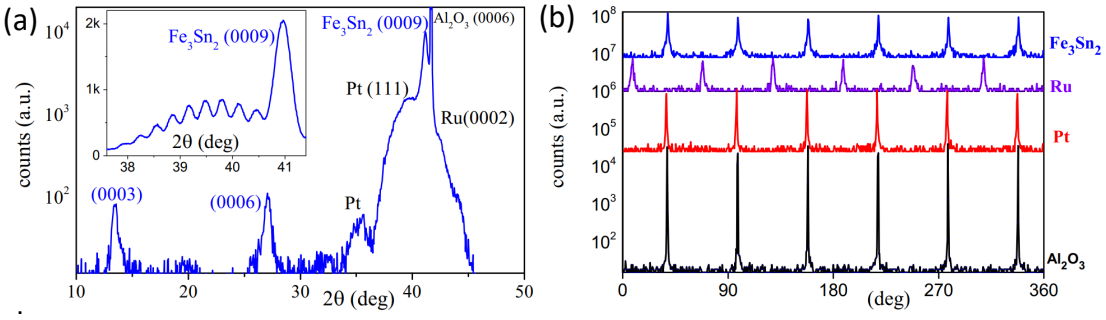

Figure 2.21: (a) XRD pattern of Fe_3Sn_2 film. Inset is a zoomed in view of the Fe_3Sn_2 (0009) peak. (b) ϕ measurement of each layer of the film showing the consistent hexagonal symmetry. Lightly adapted from the work of D. Khadkha [103].

Figure 2.21. Rather than solely focusing on the AHE, this paper proceeds to look at the Nernst effect (the current produced when a thermal gradient and perpendicular magnetic field are present in a material) as well as the Anomalous Nernst Effect (ANE) which, in a similar way to the AHE, is an extra contribution dependent on sample magnetisation. The conclusion was that the ANE was present, though extremely anisotropic due to the 2D nature of the kagome planes in Fe_3Sn_2.

2.6.3 Conclusion

Fe_3Sn_2 (as well as FeSn) has been grown within the literature to varying amounts of success through physical vapour deposition processes such as MBE or sputter deposition. In order to reach the appropriate section of the Fe-Sn intermetallic phase diagram, shown in Figure 2.7, high substrate temperatures typically in the range 400-500 °C are used. Also, a variety of substrates have been attempted with a general acceptance that c-plane sapphire with a seed layer of Pt has produced optimal results. In terms of overall properties, films grown have generally not had their low angle XRD peaks present, perhaps indicating the lack of long range crystallographic order. Also, disagreement remains as to the presence of a carrier type change with temperature for Fe_3Sn_2 with some papers showing a clear change and some showing no such transition. This transition (and the lack of transition) has appeared in both bulk and thin film materials and its presence remains an unanswered question.

I will continue in this work to use the optimal substrate of c-plane sapphire with a thin (1 to 5 nm) seed layer of Pt to encourage epitaxial Fe_3Sn_2 growth. Since epitaxial Pt already requires elevated temperatures of typically 500 °C for optimal growth, this will allow for the

high temperatures needed for the Fe_3Sn_2 phase to be used within one heating-cooling cycle.

Chapter 3

Experimental Methods

3.1 Introduction

Often we find in physics that the interfaces between two regions are the most interesting locations for studying new phenomena. For a thin film of 10 nm there is nothing but interface. The major challenge is how to produce such a film, since no mechanical method could reliably cleave a bulk crystal down to a uniform nm scale (without considerable cost and time).

In this chapter, the methods of sample growth through physical vapour deposition are described. The laboratory based characterisation with X-rays, magnetometry and electron microscopy is also discussed along with the necessary preparation preceding and analysis after.

3.2 Sputter Deposition

Sputter deposition is a physical vapour deposition process in which a working gas, typically Ar due to its chemical inertness, is ionised and accelerated into the surface of a material target. This kinetic bombardment of the accelerated ions will transfer energy and momentum to the atoms on the surface allowing them to overcome the surface binding energy. Once expelled, these atoms will proceed to coat all surrounding surfaces in a thin layer which can be used to grow thin films of the target material. In order to improve purity, reduce oxidisation, and to prevent recombination of the Ar^+ ions, this whole process occurs within a vacuum chamber into which the working gas is fed. The Ar^+ ions are produced through the voltage supplied to magnetron guns within the chamber. A diagram of these guns are shown in Figure 3.1, where a high voltage applied to the target disk turns it into the cathode while the grounded outer casing of the gun becomes a anode. If a voltage of a few hundred volts is applied to the material target, then the electric field produced ignites the Ar gas into a plasma which is contained by the magnetron's magnetic field, confining the electrons to the region just above the target. The negative potential of the target then attracts these Ar^+ ions, accelerating them to impact.

3.2.1 The Sputtering System

All samples presented in this work were grown in the same sputtering system (Leeds Kurt J Lesker Sputter Chamber 2, SLIM) shown in Figure 3.1. This chamber can consistently reach pressures of the order 10^{-7} mbar through a combination of a turbo and cryo pump. At this point, the greatest components of the pressure are being given by the presence of hydrogen

and water molecules. A Meissner trap, in effect a coiled metal tube within the chamber that can be filled with liquid nitrogen, allows water to freeze onto its surface and reduces the pressure further, optimally achieving low 10^{-8} mbar with the rest of the chamber at room temperature.

The chamber has space for 24 substrates at a time with heating bulbs above each substrate holder allowing for the substrate temperatures to be raised from room temperature up to 600 °C. However there are only two thermocouples measuring from diametric substrate holders. This, combined with the fact that the substrates are only heated through the radiative heating of the bulbs mounted above them, means that we can expect the actual temperature of the substrates to be around 50°C lower than the recorded temperature on the thermocouples, and perhaps all the way up to 100°C.

The magnetron guns shown in Figure 3.1 can have the material they are to grow, called the targets, loaded in and out of them as required. Each gun can be powered by one of either a pair of Advanced Energy power supplies, or a Hüttinger power supply. The pair of Advanced Energy power supplies are identical and by selecting a desired power to be supplied, a DC voltage is produced which normally results in a current of typically about 100 mA being sent through the target. Having these two identical power supplies means it is possible to power two guns simultaneously in a co-sputtering arrangement, where both guns are allowed to impinge on the same substrate growing a film that is an alloy of two desired elements.

The Hüttinger power supply provides an AC voltage to the target. This is useful for situations where the target material is not a conductor and so if a DC voltage was applied, the Ar^+ ions would build up on the surface (as their charge cannot be redistributed) and quickly form a layer that repels any further Ar^+ from making impact.

3.2.2 Substrate Preparation

Due to the nucleation dynamics of deposition, metal adatoms often have a tendency to clump with other metal adatoms during deposition meaning that the film undergoes what is known as Volmer-Weber growth [105] where island clumps of atoms grow on the surface eventually connecting up into a complete but ultimately polycrystalline film. If the individual crystallites are largely coordinated in their orientation, then they will grow together to form low angle grain boundaries. This is generally known as an epitaxial film which can be encouraged through the use of a seed layer. In order to produce epitaxial growth the seed layer has to be carefully selected as to also lattice match with both the substrate and the eventual Fe_3Sn_2 film that will be grown on top.

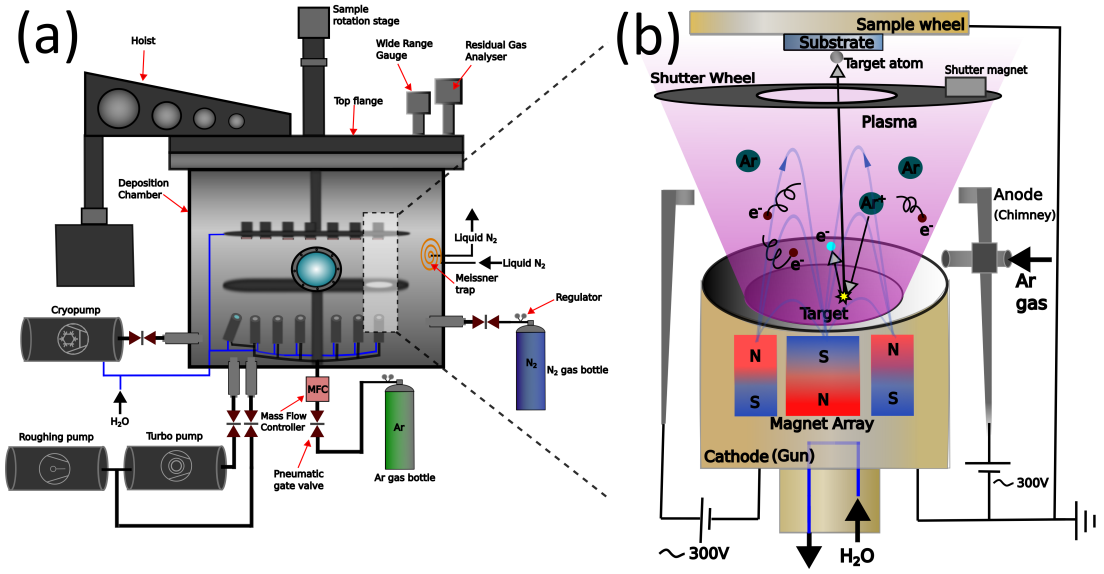

Figure 3.1: Schematic of the inside and outside components of the deposition chamber. The chamber as a whole is shown in (a) with the highlighted region containing the magnetron gun expanded upon in (b). Lightly adapted from the diagram of S. Gupta [104].

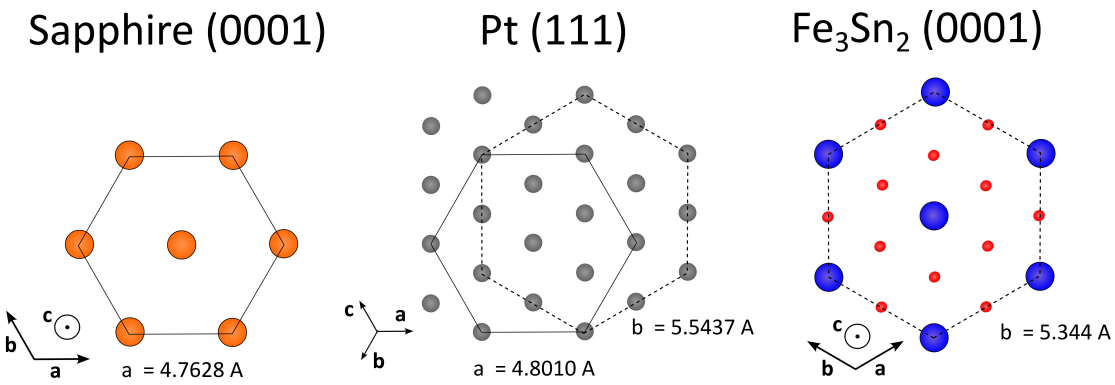

Figure 3.2: Diagram of the a-b plane in Al terminated sapphire and Fe_3Sn_2, and the 111 plane in Pt with the similarity in the lattice spacings indicated. Lattice constants for Fe_3Sn_2 are from the work of H. Giefers [22]. The lattice constants for Sapphire and Pt (and inspiration for this diagram) are from the work of R. Farrow [106].

The selected substrate of c-plane sapphire was chosen as it is well established as a substrate for the growth of epitaxial Pt [106]. The in-plane lattice spacing of large 40 mm diameter substrate wafers were first scored by a wafer saw before being marked to indicate the m-plane direction and broken by hand into 8 mm squares.

All substrates that entered into the deposition chamber were sonicated in acetone for five minutes to dissolve any organic oils that might have adhered to the surface. Following this, a sonication in isopropanol for another five minutes was used to clean off any acetone residue and after being carefully blown dry with a hand squeeze air pump the substrates were visually inspected before being considered clean enough to enter the system.

3.2.3 Process

Substrates for sample growth were typically loaded at midday the day before the samples were to be grown. After initial tests and pump down process was completed (typically to about 10^{-6} mbar after four hours) the heater elements were activated with a ramp rate of 50 °C an hour and a target of 500 °C and left overnight. This means that by the start of the next day the substrate temperature had been sitting stably at 500 °C for a few hours. Typical chamber pressures at this temperature were high 10^{-7} mbar, which reduced to low 10^{-7} or high 10^{-8} mbar when the Meissner trap was activated. The Meissner trap was left to run for an hour with internal gas partial pressures monitored by a mass spectrometer. Water pressures could typically be reduced from a 90% contribution of total pressure to 30% (approximately equal to the pressures of N_2, O_2 and CO_2 present).

After this, the mass spectrometer was turned off and each material target was pre-sputtered for 5 to 10 minutes to remove any potential oxide that might have formed on its surface. This involves powering the magnetron gun at approximately 10% higher power than the planned growth power and reducing the Ar gas pressure by 20%. These combine to widen the area of the target that the Ar^+ ions impinge on, which guarantees that the pre-sputter will clean areas that are about to be sputtered. The Pt seed layers were then grown with a power of 12 W which resulted in a rate of about 1.3 Å/s. The desired seed layer thickness was controlled by varying the time of deposition. Values of 1, 3 and 5 nm were typically used. The Ar pressure during growth was 5×10^{-3} mbar. These parameters were selected based on previous work in the group [107] and then calibrated in this deposition chamber until high quality epitaxial growth was achieved.

With these seed layers deposited, the substrate temperature was then reduced to 450

°C over the next fifteen minutes (a rate of 200 °C an hour). This temperature was selected through the growth of a series of samples between 400 °C and 500 °C, with steps of 10 °C and measuring the resulting films with XRD to optimise for the intensity of characteristic reflections. Once this temperature of 450 °C was reached, the system was allowed to sit for an extra hour to ensure stability before the main growths were started. After a presuputtering of fifteen minutes, the Fe and Sn magnetron guns were simultaneously turned on with the Sn gun having a power of 10 W and the Fe varying depending on stoichiometry desired but with a typical power of about 35 W. Each sputter deposition system is unique, and so in order to find the ideal power to feed each magnetron gun, a series of calibration samples has to be created. By changing the power fed to the Fe magnetron gun in steps of 1 W, eventually the power that leads to the optimal growth rate to stoichiometrically balance with the rate being provided by feeding 10 W to the Sn gun. It's worth noting, Sn has a very low melting point and a fast rate of growth and therefore there is less incremental control over the growth rate from the Sn gun than the Fe gun which is why the Fe gun was selected as the one to vary. The Ar pressure during growth was 5×10^{-3} mbar and temperature was monitored throughout for any fluctuations.

After completing the growths, the system was set to room temperature at 200 °C an hour but due to the thermal mass of the system (and Newton's law of exponential cooling) at least six hours would be required for the system to return to room temperature and so often it was left overnight. In the morning, the final capping layer for the film was grown either from Pt or from an alloy target of Al_2O_3 depending on the eventual purpose of the grown film. Due to Al_2O_3 being an insulator the AC magnetron source was required for this material resulting in a growth rate of only 0.1 Å/s.

3.3 X-ray Crystallography

X-ray crystallography is the use of X-ray radiation to probe the crystal structure of materials. The X-rays are produced by accelerating thermionic electrons, produced by heating a tungsten filament, into a target. These electrons interact and provide energy to the target atom's inner core electrons. If these electrons are provided enough energy to leap up past the Fermi surface, the resulting cascade down into the now empty low lying energy level produces X-rays of characteristic frequency for the atom, the X-ray spectrum. In our case, copper is used, and a monochromator selects specifically the K-α component which has a wavelength of 1.540 Å.

3.3.1 X-ray Diffraction

X-ray diffraction (XRD) is the use of angle scans, typically with $2\theta \geq 10°$, to capture an X-ray diffraction pattern produced by the scattering interaction between the X-ray photon and the periodic crystal lattice.

Due to its usefulness later when talking about electron diffraction, we will quickly consider the general form of quantum mechanical scattering. We can use Fermi's Golden Rule for the transition rate Γ from state $\mathbf{k}_{\text{in}}$ to $\mathbf{k}_{\text{out}}$:

$$\Gamma = \frac{2\pi}{\hbar} |\langle \mathbf{k}_{\text{out}} | \, V(\mathbf{x}) \, | \mathbf{k}_{\text{in}} \rangle|^2 \delta(E_{\mathbf{k}_{\text{out}}} - E_{\mathbf{k}_{\text{in}}}), \tag{3.1}$$

where $V(x)$ is the scattering potential and the final Dirac delta ensures that only scattering that conserves energy $E_{\mathbf{k}_{\text{out}}} - E_{\mathbf{k}_{\text{in}}} = 0$ is allowed. This equation assumes that the potential $V(x)$ is weak and that it's interaction with the states is very brief.

If the scattering potential is weak, it is reasonable to assume that both incoming and outgoing states must be plane waves of the form $|\mathbf{k}\rangle = Ae^{i\mathbf{k}\cdot\mathbf{x}}$. In this case, it follows quickly that the bra-ket in equation (3.1) will be equivalent to the Fourier transform of the potential $V(\mathbf{x})$ written in wavefunction notation as:

$$\langle \mathbf{k}_{\text{out}} | \, V(\mathbf{x}) \, | \mathbf{k}_{\text{in}} \rangle = \int V(\mathbf{x}) e^{-i(\mathbf{k}_{\text{out}} - \mathbf{k}_{\text{in}})\cdot\mathbf{x}} \mathrm{d}^3\mathbf{x}. \tag{3.2}$$

For a crystal, we expect this potential $V(\mathbf{x})$ to be produced by the periodic arrangement of atoms, and so it itself must be periodic i.e. $V(\mathbf{x}) = V(\mathbf{x} + \mathbf{r})$ where $\mathbf{r}$ is some lattice vector. The Fourier transform of any periodic function is zero, except for exactly the places where $(\mathbf{k}_{out} - \mathbf{k}_{in}) \cdot \mathbf{r} = 0$ which is the requirement for $(\mathbf{k}_{out} - \mathbf{k}_{in})$ to be the reciprocal lattice vectors for the crystal.

This leads to the powerfully simple Laue's law [27]:

$$\Delta\mathbf{k} = \mathbf{k}_{\text{out}} - \mathbf{k}_{\text{in}} = \mathbf{G}, \tag{3.3}$$

where $\mathbf{k}$ is the wavevector of the X-rays before and after scattering and $\mathbf{G}$ is a reciprocal lattice vector. What this relationship says is that momentum transfer to or from the X-ray can only occur in ways that scatter from one reciprocal lattice point to another. Figure 3.3 shows this relationship and how it relates to the geometry of the scattering in real space. It now becomes clear that an X-ray diffraction experiment is the act of sweeping (2)θ to find the points of constructive interference where $\Delta\mathbf{k} = \mathbf{G}$. Since for our wavevectors we have

$|\mathbf{k}_{\text{out}}| = |\mathbf{k}_{\text{in}}| = \frac{2\pi}{\lambda}$ and $|\mathbf{G}| = \frac{2\pi}{d}$ with the application of some vector algebra or geometry, we can quickly find that:

$$\lambda = 2d\sin(\theta). \tag{3.4}$$

This is, of course, Bragg's law (ultimately an identical condition to equation (3.3)) through which we can relate the appearance of constructive maxima in a diffraction pattern with the repeat spacings d between the lattice planes of the crystal. Also note, the index "n" that often appears in Bragg's law is not required so long as we appreciate that the origin of constructive interference comes from reciprocal lattice vectors that will always be part of a collinear family (e.g. for every $\mathbf{G}$ there must always be a $2\mathbf{G}, 3\mathbf{G}$, etc. that all must then correspond to $\frac{2\pi}{2d}, \frac{2\pi}{3d}$ and so on). Since we are directly probing the separation between atomic planes, this technique is perfect for material characterisation as well as assessing if a grown film is under stress which has adjusted its lattice constants.

A final consideration is the experimental broadening present in any diffraction pattern. If we recall (3.2) and its consequences, we expect the diffraction pattern to be associated with the Fourier transform of the crystal lattice. For an infinite lattice and a perfect monochromatic wave all broadening would be reduced down to the level of the uncertainty principle on the positions of the atoms. In practice of course, many effects broaden the diffraction peak, the most important of which being the finite size of the crystallites that are producing the diffraction patterns.

This means that we can use the broadening on a peak to estimate the crystallite size, τ, within the sample, with the most common equation being given by Scherrer [108]:

$$\tau = \frac{K\lambda}{\beta\cos(\theta)} \tag{3.5}$$

where K is a shape factor with typical values between 0.8 and 1 for thin films; λ is the wavelength of the X-rays, 1.54 Å in our case; θ is the angle of the diffraction peak maxima; and β is the Full Width at Half-Maximum (FWHM) of the peak measured in radians. It is worth noting that equation 3.5 relies on a series of underlying assumptions, the primary ones being that the crystallites are the only source of broadening present in the XRD features; and that all crystallites are isotropic and evenly distributed within the sample.

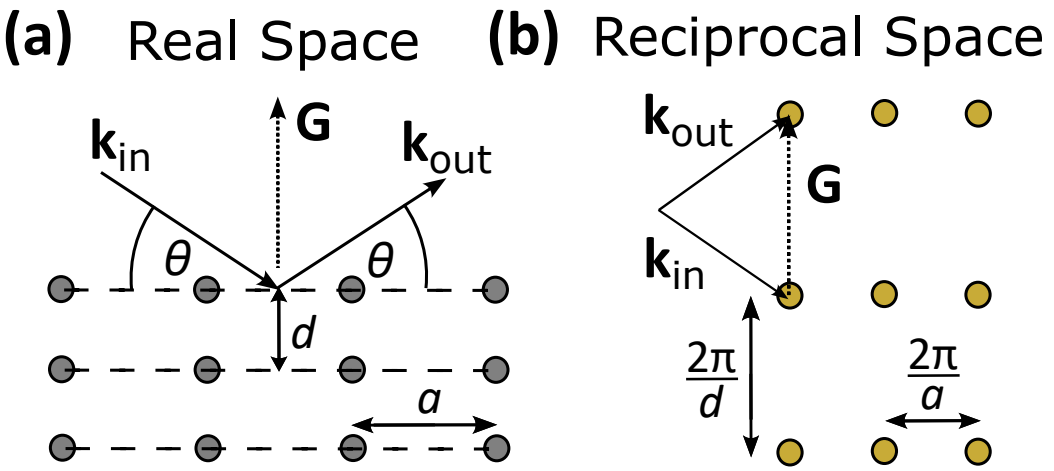

Figure 3.3: Diagram of a scattering interaction highlighting the importance of the reciprocal lattice vector. (a) shows the real space lattice and the geometry with the scattering plane waves $\mathbf{k}_{out}$ and $\mathbf{k}_{in}$. (b) shows the resulting reciprocal space where $\mathbf{G}$ is a reciprocal lattice vector. Inspired by a diagram found in book of S. Simon [26].

3.3.2 X-ray Reflectometry

X-ray reflection (XRR) is the use of angle scans, typically $2\theta \leq 10°$, so that the incident X-ray beam has a specular reflection from the sample surface into the detector. This measurement is surface sensitive but is also particularly revealing of thin film thicknesses and interfaces between layers that offer boundaries for reflection of the X-ray beam. Other features such as the critical edge; Bragg peaks; and rate of fringe decay can indicate film composition, layer stacking and roughness.

In the case of a single slab of film, an XRR scan will take on a series of peaks, known as the Kiessig fringes caused by the interference between X-rays reflecting off the top of the film and those reflecting off the film-substrate interface [109]. Assuming negligible absorption of the X-rays, the separation between subsequent Kiessig fringes thus provides a way to calculate the film thickness:

$$d = \frac{\lambda}{2}\sqrt{\frac{2n+1}{\theta_{n+1}^2 - \theta_n^2}}, \tag{3.6}$$

where d is the film thickness and θ_n the angle to the n^{th} peak. So by measuring and plotting the separation between subsequent peaks, the thickness can be found as shown in the inset in Figure 3.4.

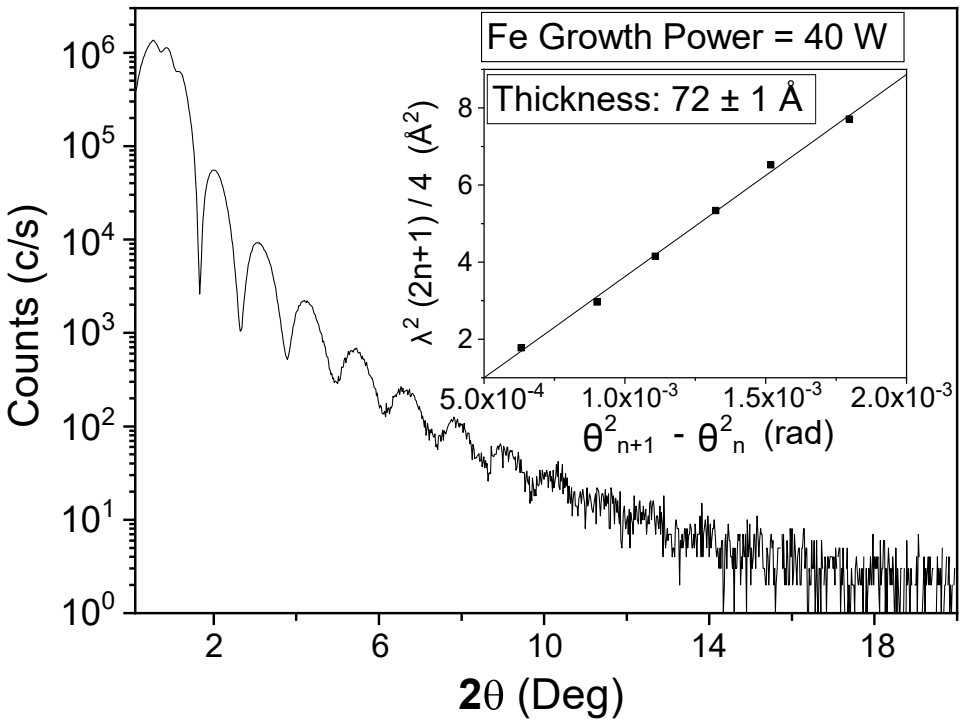

Figure 3.4: XRR measurement of an Fe-Sn film with Fe growth power 40 W. Kiessig fringes extending up to at least 12 degrees are visible. The inset shows the separation between subsequent peak maxima plotted in accordance with equation (3.6) from which the thickness can be extracted (as the square root of the gradient).

3.4 Electron Microscopy

3.4.1 Transmission Electron Microscopy

Transmission Electron Microscopy (TEM) is an invaluable tool for the analysis of the chemical and crystallographic content of systems in condensed matter physics. The basic concept is relatively simple: an optical photon with wavelength of the order of 500 nm cannot interact with an atom of diameter 0.1 nm (at least in a deterministic fashion). An electron, however, has variable wavelength dependent on its energy, so by driving it to 100 keV its wavelength can be reduced to about 3.7 pm, easily enough to fall under the atomic scale diffraction limit.

To achieve an interpretable resolution from the transmission of electrons through a sample the area being imaged must have a thickness of 100 nm at an absolute maximum and ideally less than this would be achieved. Preparing a thin lamella like this can be performed using a Focused Ion Beam (FIB) to first extract a small region from a film of interest and then thin it down until it is a suitable thickness for imaging.

In practice these electrons need to be focused using a series of magnetic lenses to produce the beam that will interact with a sample. Since the objective lens in an electron microscope is cylindrically symmetric, the spherical aberration that is infamous from classical optics will always occur. Using a complex system of magnetic lenses a slight divergence can be introduced to the beam (magnetic lenses are typically only converging) which can be used to reduce the spherical aberration producing an aberration corrected image that can achieve the desired atomic scale resolution.

A final experimental process that is worth discussing is the use of a precessing electron beam for the gathering of diffraction patterns which are then known as Precession Electron Diffraction (PED) patterns. These are obtained by directing the electron beam to be slightly tilted from the central axis and then set precessing so the final pattern is the integrated sum over all the resulting patterns. The simple scattering analysis of section 3.3 which is highly accurate for the case of a photon (described as kinematic scattering) begins to weaken significantly for the much more dynamic case of an electron interacting with a crystal lattice where complex scattering events such as channelling or forbidden reflections may occur. These dynamic effects are highly dependent on the angle of incidence of the electron beam, so a precessing measurement significantly reduces their influence by averaging over a large range of incident angles returning us to a more kinematic scattering condition as well as providing a much wider view of reflections beyond the zero-order Laue zone [110].

3.4.2 Scanning Transmission Electron Microscopy

Scanning Transmission Electron Microscopy (STEM) uses the principles of TEM, but rather than illuminating the sample with a parallel beam of electrons, the beam is instead brought into focus on the sample so that only a small spot size is illuminated. This spot is then scanned across the sample, and the transmitted electrons from each point are recorded on the detector. Using a pixelated electron detector it is possible to collect an entire electron diffraction pattern from the sample for each pixel of the scanned region. This process is often called 4D-STEM as the resulting data set records an intensity based on four coordinates: the real space x and y for the location of the scanning electron beam; and the reciprocal space k_x and k_y for the location in the diffraction pattern.

It is useful to think of the resulting image formed on the detector in reciprocal space in three parts: the first is the direct beam, a bright central spot often indexed (000) from electrons that were neither scattered nor diffracted from the atoms in the material. The intensity and shifts in this central beam can be used to gather electrical and magnetic information from the sample. The second is the Low-Angle Annular Dark Field (LAADF) which is the band (or annulus) whose centre excludes the direct beam, and whose outer limit stops just past the highest angle diffraction spots produced through Bragg diffraction. An image produced by integrating over this band will highlight areas of high crystallographic quality. The final region is the High-Angle Annular Dark Field (HAADF) which captures all electrons that fall beyond the area dominated by Bragg diffraction. To understand this, we can return to the analysis of equation (3.2) and remember that all elastic scattering is the Fourier transform of the potential in real space.

A reasonable model of the periodic atomic potential is the convolution of a single atomic potential, $V(\mathbf{r}) = \frac{kQ}{|\mathbf{r}|}$, with the Dirac Comb function with Dirac points at each atomic site, the results of which are shown in Figure 3.5 for just the x-axis. A basic principle of the Fourier transform is that short-range features in real space transform to high-angle scattering in momentum space and vice versa. So, if we look at low angles on our detector, we see the coherent Bragg diffraction from the interaction of many periodic atomic potentials. If we look at high angles, we begin to see only the scattering coming from our short-range single central potential. Of course we actually have many electrons scattering off many atoms, but altogether at short range in real space these interactions have no phase relation to each other, so the eventual high-angle scattering is purely statistical (to first order) and is just the classical Rutherford scattering with a Z^2 dependence on electron number of the scattering atom.

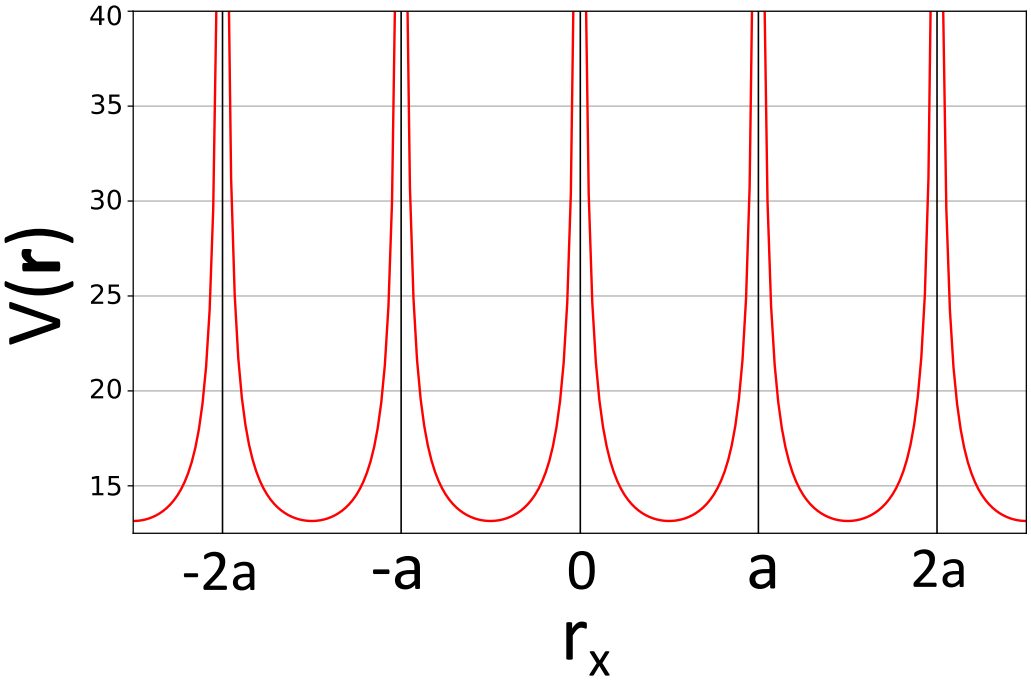

Figure 3.5: The convolution of the $\frac{kQ}{r}$ Coulomb potential with the Dirac comb (showing only the results along the x-axis for clarity). The convolution has effectively copied the individual atomic potential periodically along the axis.

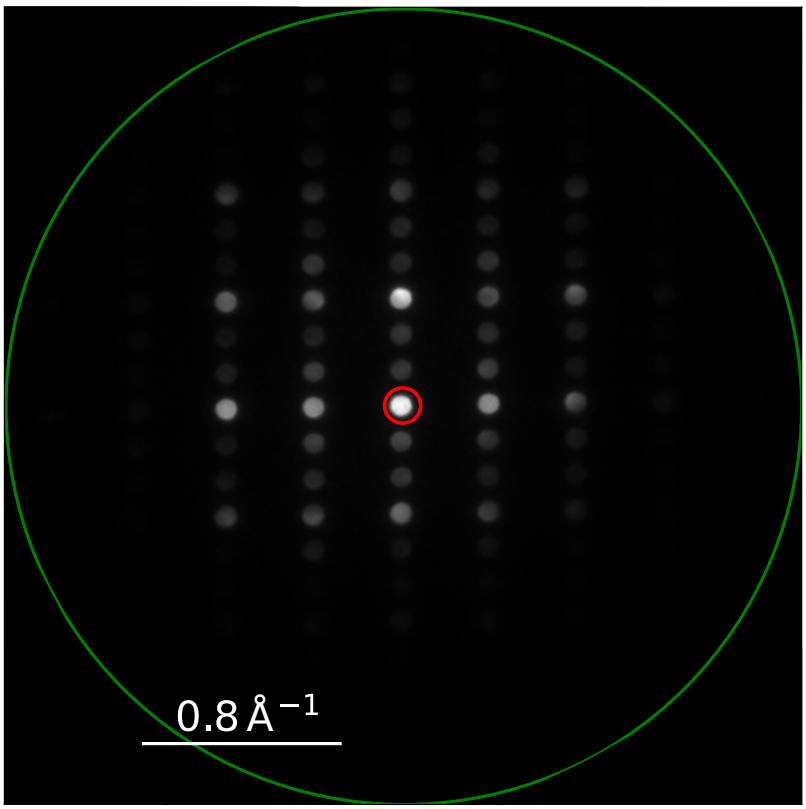

Figure 3.6: Image from a single point in real space of an Fe_3Sn_2 film using STEM. The region within the red circle is the direct beam. Between the red and green circles the PED diffraction pattern is present so integrating over this region will produce a LAADF image. Beyond the green circle, any electron counts will be due to incoherent scattering forming the HAADF image.

In practice, all this data has been gathered by the detector and we can produce a desired image by selecting which areas of the whole detector we choose to extract data from (described as creating a virtual detector). An example of selected regions for a virtual detector is shown in Figure 3.6. Due to the spot diffraction extending to a reasonably high angle (almost to the edge of the detector) HAADF images in this work are produced by subtracting the number of electrons within some annulus that contains the PED pattern from the estimated total number of electrons in the incident beam (as calculated from the beam current). In some ways, we should think of this as measuring all the electrons *not* captured by the detector as these have been scattered to very high angles.

STEM measurements within this work were performed both at the University of Leeds and by collaborators at the University of Glasgow.

All data used in diffraction spot analysis, phase mapping, and EDX spectroscopy was collected on the Tensor Tescan 4D-STEM system at the University of Leeds. A beam current of 1 nA was used with acceleration voltage of 100 keV, resulting in a 3.88 pm wavelength and 2.2 nm spot size. This is importantly smaller than the 3 nm step size which is the distance the beam moves before a new detector measurement is taken (effectively the pixel size in the resulting image). This means that there is no overlap in evaluated regions. High-resolution STEM measurements were performed on the JEOL ARM200cf microscope at the University of Glasgow with an acceleration voltage of 200 keV and probe size down to 0.1 Å.

3.4.3 Energy Dispersive X-ray Spectroscopy

Energy Dispersive X-ray Spectroscopy (EDXS) makes use of the electron beam interacting with an atom's inner core electrons to produce X-rays, identical to the method of X-ray generation described in section 3.3. There, we used a sample of Cu to generate a set of X-rays of a known wavelength; for EDXS, we use the characteristic energies of the X-rays produced by the atoms in the sample when interacting with the electron beam, in order to determine the elements present within the sample from the X-ray spectrum.

When used in a S/TEM, this allows us to form a map of the elemental composition within a film, showing regions of higher and lower concentration of some elements. Due to the fact that many elements have overlapping X-ray spectra, it is a requirement to already have a good idea of which elements are present in a sample to narrow down the elemental search being performed.

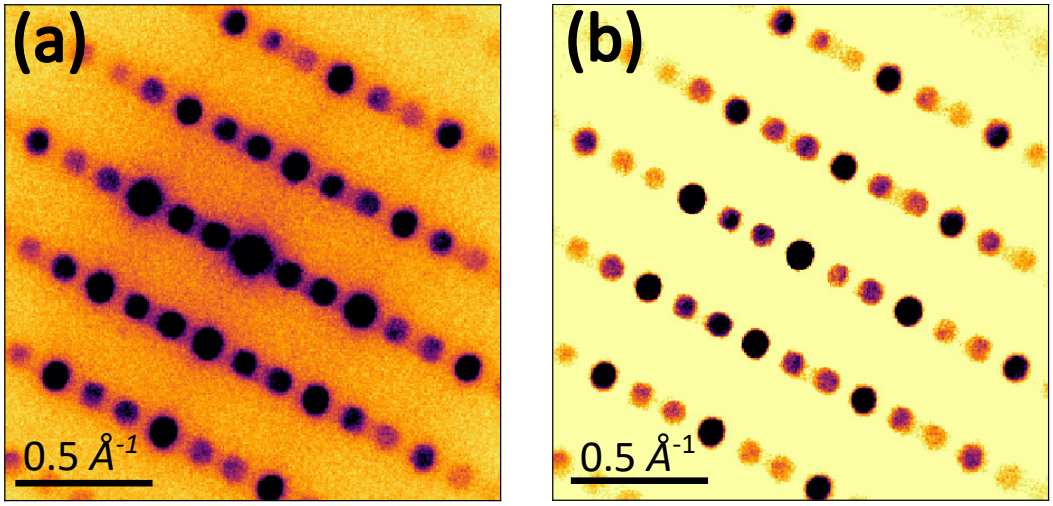

Figure 3.7: (a) PED pattern from an Fe_3Sn_2 thin film before any preprocessing has been applied. (b) The resulting image from running a DoG subtraction on (a), notice how the grainy background and the suffuse halo around each spot has been removed.

3.5 Template Matching

In order to produce a phase map of a given film a method has to be used to assign a given pixel from the STEM image to either one phase or another. The method selected in this work was a process of template matching, where simulated images of the potential spot diffraction patterns from the different phases are produced and then cross correlated to the experimental images in order to assign a correlation value which indicates which phase is the most likely to be present for a given diffraction pattern. All the following process was performed using the Pyxem extension of the Python Hyperspy package. Crystallographic data for the Fe-Sn phases were initially taken from the work of H. Giefers and M. Nicol [22], with adjustments that will be discussed in the relevant chapter.

3.5.1 Preprocessing

As an initial step, cross sections of the film that contained substrate, the Pt seed and capping layers and the Fe-Sn film itself were cropped to smaller regions containing just the Fe-Sn material. This reduces the complexity of any future matching to be done.

A Difference of Gaussian (DoG) subtraction was then performed in which the experimental image is convolved with a function that is the difference between two Gaussian functions.

Such a convolution on a single Gaussian would act as a low bandpass filter attenuating any high frequency spatial information, while convolving with the difference between the two is a bandpass filter that attenuates both low and high frequencies. An intensity floor was also implemented which removed any signal below a given cut off threshold and magnified any signal remaining. This preprocessing removed any spot noise or halo effects around the diffraction spots and were significant for improving the eventual fitting results. The result of such filtering can be seen in Figure 3.7 where the difference in background noise is apparent.

3.5.2 Generating the Diffraction Library

To generate a library of potential electron spot diffraction patterns for the different phases there are really only two pieces of information needed: the crystallographic structure of the phase and how that crystal will be orientated in space, known as the zone axis.

A CIF file contains all the crystallographic information Pyxem needs to generate a PED pattern and so all that is required is to select the range of zone axes that we'd like to simulate. Although the growth conditions lead us to suspect a particular zone axis to be dominant there will always be slight variations due to possible grain boundaries; how the lamella was cut; or any warping it has then experienced.

If we wanted then to have a diffraction library that can account for this, we need to simulate some other possible zone axes. A primitive (and computationally inefficient) method would be to just simulate the entire solid angle sphere of possible angles, then we know that any possible rotation has been covered. An improvement on this can be obtained by using the symmetry of the crystal. Fe_3Sn_2 for instance has trigonal symmetry, which means it should be invariant under rotations around its c-axis by 120° and so only polar angles in this range need to be simulated (with azimuthal angles ranging from 0° to 180°). Figure 3.8 shows an example of points sampled on a solid angle represented in stereographic projection (what you would see if viewing points evenly distributed on a sphere from a bird's eye view). Each of these points can then be used to generate a rotation for the crystal and a resulting PED pattern. For a high resolution mesh, this process can take quite a long time. Fortunately, once the diffraction library has been generated, it can then be saved and called upon as needed, reducing future matching efforts.

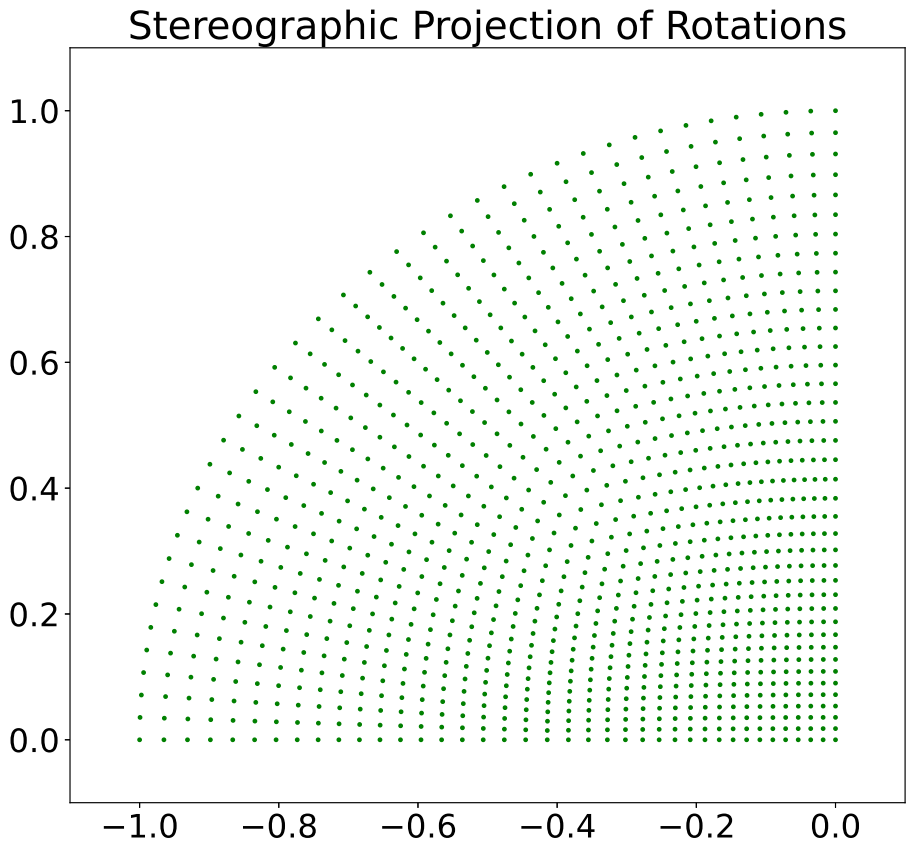

Figure 3.8: Stereographic projection of a set of angles on the unit sphere for the Fe_3Sn_2 space group R-3m. Due to the symmetry, only the North-West quadrant of the Wulff Net needs to be included. For image clarity the solid angle separation between each point is 3°, though for the actual template matching a separation of 1° was used.

3.5.3 Correlate Data to Library

With the library generated it is then possible to compare each element of the library to any given piece of STEM data and return a correlation value between the two. The highest correlation corresponds to the image of the library that matches best to the experimental image. The procedure behind this is that the experimental image is divided into annular slices corresponding to different radii. Since the polar coordinates (radius and angle) to all the simulated spots are known, it is possible to rotate each radial slice by the known angle of the spots and sum the result. If the experimental image has a high count rate at the correct radii and angles, i.e. there are diffraction spots at all the same coordinates as the simulated spots, the resulting intensity sum will be large which we can use as the correlation. If there is a poor match, we will mostly add just background intensities and the resulting correlation will be small. From here, it becomes straightforward to produce a phase map where each pixel is assigned to either FeSn or Fe_3Sn_2 depending on which phase can produce a PED pattern with the strongest correlation to the data.

Since a correlation value is returned not just between the best match, but between every single template and the data (so the best correlation can be found) it is also possible to assign a confidence value for the phase matching of each pixel.

To do this, we can contrast the correlation value for the phase selected, to the best correlation value found for the other phase using the formula:

$$C = \left(1 - \frac{\rho_1}{\rho_0}\right), \tag{3.7}$$

where ρ_1 is the correlation value for the second-best pattern match, and ρ_0 is the correlation value for the best match. The overall steps of the whole process are shown in Figure 3.9. Once the final phase map is produced, a quick scan through by eye can confirm whether the template matching process has been successful. Most often serious errors in final phase maps were produced by poor preprocessing, leading to spurious correlations between the simulated diffraction library and the data.

3.6 Magnetometry

A Vibrating-Sample Magnetometer (VSM) is a device for measuring the magnetic properties of a material. To do this, a sample of the material is placed in a strong magnetic field to magnetise it. Then, by physically oscillating the sample, the dipole moment of the sample is measured

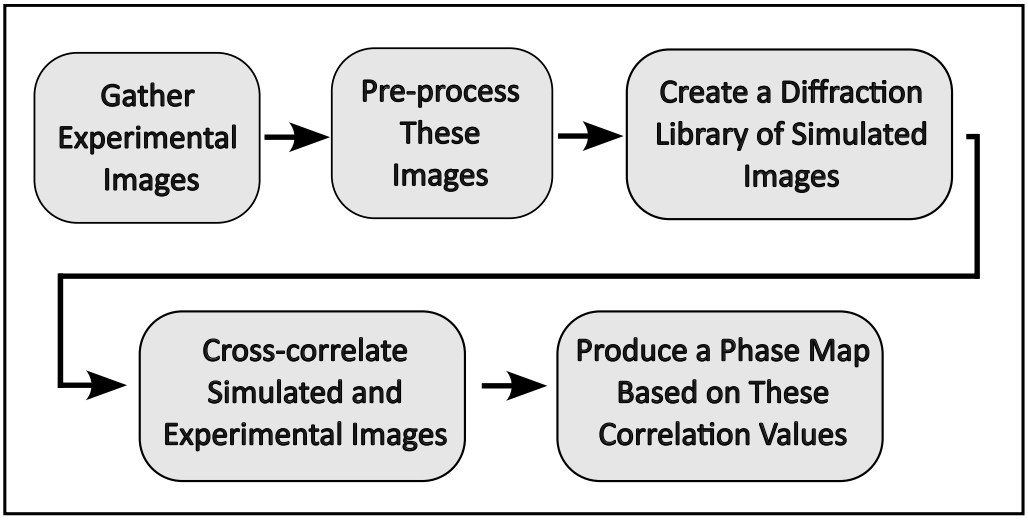

Figure 3.9: Basic workflow of the template matching process.

through the induced current it produces in a set of detector coils. The Faraday effect which induces the current is well known and the voltage is given by:

$$V_{ind} = \sigma G A 2\pi f \cos(2\pi f t) \tag{3.8}$$

where V_{ind} is the induced voltage; σ is the magnetisation we are trying to measure; G is a factor that depends on the geometry of the coil; and A and f are the amplitude and frequency of the oscillations respectively [111]. Through the use of a Superconducting Quantum Interference Device (SQUID) detector circuit, that operates through a pair of Josephson junctions, magnetic fields down to a single flux quanta can in theory be detected [112].

Samples are attached to a quartz rod in an In-Plane (IP) orientation through the use of a small amount of adhesive. For Out-Of-Plane (OOP) measurements, samples are loaded into a plastic straw such that their four corners are in contact with the straw. In order to be contained completely within the uniform magnetic field detection region, samples can not be significantly larger than 4 mm by 4 mm. As growth is performed on 8 mm by 8 mm substrates, this requires the samples to be cut to size, which introduces the largest source of error present in a SQUID VSM measurement, that being the uncertainty in the volume of the sample being measured. In order to reduce this uncertainty, the area of the films is measured through triplicate pixel count on an image taken of the sample after cutting and the thickness is calculated through XRR measurements as described in Section 3.3.

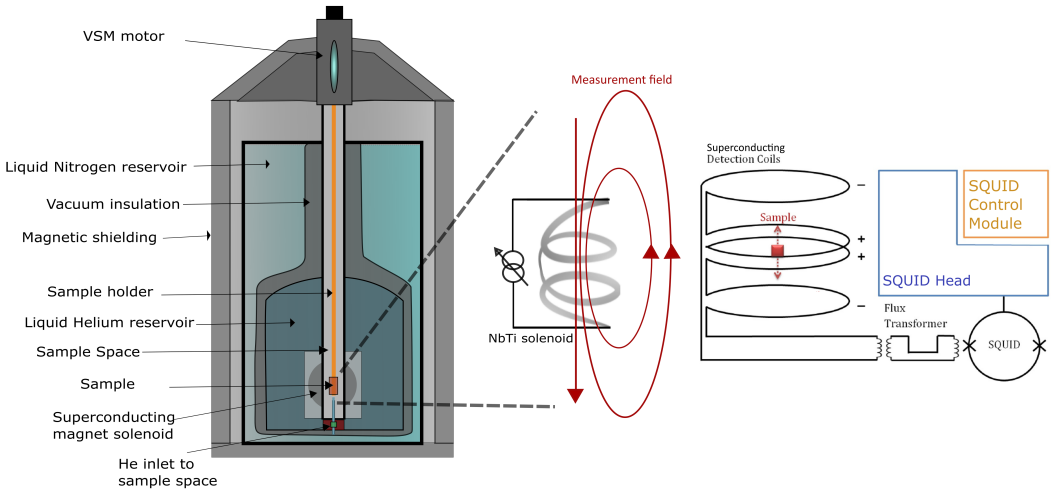

Figure 3.10: Simplified diagram of VSM set up with Superconducting Quantum Interference Device (SQUID) detector circuit. Lightly adapted from the diagram of S. Gupta [104].

Since a magnetic sample will often enter the SQUID VSM having already been magnetised in a particular direction, it is always useful to run a demagnetisation process on a sample before beginning measuring. This involves applying a large magnetic field to the sample, and then allowing that magnetic field to return to zero but with significant oscillations into negative field and back again so that the individual domains and moments within the sample experience being switched back and forth which will gradually disorder them as the field reduces. Samples can often be returned to less than 1% of their saturation moment by following this technique.

The final major consideration is the shape factor correction (Darwin correction) [113] that arises from the unique shape of each sample. This correction factor is a function of whether the sample is mounted in-plane or out-of-plane; the surface area of the sample; and the frequency of the oscillations of the sample within the detector coils. The calculations of these values can be found in Appendix B.

3.6.1 Hysteresis Loops

The most common measurement performed on the SQUID VSM is a hysteresis loop of moment against field. Figure 3.11 is an uncorrected measurement. The large step as we pass from positive to negative field is the ferromagnetic contribution from the Fe_3Sn_2. In addition to this, there is a linear background (in this case negative) mostly arising from the diamagnetic

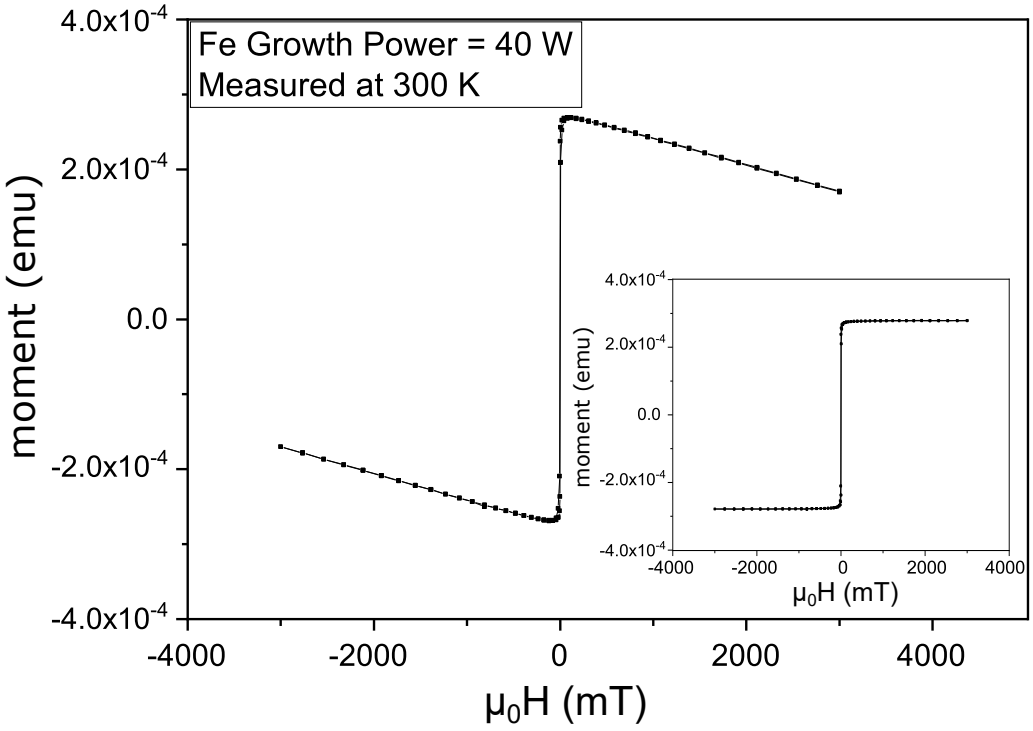

Figure 3.11: Uncorrected hysteresis loop measured on the SQUID VSM. The inset shows the resulting corrected loop once the linear background has been subtracted and the shape factor correction (typically only a 1-5% adjustment) has been applied.

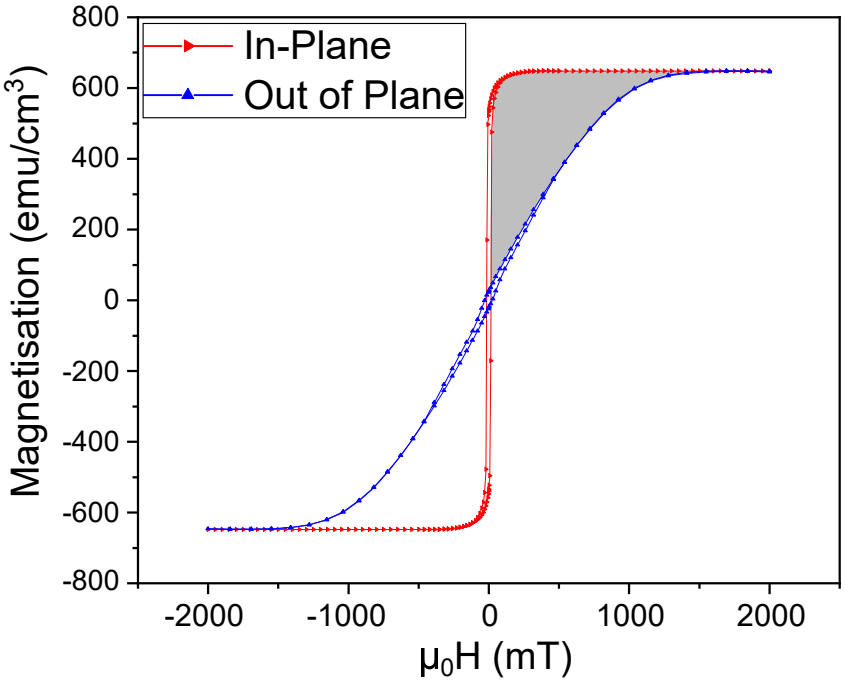

Figure 3.12: IP and OOP magnetisation hysteresis loops that have been brought into agreement at saturation using the shape factor correction. The effective anisotropy between the easy and hard axis can be found by integrating over the area contained between two loops indicated by the grey area.

sapphire substrate but also containing small contributions from any other material present with a linear response such as the quartz or plastic of the sample holder; the adhesive that holds the sample in place; or any contaminant dust. Once accounted for through simply adding (or subtracting) the necessary gradient, the coercivity and remanent moment can be extracted from a loop from the x-axis intercept, y-axis intercept respectively.

The saturation magnetisation of a sample can be found by taking the saturation moment (the unchanging moment at high field) and dividing by the sample's volume. Figure 3.12 shows the IP and OOP magnetisation vs field loop that results. Since this particular film has its easy axis in plane a smaller field is required to reach the magnetic saturation in this direction. We can measure this effective anisotropy, K_{eff}, by integrating the area between the IP and OOP curves indicated by the grey area:

$$K_{\text{eff}} = \mu_0 \int_0^{H_0} (M_{\text{easy axis}} - M_{\text{hard axis}})\, dH \ . \tag{3.9}$$

For a thin film, this effective anisotropy is the sum of the inherent uniaxial anisotropy coming from the crystal structure and the shape anisotropy produced by the geometry of the film.

3.6.2 Zero-Field Cooled / Field Cooled Measurements

Rather than measuring magnetic moment vs field as in a hysteresis loop, it is also possible to measure magnetic moment as temperature is changed in a fixed magnetic field. This leads to a measurement technique known as Zero-Field Cooled/Field Cooled (ZFC/FC) measurements. This name can be confusing, and so it is worth remembering that this title refers to the *state of preparation* for the measurement. In other words, ZFC measurements are performed after the sample has been demagnetised and then cooled in no external field. After this, an external field is applied at the low temperature and the measurement begins as the sample is warmed up. The low temperature will often result in moments and domains remaining "frozen" as even within the magnetic field, they lack the energy to reorientate until the temperature rises to a particular point. Differences can be drawn during the FC step, where the sample is now cooled in an external field and the effect of this external field on the moment can be measured in the changing temperature.

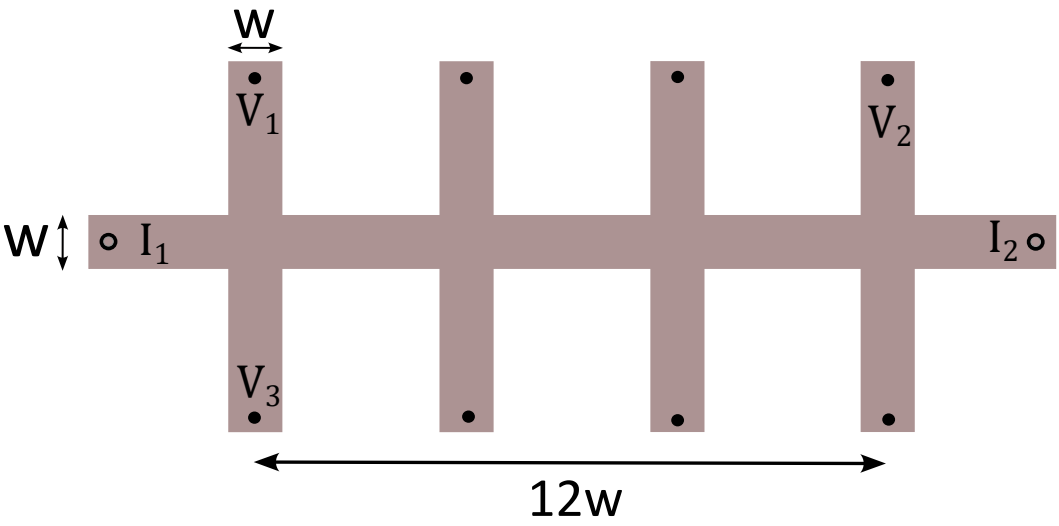

Figure 3.13: Diagram of a typical Hall bar used in this work (before gate deposition). I_1 and I_2 indicate the locations for current source and sink. R_{xx} measurements are made by measuring voltage longitudinally such as between the arms V_1 and V_2. R_{xy} measurements are made measuring the voltage transversely such as between V_1 and V_3. In all cases $w = 0.25$ mm.

3.7 Clean Room Fabrication

A Hall bar geometry is desirable for electrical measurements due to the simplicity it offers in analysing the measured resistances. Due to the growths being performed at high temperatures, depositing through a masking shape directly in the form of a Hall bar was not possible. Instead, sheet films were deposited and then milled into the Hall bar pattern using a SCIA ion miller in the Leeds Nanotechnology Cleanroom. A wet etch process was also attempted using hydrochloric acid, sulphuric acid, and aqua regia in turn. This method was unsuccessful due to the Pt seed layer present in all the films which was of such high quality that before even 5 nm of it could be etched away, the films would suffer such severe side attack into the Fe-Sn walls, that the entire film would float off the still untouched Pt layer.

In order to produce the desired geometry, a protective layer of positive photoresist S1813 was coated onto the samples using a spin coater. This can then be precisely exposed to UV light which acts to weaken the chemical crosslinking in the resist so that it can be washed off using SVC-14 photoresist stripper. The remaining unexposed resist acts as a thick protective layer so the ion miller can only attack certain areas of the film.

After the basic Hall bar shape is produced, it was then possible to apply a top gate to the

structure by first depositing a dielectric layer of Al_2O_3 using Atomic Layer Deposition (ALD), followed by forming the lithography for a gate and contact pattern and then evaporating a layer of gold through this to form the top gate. The SVC-14 photoresist stripper is hydroxide based which will attack the alumina dielectric and risk leaving pinhole defects in what needs to be a continuous layer. In order to avoid this, a more complicated bilayer resist process was used where a layer of PMMA 405 K A8 photoresist was first spun onto the surface followed by the S1813. This bottom layer can then protect the alumina while the lithography for the gate electrodes is performed.

The gate electrodes themselves are formed of 10 nm of Ti followed by 90 nm of Au. The Ti acts as an adhesion layer to reduce the chance of the Au contacts breaking loose during the final preparation steps. Cr-Au is actually a more common combination to use, but Cr_2O_3 is known to be an antiferromagnet [114] so was avoided.

3.8 Electrical Transport

A cryostat is a piece of equipment used to perform transport measurements on a material at a range of temperatures between room temperature and some lowest point known as the "base temperature." For a typical gas-flow cryostat this can be assumed to be the temperature achieved by pumping on liquid He, about 1.5 K. Electrical transport measurements in this work were primarily performed on an Oxford Instruments He flow cryostat. Figure 3.14 shows a cross section view of the cryostat with all key components labelled. Further work that involved changing the orientation of the sample within the cryostat was performed on Cryogenic Limited He flow cryostat, with a motorised set up that allowed for the automation of rotating the sample within a field.

An internal chamber known as the variable temperature insert (VTI) is surrounded by liquid He (which is itself isolated from the environment by a vacuum jacket and reservoir of liquid nitrogen). The VTI is maintained at a low pressure through a roughing pump which also acts to draw He gas through the needle valve and into the VTI. The temperature can then be controlled through the balancing of an electrical heater element at the base of the VTI; the pressure provided by the roughing pump; and the flow of He allowed into the VTI. The whole VTI is also surrounded by the coils of a superconducting magnet that can produce magnetic flux densities of up to 8 T. By loading the sample onto a sample stick that is then inserted into the VTI, it is possible to measure the electrical properties of a sample as a function of temperature and magnetic field. Through selection of a particular head for the sample stick it is

possible to mount the sample for both in-plane and out-of-plane magnetic field measurements.

The sample temperature is recorded from a Lakeshore 340 using a Cernox temperature sensor that is mounted within the sample head. Electrical transport measurements are performed via four terminals with a Keithley 6221 current source and either a single or pair of 2182 nano-voltmeters. These, along with the temperature and magnetic fields, are all controlled using custom software written in LabVIEW by Professor G Burnell.

3.8.1 Seed Layer Subtraction

Since all the films examined in this work were deposited upon a seed layer of Pt, when the thickness of the Fe_3Sn_2 film approaches the thickness of the seed layer, a sizeable proportion of the current will flow through the Pt rather than the Fe_3Sn_2. The simplest model is to imagine the two films as being two resistors in parallel. By measuring the resistance, R_s, and the thickness, t_s, of a Pt seed layer individually, it is possible to then subtract its contribution from the overall total resistance, R_T (which is what we actually measure from a sample). So then the resistance of the Fe_3Sn_2 layer, R_f, will be given by:

$$R_f = \frac{R_T R_s}{R_s - R_T} , \tag{3.10}$$

or, in terms of resistivities:

$$\rho_f = \frac{t_f \rho_T \rho_s}{\rho_s t_T - \rho_T t_s} . \tag{3.11}$$

When we measure the magnetoresistance (MR), the change of the longitudinal resistivity, ρ_{xx}, with magnetic field, it is common to present the normalised change in resistivity calculated by:

$$MR = \frac{\rho_{xx}(B) - \rho_{xx}(0)}{\rho_{xx}(0)} . \tag{3.12}$$

Fortunately, the MR of the Pt seed layer is only 0.1% at 3 K and reduces in magnitude for higher temperature which can be seen in Figure 3.16 b. The total MR of the films is found to be negative and of the order of -1% at 3 K with the entire negative contribution coming from the Fe_3Sn_2 layer. The uncorrected and the corrected MR with the Pt contribution subtracted is shown in Figure 3.16. Finally, by doing the subtraction of the seed layer presented above, the corrected MR with the Pt contribution subtracted is shown in Figure 3.16 (c).

For the transverse resistivity, ρ_{xy}, also known as the Hall resistivity, we aren't quite as fortunate. The contribution from the Pt seed layer is at least of the same order of magnitude as the relatively weak Hall effect in Fe_3Sn_2, and so must be taken into account.

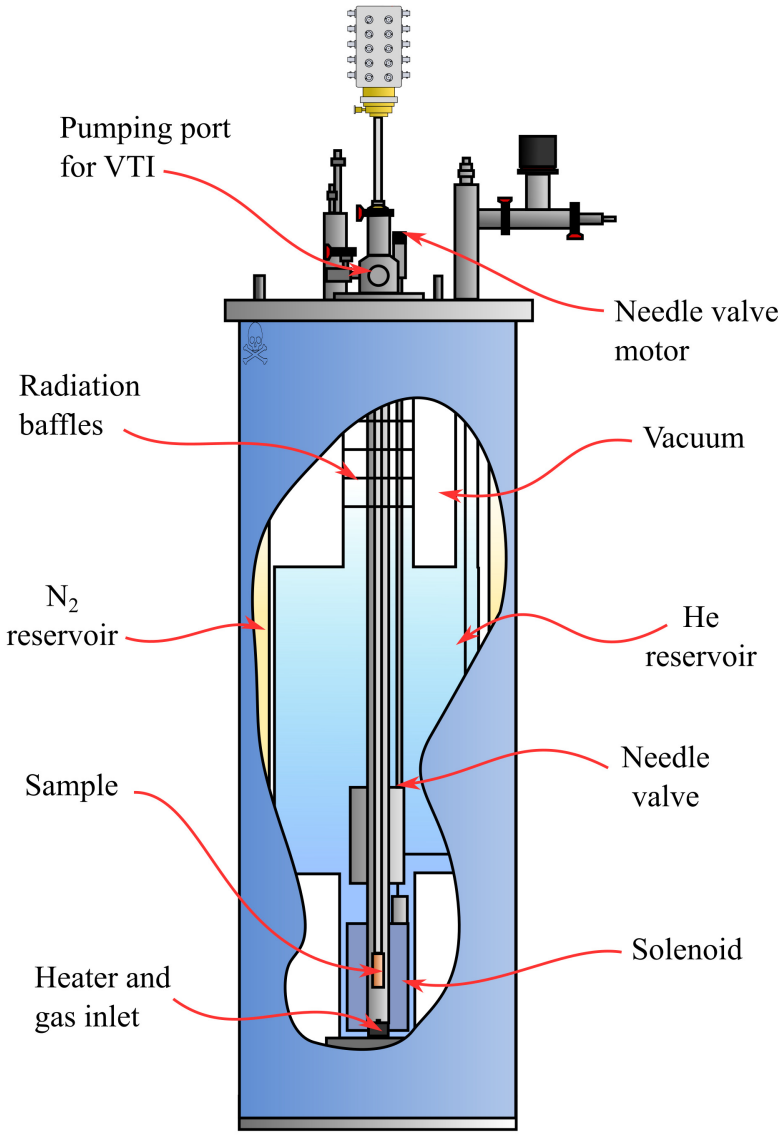

Figure 3.14: Schematic of the He flow cryostat showing the internal components. Lightly adapted from the diagram in the work of J. T. Batley [115].

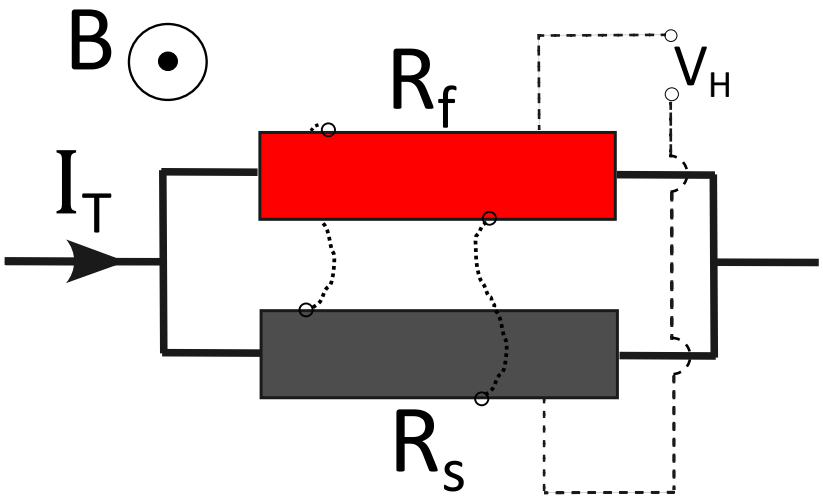

Figure 3.15: Schematic diagram for the two resistor model for a bilayer thin film with resistances R_f for the main film and R_s for the seed layer. The dotted lines indicate virtual wires that we can imagine connecting between the films and to the Hall probes.

To start, we can imagine two resistors wired in parallel in a shared magnetic field of flux density B. If a total current, I_T, is flowing into the configuration then we say a certain percentage of current, xI_T, flows through the resistor representing the Fe_3Sn_2 film and the rest, $(1-x)I_T$, flows through the resistor representing the seed layer. We can calculate this percentage by first measuring a pure Pt layer with the same thickness as the seed layer. Then, since the total resistance of the film is the reciprocal sum of the seed layer resistance and the Fe_3Sn_2 layer resistance, and we know the Pt seed layer resistance, we can reverse calculate the Fe_3Sn_2 layer resistance (and by extension the resistivity) on its own. Now if a wire were to connect the sides of the two resistors, as represented by the dotted lines in Figure 3.15, then it becomes clear that only one shared Hall potential can exist across the film, V_H, which is what we measure. This must be the potential that both layers are experiencing, and yet, if separated both layers would produce their own, different, Hall potential due to their own carrier properties. V_H is the sum of these individual Hall potentials (V_f and V_s) weighted for the percentage of the current flowing through that layer of the film:

$$V_\mathrm{H} = xV_\mathrm{f} + (1-x)V_\mathrm{s}\,. \tag{3.13}$$

Now, if we want to extract the resistance of just the Fe_3Sn_2 layer, we can rearrange this to give:

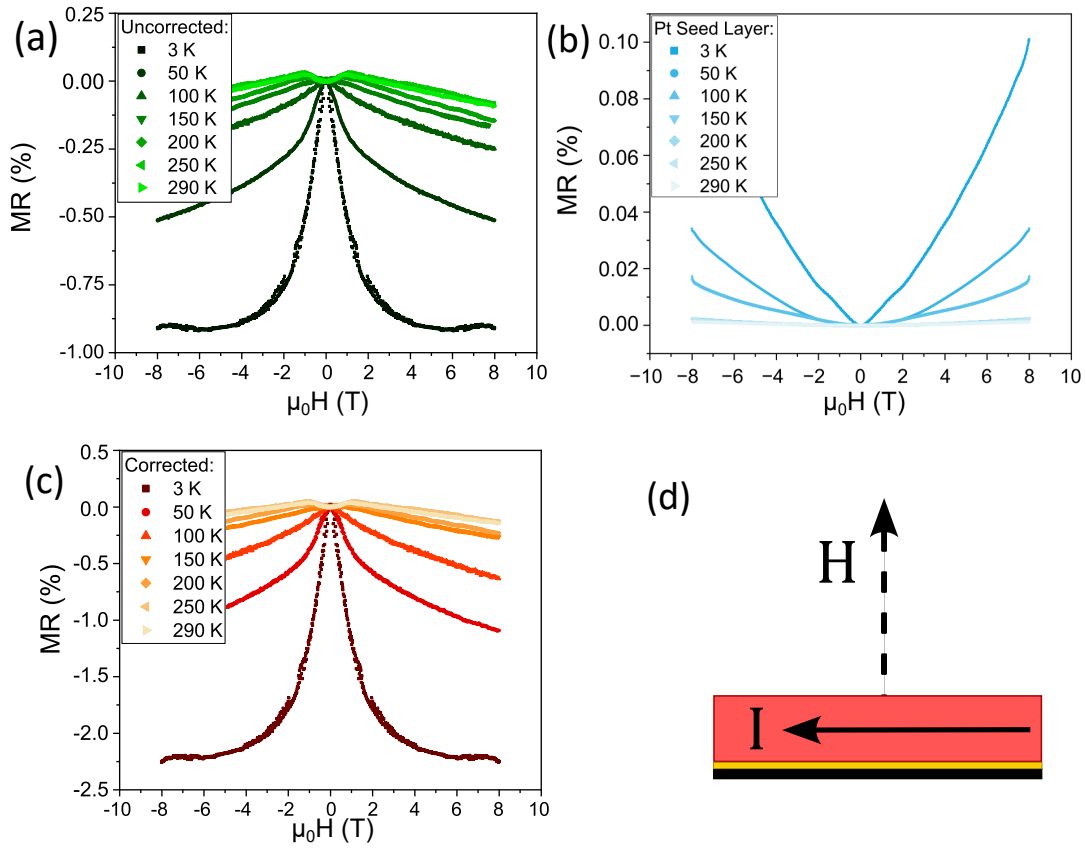

Figure 3.16: MR measurements from (a) the total film, (b) the Pt seed layer individually, (c) the Fe_3Sn_2 layer, calculated from removing the Pt component from the total MR. (d) is a rough schematic showing the magnetic field orientation relative to the current direction.

$$R_{\mathrm{f}}^{\mathrm{xy}} = \frac{R_{\mathrm{T}}^{\mathrm{xy}}}{x^2} - \frac{(1-x)^2}{x^2} R_{\mathrm{s}}^{\mathrm{xy}} \,, \tag{3.14}$$

or, in terms of resistivities:

$$\rho_{\mathrm{f}}^{\mathrm{xy}} = \frac{t_{\mathrm{f}}}{t_{\mathrm{T}}} \frac{\rho_{\mathrm{T}}^{\mathrm{xy}}}{x^2} - \frac{t_{\mathrm{f}}}{t_{\mathrm{s}}} \frac{(1-x)^2}{x^2} \rho_{\mathrm{s}}^{\mathrm{xy}} \,. \tag{3.15}$$

Equations 3.11 and 3.15 together allow for any resistivity data to have its seed layer contribution subtracted from both the longitudinal and the hall resistivity.

3.8.2 The Ordinary and Anomalous Hall Effect

As discussed in section 2.5, a magnetic field will alter the trajectories of electrons in a material producing a transverse voltage known as the Hall effect [29]. By dividing that measured voltage by the supplied current we can calculate the Hall Resistance, and thus also, the Hall resistivity, ρ_{xy}, of the material. According to equation 2.17 we expect the Ordinary Hall Effect (OHE) to be linear in applied field, while the Anomalous Hall Effect (AHE) is linear in *magnetisation*, which will saturate in a high enough field. Since the field is applied perpendicular to the plane of the film, this means the magnetisation will follow the OOP curve in Figure 3.12. In order to extract the coefficient R_{o} and the saturated AHE resistivity, ρ_{AHE}, a straight line is fitted to the high field region greater than $4T$ where the AHE will have completely saturated. Figure 3.17 shows a typical ρ_{xy} measurement for an Fe_3Sn_2 film at 290 K, demonstrating both OHE and AHE with the linear fitted line shown. The gradient of this line is R_o and the intercept is ρ_{AHE}.

3.9 Conclusion

Understanding these experimental techniques puts us in a good position to continue onwards with this thesis. The theoretical background behind scattering, whether it be X-rays or electrons, can be quite involved but is fundamental to the interpretation of measurements that use it. The methodology for the template matching has also been presented in order that the reader may fully understand the logic that has been used to produce the phase maps presented in chapter **??**. The other analysis techniques discussed in this chapter will be applied throughout the rest of the thesis. Specifically the background removal of section 5.2; and the seed layer subtraction of section 3.8.1; should be assumed to have been performed on all hysteresis measurements of chapter 4 and 5 and transport measurements of chapter 6 unless explicitly stated otherwise.

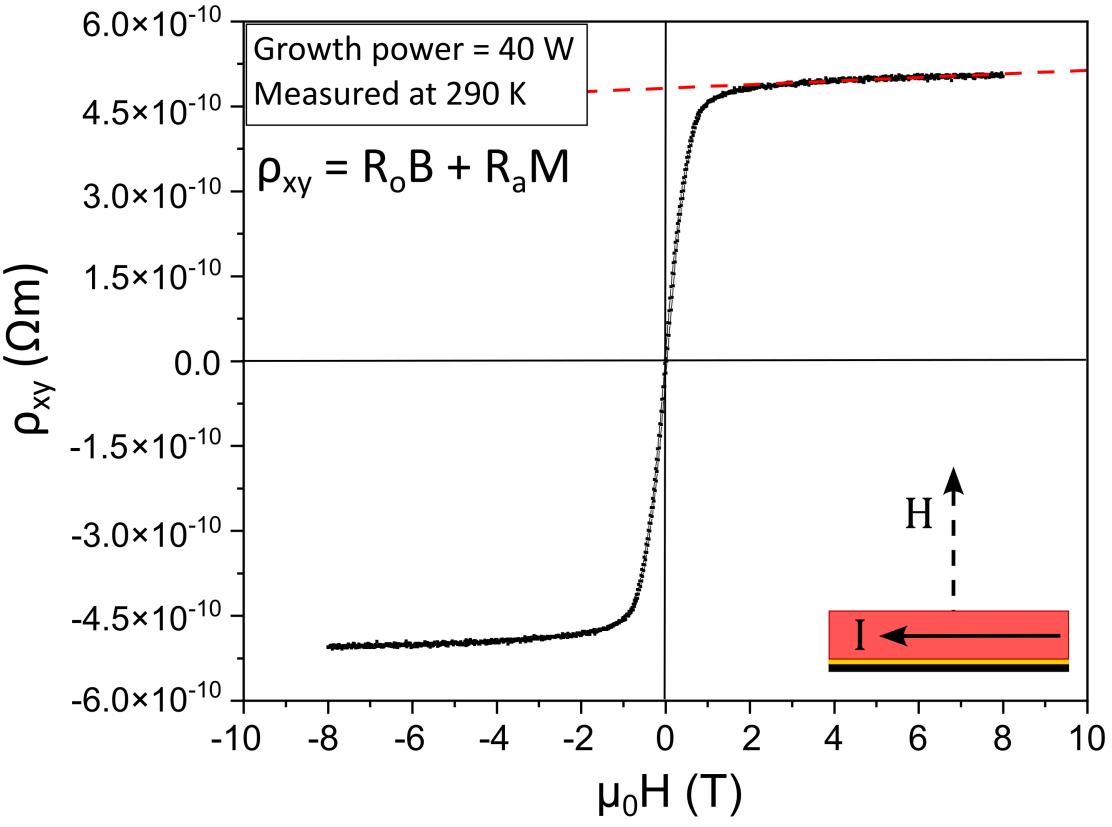

Figure 3.17: Transverse resistivity, ρ_{xy}, measured under a field sweep in the He cryostat. The ordinary Hall effect coefficient, R_{o}, and the saturated AHE resistivity, ρ_{AHE}, are extracted from the gradient and intercept of the linear fitting to the high field region of the measurement, considered to be any flux density greater than 4 T.

Chapter 4

The Growth and Characterisation of Thin Film Fe_3Sn_2

4.1 Introduction

This chapter describes the investigation of phase purity in the deposited Fe_3Sn_2 thin films. As described in Chapter 2, there are five known intermetallic alloys of Fe and Sn; in order of decreasing Fe concentration these are Fe_3Sn, Fe_5Sn_3, Fe_3Sn_2, FeSn and $FeSn_2$. Even when selecting the correct stoichiometry and temperature for the growth, intergrowths of an undesired phase are highly possible. Here we will present the results of three selected films, each grown with a fixed Sn magnetron power of 10 W but a different Fe magnetron power to adjust the stoichiometric ratio present in the deposited film. Each film was grown on a sapphire substrate with a thin Pt seed layer of 3 nm as described in section 3.2.2. The film grown with Fe power of 30 W is 82 $\pm$ 1 nm thick; the one grown with 36 W is 83 nm $\pm$ 1 nm; and the one grown with 40 W is 95 nm $\pm$ 1 nm thick as determined by STEM measurement. The XRD, VSM and S/TEM measurements of these films are shown as well as a discussion of phase purity and crystal quality.

4.2 X-ray Diffraction

Using X-ray diffraction, the lattice spacing present in the grown films can be determined. Fe_3Sn_2 has a repeating structure along the c-axis consisting of a pure Sn layer, followed by two Fe_3Sn layers, then returning to a pure Sn layer. This symmetry results in allowed reflections of (0003) at 13.4°, (0006) at 26.9° and (0009) at 40.9°.

FeSn has its characteristic peaks at 19.9° and 40.5° for (0001) and (0002) respectively. It's important to note that the angular difference between Fe_3Sn_2 (0009) and FeSn (0002) is only 0.4° so this is a poor peak to use in composition characterisation as even some slight strain or peak broadening can blur these peaks into each other.

Figure 4.1 is the XRD pattern for the three films as well as an XRD pattern from a clean substrate on which no film has been deposited for comparison. Looking at the film which has had its growth power tuned to the stoichiometric ratio of FeSn, with Fe growth power of 30 W, two distinctive peaks at 20° and 40° are seen. Present on all XRD data is the c-plane sapphire (Al_2O_3) substrate peak at 41.7° and a broad Pt (111) peak at 40°.

For the XRD pattern from the second film with higher Fe content, this still demonstrates peaks at 20° and 40° but also shows peaks at 13° and 27° which are clear indications of an ordered Fe_3Sn_2 content. Finally, the third sample's XRD pattern shown in Figure 4.1 shows the result of increasing Fe content further. The peaks associated with FeSn subside and only

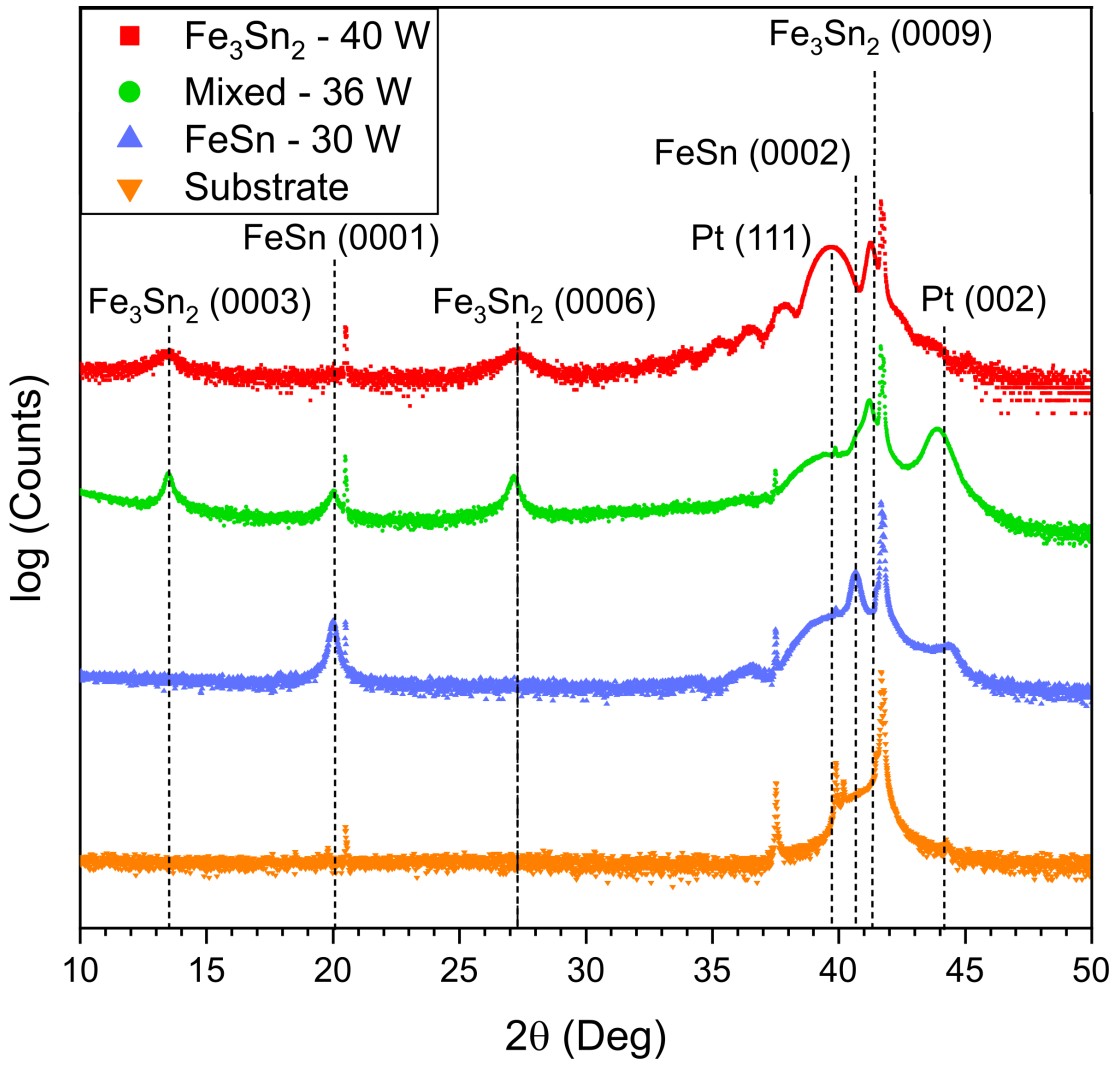

Figure 4.1: $2\theta - \omega$ X-Ray Diffraction (XRD) pattern of three thin films and one clean substrate. Films were grown with different growth power of the Fe gun, 40 W, 36 W, and 30 W. Dotted lines indicate the predicted angles for the labelled reflections. The 30 W sample has FeSn diffraction peaks, the 40 W sample has Fe_3Sn_2 diffraction peaks, and the 36 W sample demonstrates both. It is worth noting that the Pt peak for the 40 W sample is especially well formed, enough to form Pendellösung fringes away from the central diffraction peak at 40°.

those of Fe_3Sn_2 remain. It is worth noting that an XRD peak at about 45° is present on the first two patterns which I associate with growths of the Pt (002) orientation, as this peak's intensity is often inversely proportional to the Pt (111) peak. Based on these XRD patterns, the labelling of "FeSn", "Mixed", and "Fe_3Sn_2" are going to be applied to these films which will be fully justified by the end of the chapter. By fitting a Voigt profile (the convolution of a Gaussian and a Lorentz distribution) to each peak, it is possible to extract the peak parameters which are shown in Table 4.1.

Sample	(h k i l)	x_c (Deg)	FWHM (Deg)	τ (nm)
Fe_3Sn_2	(0 0 0 3)	13.42 ± 0.01	0.98 ± 0.01	8.37 ± 0.09
	(0 0 0 6)	27.24 ± 0.03	1.31 ± 0.04	6.8 ± 0.2
	(0 0 0 9)	41.28 ± 0.03	0.30 ± 0.01	35 ± 1
Mixed	(0 0 0 3)	13.51 ± 0.01	0.31 ± 0.01	26.7 ± 0.9
	(0 0 0 1)	20.02 ± 0.02	0.43 ± 0.07	20 ± 3
	(0 0 0 6)	27.17 ± 0.02	0.39 ± 0.01	22.7 ± 0.6
	(0 0 0 9)	41.22 ± 0.01	0.35 ± 0.01	29.5 ± 0.8
FeSn	(0 0 0 1)	20.01 ± 0.02	0.24 ± 0.01	35 ± 1
	(0 0 0 2)	40.67 ± 0.02	0.31 ± 0.02	34 ± 2

Table 4.1: The peak centre, x_c, Full Width Half Maxima, FWHM, and average crystallite size, τ, for the Fe-Sn peaks in the XRD data in Figure 4.1. x_c and FWHM are extracted from a Voigt fitting to each peak, τ is calculated from the Scherrer equation 3.5.

Using the Scherrer equation, (3.5), we can use the FWHM of these peaks to estimate the average crystallite size for these films. For the FeSn film, an average crystallite size of 34.5 $\pm$ 0.5 nm was found while the Fe_3Sn_2 with its broader (0003) and (0006) peaks had an average crystallite size of 7.8 $\pm$ 0.5 nm. For the mixed film, some slightly more detailed analysis can be performed due to the number of peaks present in the full diffraction pattern corresponding to the Fe_3Sn_2 phase. A method suggested by Williamson and Hall [116] is to assume that the broadening on any peak is just the summation of the broadening due to the finite crystal size and the broadening due to a distribution of microstrains within the crystal. This produces a reasonably simple expression:

$$\beta \cos(\theta) = \frac{K\lambda}{\tau} + 2\epsilon \sin(\theta), \tag{4.1}$$

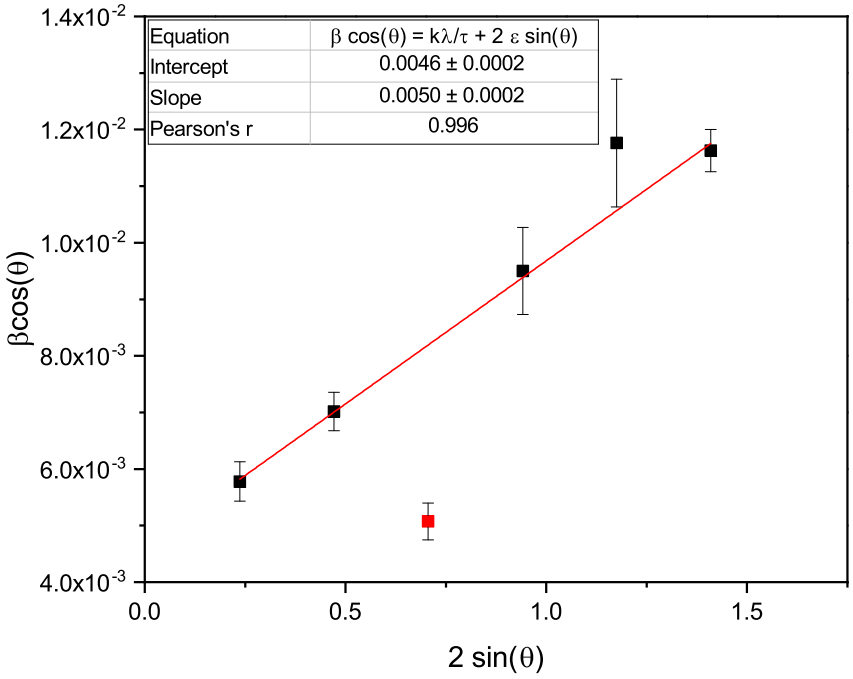

Figure 4.2: Williamson-Hall plot of the Fe_3Sn_2 phase within the mixed film. The red data point, corresponding to the peak at $2\theta = 40°$, has not been included in the fitting due its properties likely being affected by the FeSn peak at the same angle.

where ϵ is the strain (fractional change in lattice constant) of the crystal and all other symbols match their corresponding definitions in the Scherrer equation, (3.5). By plotting $\beta\cos(\theta)$ against $2\sin(\theta)$, shown in Figure 4.2, the result is a straight line whose gradient is the strain and whose intercept can be rearranged to find the average crystallite size. Doing this, we find the crystallite size is 30 $\pm$ 1 nm and the strain is $(5.0 \pm 0.2) \times 10^{-3}$ or 0.50% $\pm$ 0.02%. Unfortunately this analysis is not repeatable on the other films due to there not being any significant diffraction peaks past 2θ = 50°.

It's reasonable to conclude from this data that the phase content for the FeSn and Fe_3Sn_2 films are predominately the desired phase, due to the absence of each other's diffraction peaks in their patterns which is quite evident in the mixed film. However, the crystallite size being smaller than the film thickness, by quite significant amounts in the Fe_3Sn_2 case, would generally indicate that the films are likely polycrystalline.

4.3 Magnetic Response

By taking these three samples and measuring their moment in a SQUID VSM, it is possible to find how the saturation magnetisation varies between the samples. Since Fe is the only magnetic element in the films, one might expect a higher Fe content to always lead to higher magnetisation. However, FeSn is a type-A compensated antiferromagnet [117] so any region of the film in this phase is expected to have no contribution towards the magnetisation.

It is worth noting that Pt can obtain a proximity magnetisation from a neighbouring ferromagnet, but most measurements of this effect predict a relatively thin depth of this effect of about a nanometre and an acquired moment of 0.43 μ_B per Pt atom [118] which in our case would roughly contribute a 4 emu/cm^3 increase to the magnetisation of our films which falls within the error on the measurement and not significant compared to the many hundreds of emu/cm^3 already present from the ferromagnetic films.

In figure 4.3, we see the in-plane magnetisation hysteresis loops for the three samples. The antiferromagnetic FeSn has a saturation magnetisation of 255 $\pm$ 5 emu/cm^3 which is significantly smaller than the mixed phase film with a value of 616 $\pm$ 8 emu/cm^3 which is in turn smaller than the ferromagnetic Fe_3Sn_2 with 835 $\pm$ 9 emu/cm^3. The presence of any magnetic moment in the FeSn sample is likely to be due to the presence of ferromagnetic pure Fe and Fe_3Sn_2 impurities throughout the film. The bulk magnetisation of single crystal Fe_3Sn_2 is reported to be about 700 $\pm$ 100 emu/cm^3 at 4 K by G. Le Caer [23], and also the same at 77 K by B. Malaman [71]. Our value for the saturation magnetisation is higher but is still within

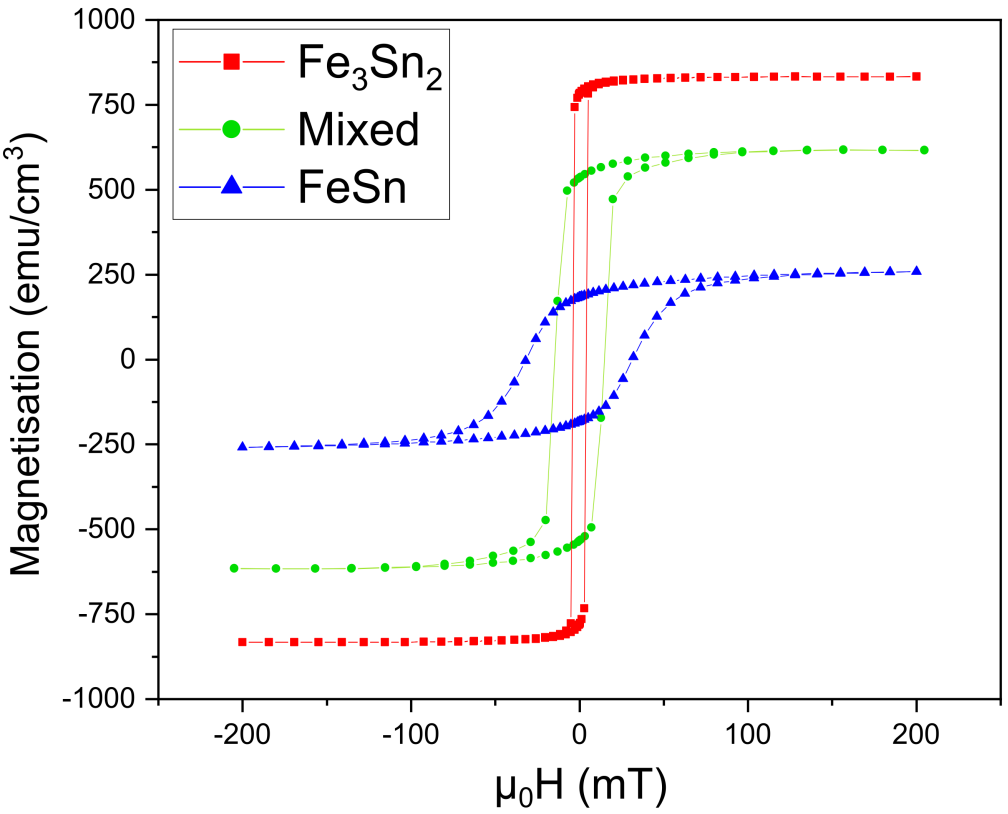

Figure 4.3: In-plane magnetic hysteresis loops for the three films obtained with SQUID-VSM at 300 K. The magnetisation and coercivity of the three films are significantly different.

a reasonable range for a thin film.

The value of the coercivity also changes significantly between the samples. The Fe_3Sn_2 sample has a coercivity, $\mu_0 H_c$, of 4 mT $\pm$ 0.2 mT; the mixed phase film has a coercivity of 31.5 mT $\pm$ 0.5 mT; and the FeSn film has a coercivity of 88.0 mT $\pm$ 0.8 mT. Work by Zhang *et al.* [119] has associated the ferromagnetic to anti-ferromagnetic boundary coupling with an increase in coercivity which could explain why a predominantly FeSn film with some pockets of Fe_3Sn_2 could experience a large coercivity. An interesting feature of the Fe_3Sn_2 film is that despite the small crystallite size calculated in section 4.2, there is not the often associated large coercivity from grain boundaries and defects acting as pinning sites that have to be overcome as the field changes direction.

Further magnetic analysis of these films is the focus of the next chapter.

4.4 Scanning Transmission Electron Microscopy

For further analysis lamellas were cut from all three of these films. All imaging was done on a TESCAN TENSOR with a 1 nA probe current and an electron energy of 100 keV, corresponding to a 2.2 nm spot size and 3.88 pm wavelength. Figure 4.4 is the HAADF real space image of the Fe_3Sn_2 film gathered by the integration process described in subsection 3.4.2. Since this is the Rutherford scattering regime, we expect scattering intensity to go as Z^2 (where Z is the electron number of the scattering atom) and this is exactly what is observed with the Pt of the seed and capping layer being clearly distinguishable as bright bands sandwiching the Fe_3Sn_2 layer. Also note that Al_2O_3, having only light elements, scatters practically nothing to high angles.

For each 3 nm $\times$ 3 nm region in Figure 4.4 it is possible to image an electron spot diffraction pattern; three of which are shown on the right of Figure 4.4 for three sections of the film. The cap of Pt shows the expected polycrystalline rings caused by the blurring of many diffraction spots across a full 2π radians of rotation; the main bulk of the film shows a distinct diffraction pattern whose assignment to FeSn or Fe_3Sn_2 will soon be discussed; and the substrate shows the expected highly ordered set of diffraction spots that we'd expect from a single crystal substrate.

Using EDX we can also gather a more objective view of elemental distribution within the selected region of Figure 4.4 (indicated by the green box) which is shown in Figure 4.5. The five elements chosen for analysis are Fe and Sn for being present in our desired film; Pt for being in the cap and seed layer; and Al and O for being part of the substrate (though oxidation

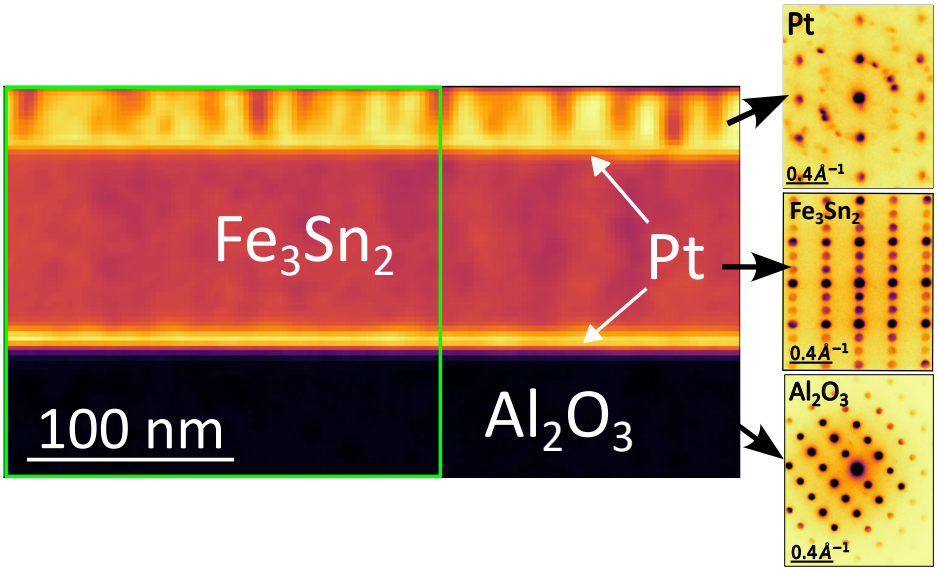

Figure 4.4: HAADF image of a cross section of the 40 W film viewed through STEM microscopy. The Z-contrast between the light sapphire (Al_2O_3) of the substrate and heavy Pt of the seed and capping layer are clear as discussed in section 3.4.2. The green box indicates the region presented for EDX analysis in Figure 4.5. Also shown are the electron spot diffraction pattern from the Pt cap, the main bulk of the Fe_3Sn_2 film, and the sapphire substrate.

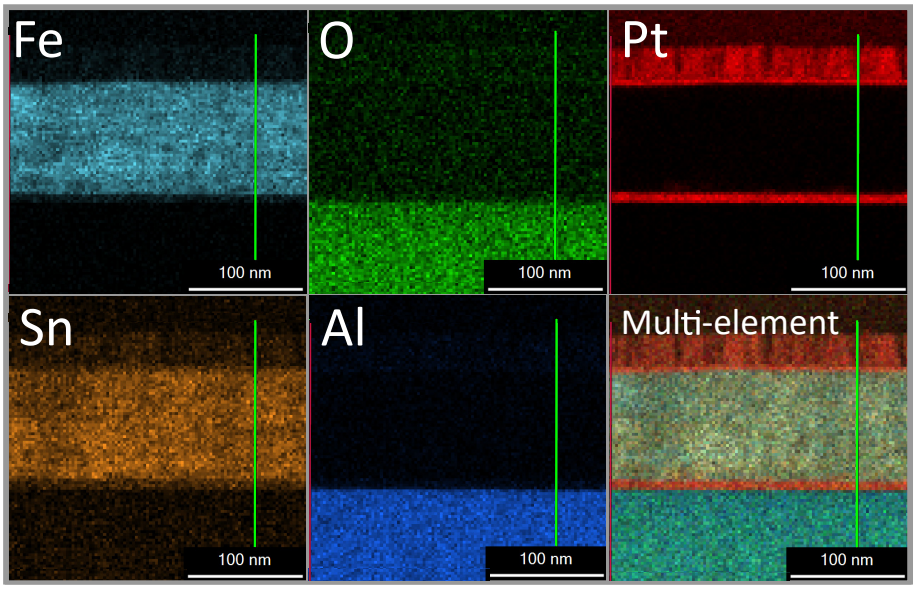

Figure 4.5: EDXS measurement of the cross section in Figure 4.4. Each segment shows the distribution of one of the constituent elements, Fe, O, Pt, Sn, and Al except for the sixth segment which is the combination of the other five. The elemental line profile along the green line is shown in Figure 4.6 for four of these elements.

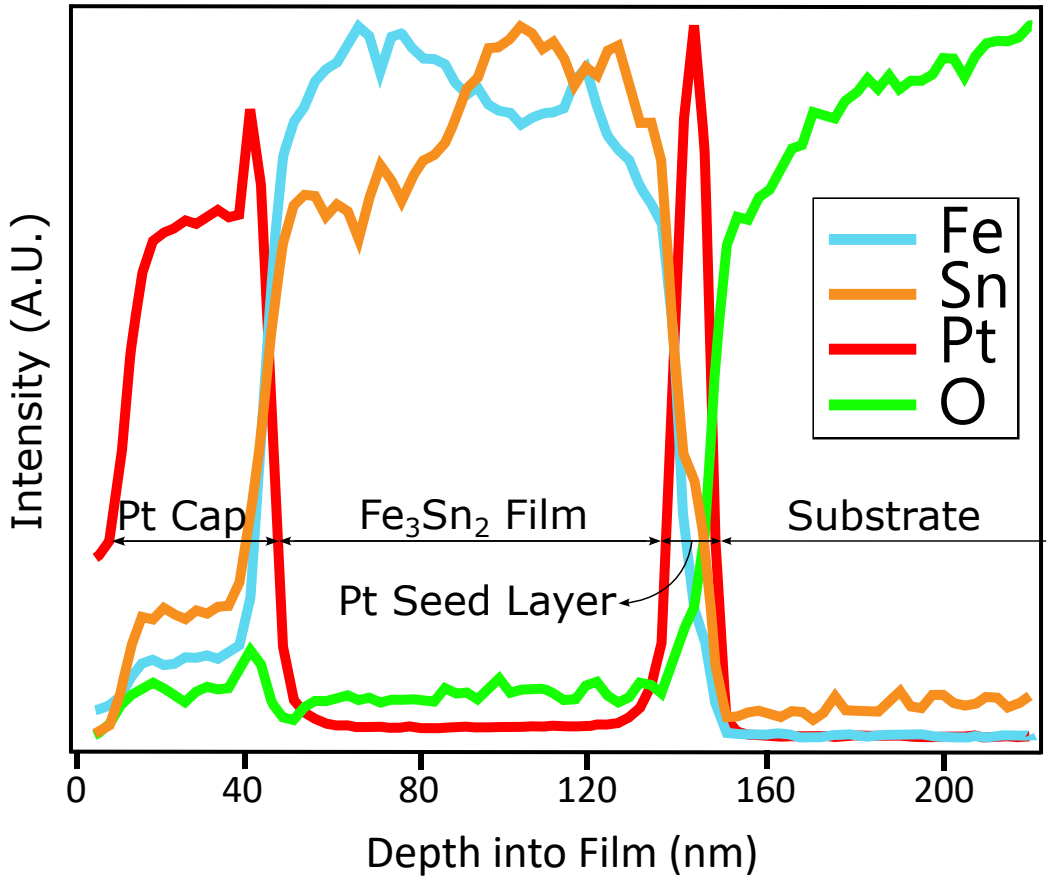

Figure 4.6: Line profiles for Fe, Sn, Pt and O from the EDXS maps in Figure 4.5. The boundaries between layers are well defined with perhaps a few nm of intermixing at either boundary of the Fe_3Sn_2 region. An interesting note is the seemingly increased Sn concentration at greater depths within the film, perhaps indicating a chemical affinity for Pt-Sn alloy.

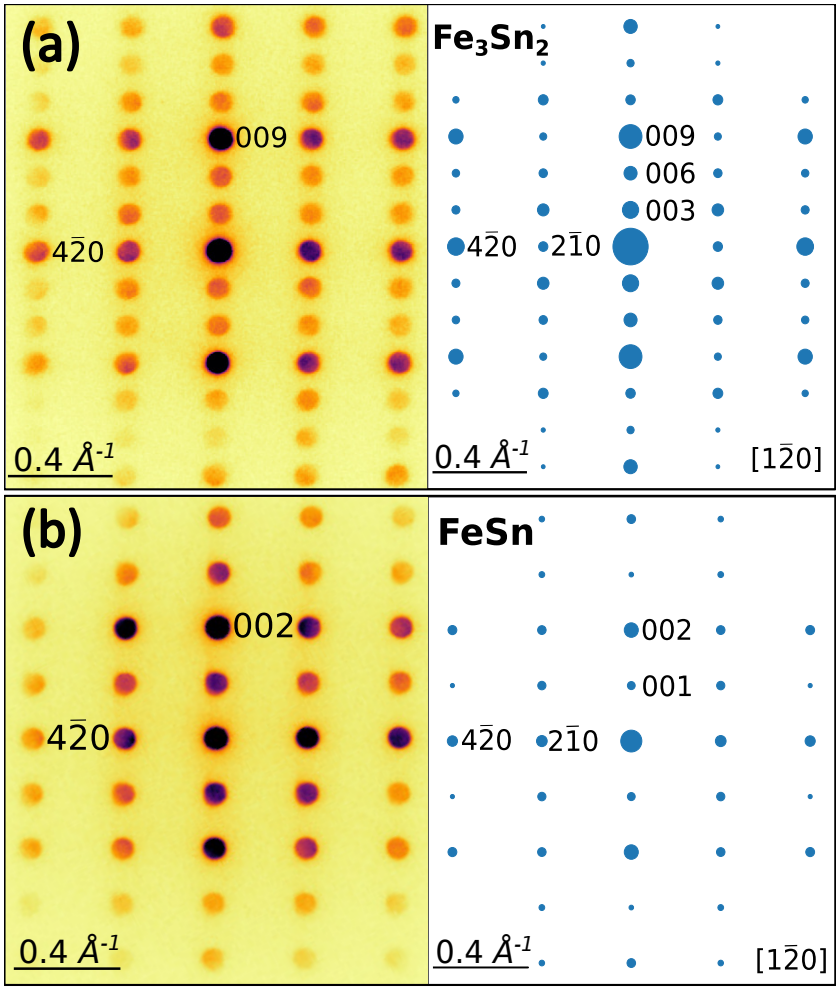

Figure 4.7: PED patterns of (a) Fe_3Sn_2 and (b) FeSn, both gathered from the mixed phase film along with associated simulations for these phases along the $\langle 1\bar{2}0 \rangle$ zone axis with an electron wavelength 3.88 pm. The difference in the stacking sequence between the Fe_3Sn_2 and FeSn films with the ABBA pattern of Fe_3Sn_2 indicated by the pair of dimmer spots between the direct beam and 009, while only a single spot exists in the FeSn pattern.

can of course introduce oxygen throughout the film). A sixth panel combines all the individual elemental maps for ease of view. Generally, all the layers seem well formed, though some consideration should be given to the Sn panel. It's clear from the counts of Sn within the substrate that the EDX spectra for Sn is prone to false positive, but there is also an increased count rate of Sn with the Pt cap layer that doesn't appear in the Fe segment. Figure 4.6 also shows the EDX line profile taken on a line along the c-axis down into the film. Here we can see that indeed there is a significant increase of Sn intensity in the cap (and the corresponding decrease in the upper layers of the film) that perhaps indicates the beginning formation of a Pt-Sn alloy on this upper surface. The line profile does also clearly show that there is a non-negligible intensity of Fe and Sn in the Pt seed layer, though overall the layers are well formed.

Because STEM generates a spot diffraction pattern for every location the electron beam scans over, the resulting 4D-STEM data often contains thousands of individual diffraction patterns. Rather than engaging in the tedious task of assigning these to either the FeSn or Fe_3Sn_2 by eye, it is possible to use a template matching algorithm to compare the data from each pattern to a library of simulated spot diffraction images and return a correlation value for each pair as discussed in section 3.5. In order to perform a phase match, simulations of the potential spot diffraction patterns for the individual phases Fe_3Sn_2 and FeSn need to be produced and verified. Figure 4.7 shows example PED patterns taken from the mixed phase film and matching simulated patterns produced using the Pyxem extension of the Python Hyperspy package. Using the selection of the appropriate wavelength for 100 keV electrons and choosing the zone axis carefully, a strong match between the simulated and observed patterns can be achieved. It was found that a strain from the reported bulk lattice constant in the a-b plane needed to be implemented to improve the match further, with an adjustment from $a = b = 5.344$ Å to a lattice constant that matches with (111) Pt, $a = b = 5.544$ Å. This would correspond to an in-plane strain of approximately 3%.

The results of the template matching process are shown in Figure 4.8. All three films are depicted as a binary colour map where each pixel has either been assigned as Fe_3Sn_2 or FeSn. The results correspond well with the X-ray and magnetisation results with the film suspected of being purely FeSn being assigned only 10.3% of its pixels as Fe_3Sn_2; the mixed film has 67.5% content of Fe_3Sn_2; and the Fe_3Sn_2 as 97.1% Fe_3Sn_2. Also shown are the respective confidence maps for the assignments with bright indicating a relatively high confidence in the phase assignment and dark being a relatively low confidence. It is generally

true that the intergrowths of the undesired phase within the bulk film are associated with drops in confidence of assignment. These areas, depicted in Figure 4.9, often show completely ambiguous PED patterns and so the matching algorithm has to take a low confidence guess as to the phase assignment it selects.

4.5 Transmission Electron Microscopy

Consistent well formed diffraction patterns across a large cross section of a thin film are a good indication of crystalline quality, but these can be hard to present. Something that is even more visually clear is high resolution TEM that allows us to resolve the individual atoms within the atomic layers. Through a collaboration with the University of Glasgow, high resolution TEM images were able to be taken of the 40 W Fe_3Sn_2 film. This is shown in Figure 4.10 for the Fe_3Sn_2 film along with the geometric phase analysis indicating the correct lattice spacings of 6.65 Å are present within the film.

4.6 Discussion and Conclusion

The three methods of X-ray crystallography, magnetometry, and electron microscopy work well in tandem to produce a characterisation of these three films. XRD in particular is a reliable and fast technique to highlight which films are worth examining in closer detail with VSM and STEM measurements. The phase content deduced through the STEM pattern matching has good qualitative agreement with the XRD and good quantitative agreement with the magnetisation of the samples measured through VSM. The ratio of Fe_3Sn_2 content between the Mixed sample and the Fe_3Sn_2 sample extracted from the phase map is 0.70 ± 0.02, while the ratio of their saturation magnetizations is in good agreement at 0.73 ± 0.02. However, the ratio of Fe_3Sn_2 phase content between the FeSn and Fe_3Sn_2 samples is 0.106 ± 0.008 while the ratio of the magnetization is significantly higher with the FeSn film having 0.30 ± 0.03 of the magnetization of the Fe_3Sn_2 sample. I think a reasonable explanation for this comes from the mixed PED patterns of Figure 4.9. Through multiple iterations of coding the template matching algorithm I was generally stricter on what was considered a "good" match to Fe_3Sn_2, adjusting my code until only patterns that were clearly Fe_3Sn_2 were being assigned as such. In a binary assignment, this inevitably means that blurred PED patterns will get assigned more often to FeSn, though these areas do not truly represent fully compensated AFM regions that will provide no additional magnetisation to the sample. A natural extension of this work

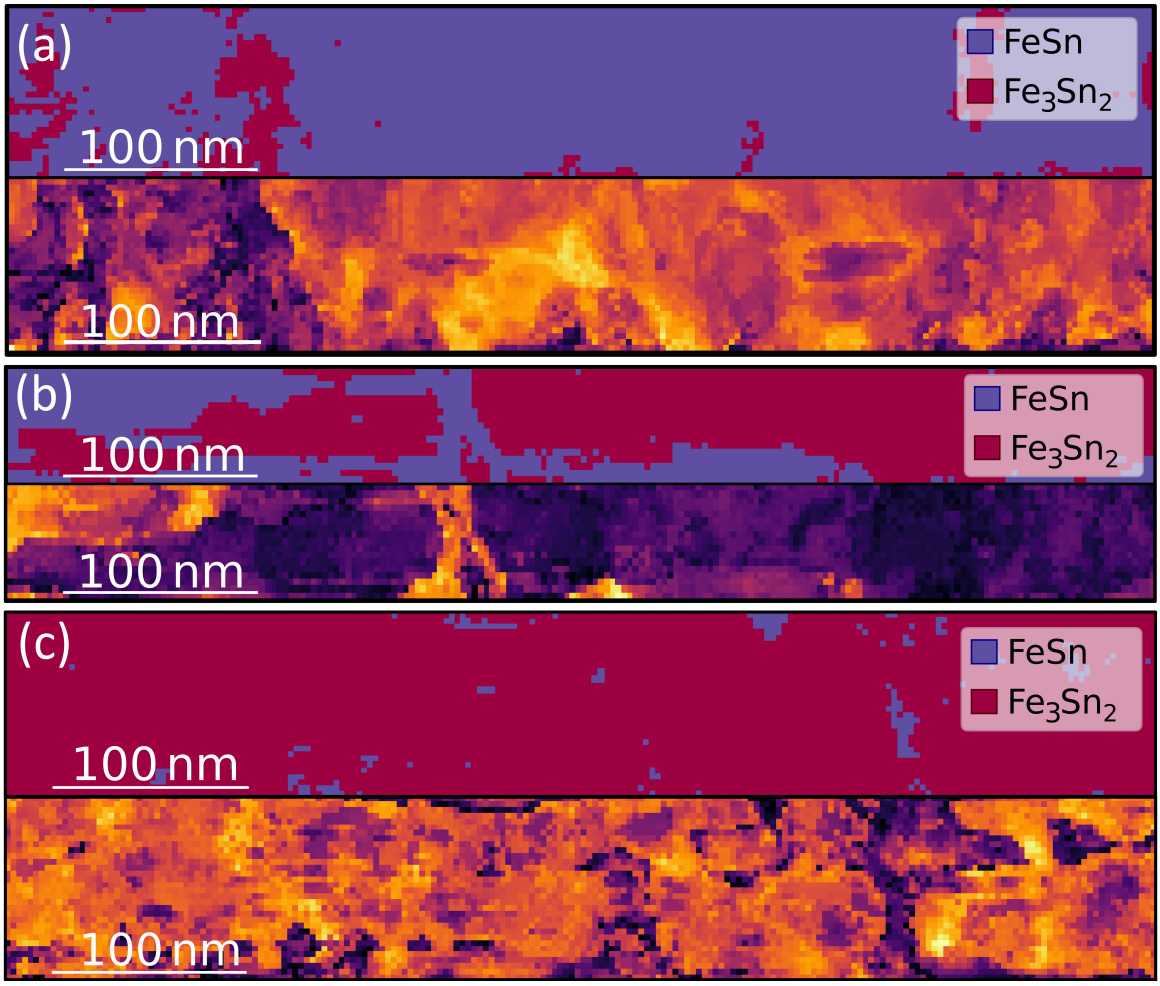

Figure 4.8: Phase maps for cross sections of (a) the FeSn film, (b) the mixed phase film, and (c) the Fe_3Sn_2 film. The percentage Fe_3Sn_2 content by pixel count is 10.3% for (a), 67.5% for (b), and 97.1% for (c). Also shown underneath is the associated confidence map for each phase assignment (see equation (3.7)), bright and dark representing high and low confidence respectively. Note that the intergrowth areas between phases are often associated with a reduced confidence value due to these pixels often blurring the distinct PED patterns over each other, as shown in Figure 4.9.

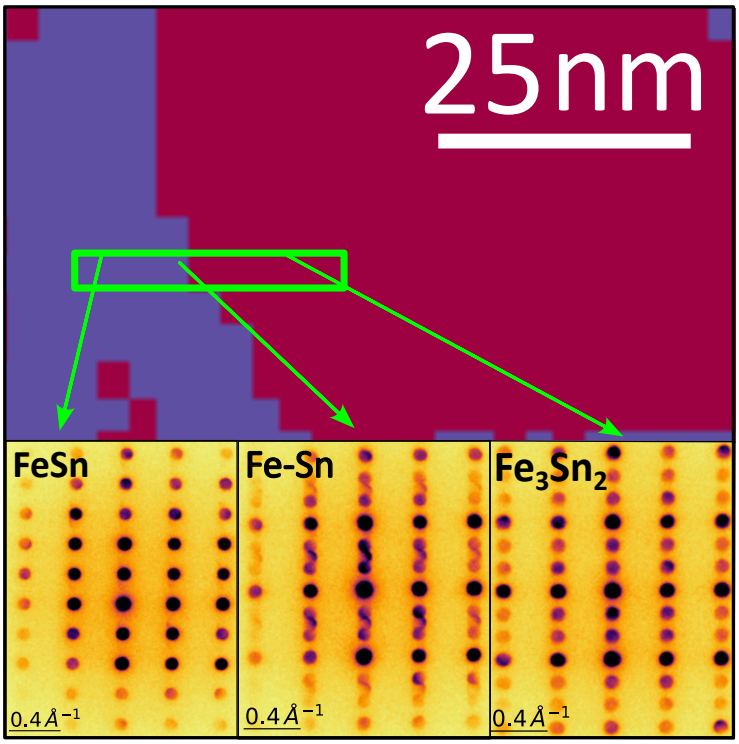

Figure 4.9: Zoomed in phase map of the mixed phase film shown in Figure 4.8. The PED patterns for the highlighted areas are shown, with the boundary region being a clear combination of the diffraction patterns on either side.

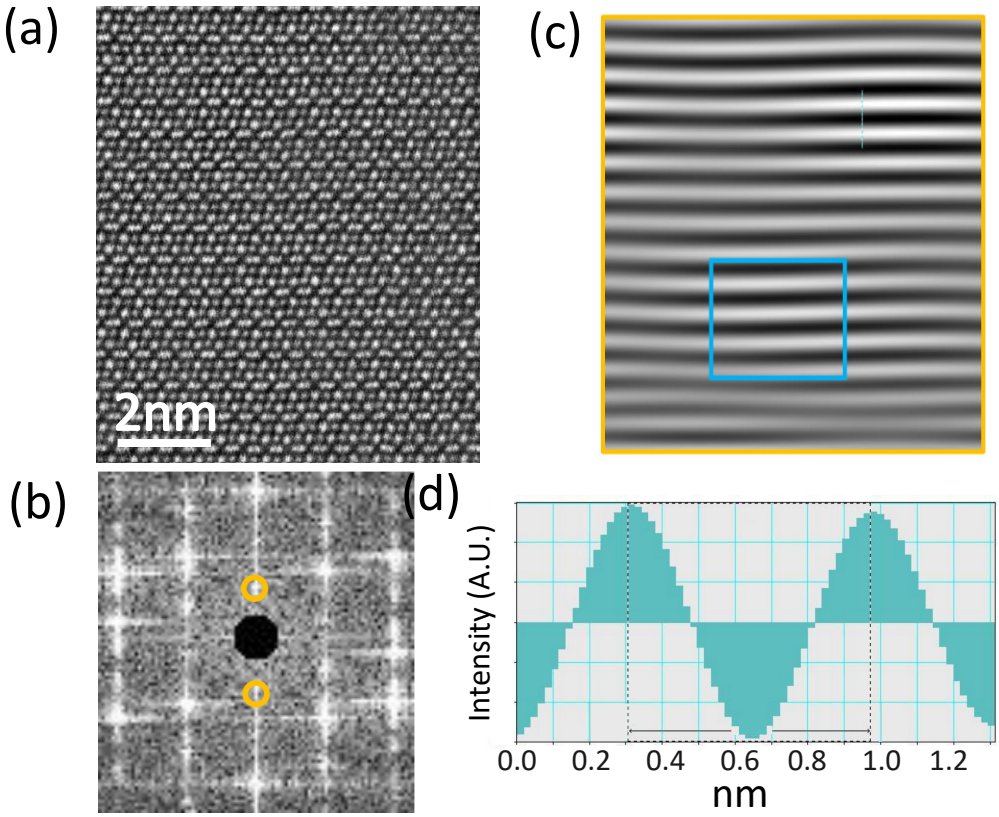

Figure 4.10: In (a) we see the high resolution STEM image of the Fe_3Sn_2 film showing the well formed crystal layers. The fast Fourier transform (FFT) of the image in (a) is shown in (b). In (c) the inverse Fourier transform has been performed around the highlighted spots in (b) which reveals spatial frequencies associated with these spots that correspond to the crystal layers. The separation between these can then be easily measured as 6.6 ± 0.1 Å as shown in (d).

would be to produce new template libraries that contain the blurred PEDs and assign these as a third phase in the phase map. Another less sophisticated option would be to assign a mixed phase designation to any region of the film that has a confidence value in its Fe_3Sn_2 or FeSn assignment below some cut-off value.

Overall, it has been shown that by controlling the stoichiometric ratio, the phase content of Fe-Sn thin films can be controlled to a reasonably high degree of accuracy.

Chapter 5

The Magnetic Properties of Fe_xSn_{1-x} Thin Films

5.1 Introduction

In the previous chapter, the crystallographic characterisation of three thin films was performed, with the conclusion being that the phase content of one film was 97.1% Fe_3Sn_2; one was 67.5% Fe_3Sn_2 and 32.5% FeSn; and the final one was 89.7% FeSn. Before the experiments of the previous chapter were performed, these samples were cleaved in two and the half that did not undergo any electron microscopy were studied for the results of this chapter. Since we are now confident in the composition of these films, they will be referred to and labelled as "Fe_3Sn_2", "Mixed", and "FeSn" for the remainder of this chapter.

All three films were studied through the magnetometry methods discussed in section 3.6. In order to fit in the SQUID magnetometer a further dissection was needed, that cut the films down into the 4 mm by 4 mm size required to fit in the magnetometer.

5.2 Hysteresis Loops

Hysteresis loops, as discussed in section 2.2.2 and section 3.6, are the principal way of gathering information about the magnetic content of a material. By mounting the samples with the applied field direction both In-Plane (IP) and Out-Of-Plane (OOP) it is possible to measure the magnetic moment vs. field along both the easy and hard axis of the material. Due to the strong shape anisotropy of a thin film, this easy plane always lay in the IP direction.

Figure 5.1 shows the hysteresis loops for the Fe_3Sn_2 film over a range of temperatures. The hysteresis curves for the Mixed film are shown in Figure 5.2 and the FeSn film Figure 5.3. All three films are shown to have their easy axis in-plane. The saturation field, $\mu_0 H_s$, required to saturate the magnetisation out-of-plane was found to be 1010 ± 30 mT for the Fe_3Sn_2 film; 780 ± 40 mT for the Mixed film and 200 ± 60 mT for the FeSn film. In each of Figure 5.1, 5.2, 5.3, the magnetic field axis has been scaled in order that the switching of the magnetisation is visible. The inset in (a) in each of these figures shows the full loops taken out to saturation.

Since a perfect OOP mounting is impossible, there will always be some contribution from the easy axis pointed along the field direction. This is most noticeable in Figure 5.1 (b), in which some small switching is observed around zero field. In each case, the inset in (b) shows the region around zero field so that this behaviour can be examined.

At higher temperatures, the increased thermal energy allows more of the individual magnetic moments to reverse direction at any given moment in time, which in turn reduces the saturation magnetisation (or equivalently, a higher temperature will lead to higher magnon

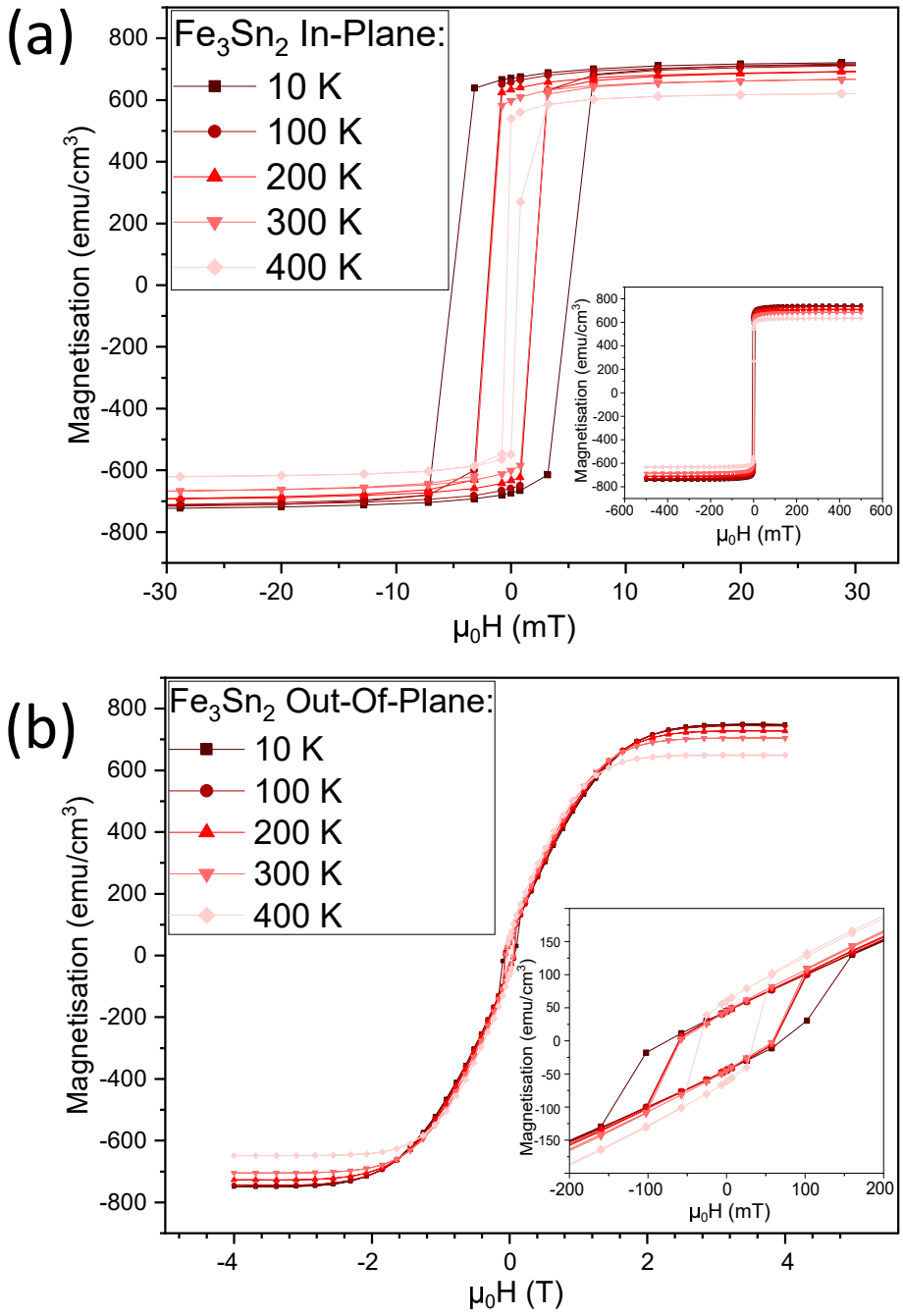

Figure 5.1: IP (a) and OOP (b) hysteresis loops for the Fe_3Sn_2 film across a range of temperatures. The inset in (a) shows the curves to full saturation. The inset in (b) shows an expanded region around 0 field.

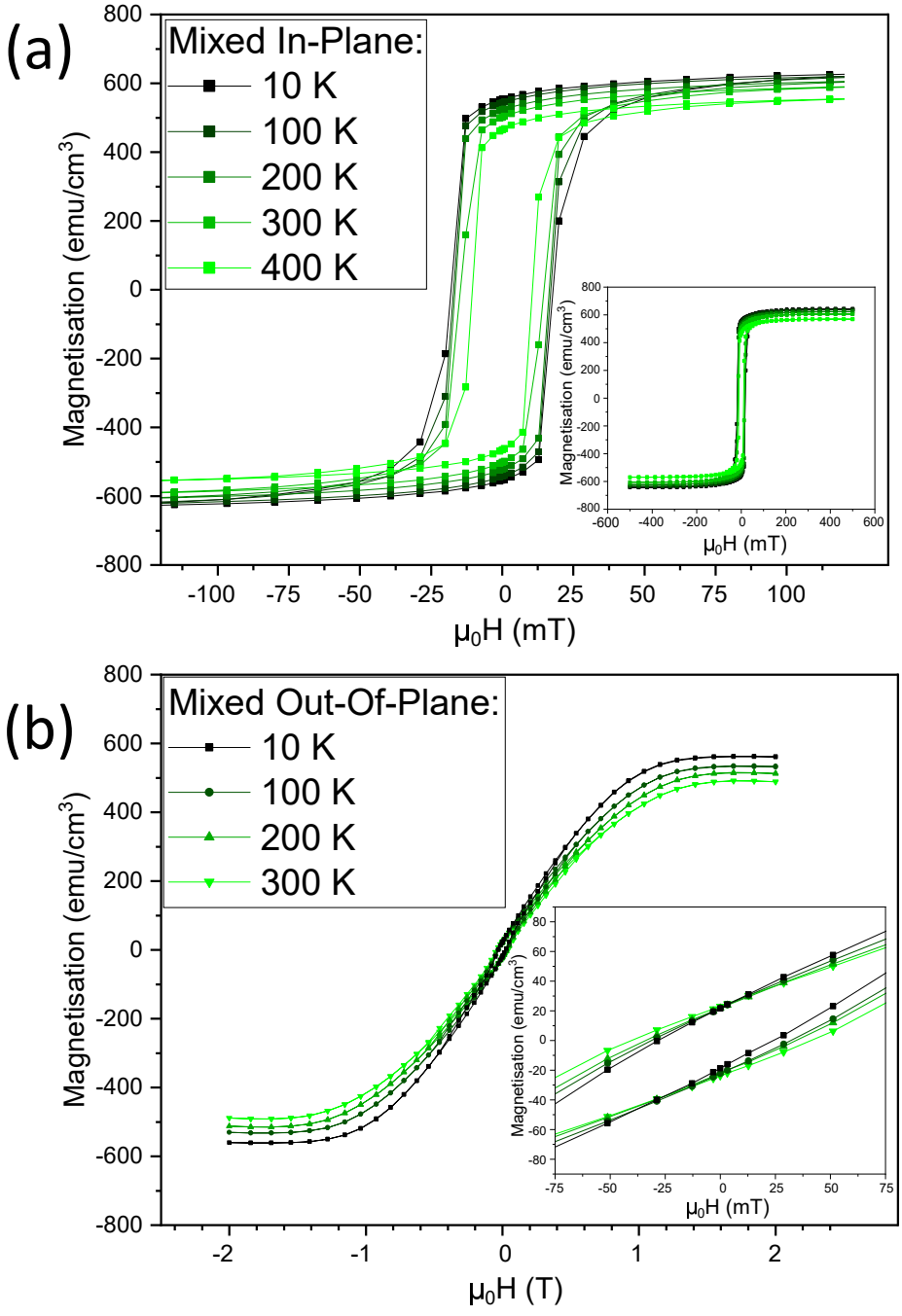

Figure 5.2: IP (a) and OOP (b) hysteresis loops for the Mixed film across a range of temperatures. The inset in (a) shows the curves to full saturation. The inset in (b) shows an expanded region around 0 field.

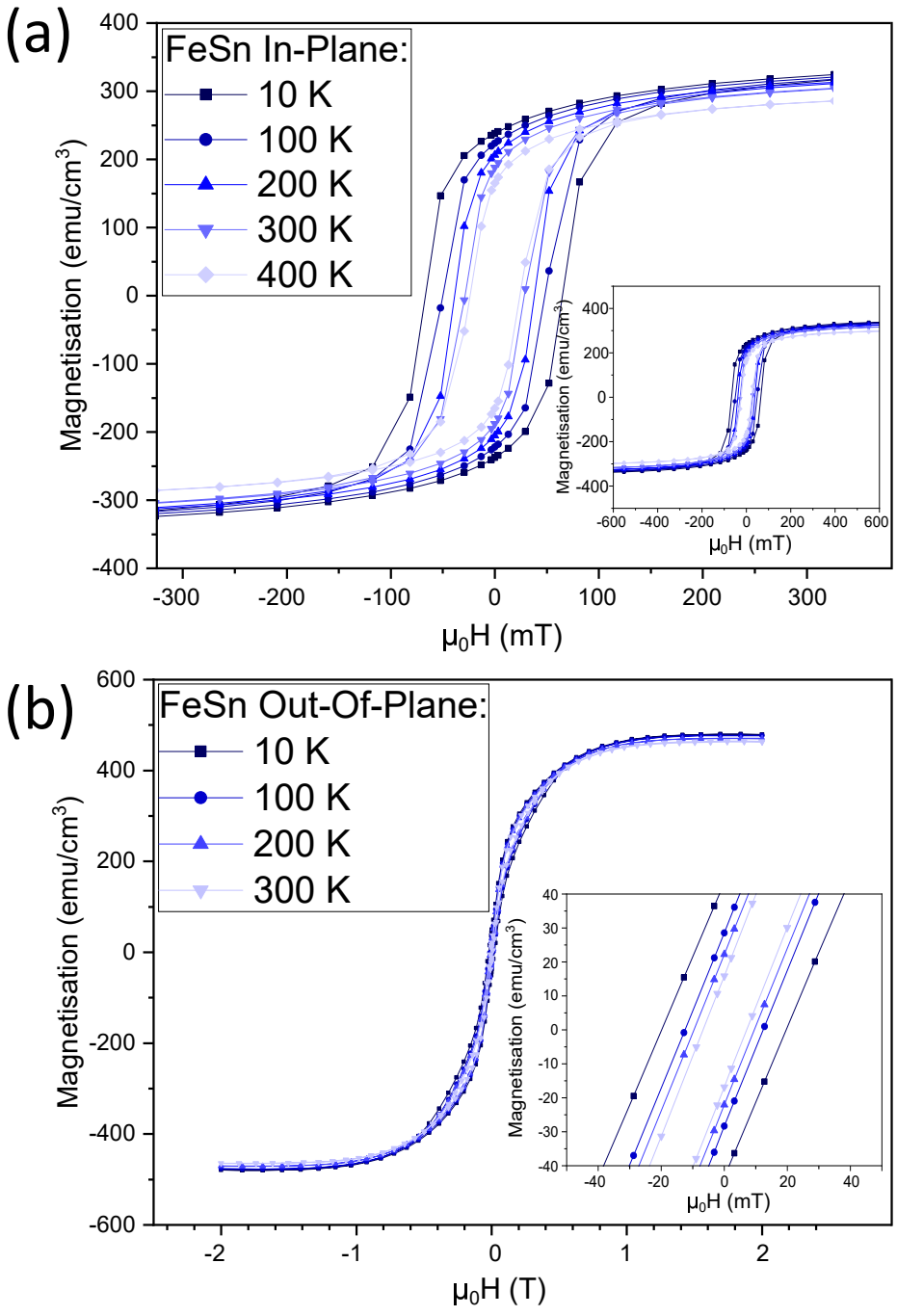

Figure 5.3: IP (a) and OOP (b) hysteresis loops for the FeSn film across a range of temperatures. The inset in (a) shows the curves to full saturation. The inset in (b) shows an expanded region around 0 field.

density where each magnon reduces the total saturation magnetisation by one $\hbar$). Since the ferromagnetic content of each film is provided completely by the Fe_3Sn_2 content (the FeSn, being an antiferromagnet, should have no net magnetisation) it is then reasonable to predict that the temperature dependence of the saturation magnetisation, M_s, should actually be shared across all three films. Figure 5.4 shows the saturation magnetisation vs. temperature curves for all three films. None of the films were taken to the Curie point, T_c (where the saturation magnetisation would fall to zero), due to the effect of high temperature on the structure of the films which is discussed at the end of this chapter, however, a rough extrapolation by eye allows us to estimate that T_c will occur somewhere in the region beyond 800 K for all three films. Figure 5.4 (d) shows the magnetisation normalised to the 10 K value (where available) for comparison. It is clear that the qualitative behaviour of the magnetisation is shared by all three films, as expected if the primary contribution to the magnetisation is arising from the Fe_3Sn_2 content.

Figure 5.5 shows the data for saturation magnetisation vs temperature for the three films in the 10 K to 175 K region which has been fitted with the Bloch-$\frac{3}{2}$ law, as discussed in section 2.2.3. This region has been selected as it is sufficiently below the T_c of Fe_3Sn_2 ($175\,\mathrm{K} \approx \frac{T_c}{4}$) and so magnon-magnon interactions are unlikely to be contributing significantly to the reduction in magnetisation. From these fittings the zero temperature magnetisation M_0 as well as the parameter b that can be used to calculate the spin-wave stiffness D can be extracted. The results for these are shown in Table 5.1 along with the associated uncertainties. Generally the Bloch-$\frac{3}{2}$ law fit well for all three films, with reduced χ^2 values of 1.28, 0.539 and 2.63 for the Fe_3Sn_2, Mixed and FeSn film respectively. For the combined fit, the difference between the $a = 1.5$ and the free varying a fits were minimal, however the uncertainty introduced into b (leading to a result of $b = (3 \pm 4) \times 10^{-6}$) is highly undesirable, as well as the fact that without a model to explain this varying coefficient, extracting physically relevant parameters becomes difficult to impossible.

It is worth briefly mentioning the thin film correction that can be applied to Bloch's law to account for the fact that in a thin film magnons will end up being quantised (as opposed to plane waves) along the normal direction of the film [120, 121]. Following the work of L. Huang *et al.* [122] the adjusted Bloch-$\frac{3}{2}$ law is:

$$M_S(T) = M_0 + \frac{\gamma\hbar}{4\pi L_z}\frac{k_B T}{D}\sum_{m=0}^{(L_z/a)-1} \ln[1 - e^{\frac{\omega_m}{k_B T}}]\,, \tag{5.1}$$

with

$$\omega_m = \gamma\hbar B_z - D\left(\frac{m\pi}{L_z - a}\right)^2 , \tag{5.2}$$

where $\gamma = 1.7\times10^{11}$ $\mathrm{T^{-1}s^{-1}}$ is the gyromagnetic ratio [123], L_z is the film thickness, $a = 0.22$ nm is the separation between atomic layers, and D is the exchange stiffness at $T = 0$ K.

When the summation in equation 5.1 contains more than a few dozen terms it rapidly approaches the original Bloch-$\frac{3}{2}$ law and so when a fit with this model was performed, the extracted values differed from those in Table 5.1 by only 0.1% at a maximum (and for most parameters significantly less than that). However, this fitting, performed using the DREAM Markov chain Monte Carlo algorithm as implemented in the Bumps package [124], also allows correlation values between the parameters to be extracted, which are presented in the Appendix C.

Sample	a	M_s (emu/cm^3)	b (K^{-1})	D (J/m^2)
Fe_3Sn_2	**1.5**	776.6 ± 0.6	$(8.6 \pm 0.6) \times 10^{-6}$	$(4.1 \pm 0.2) \times 10^{-40}$
Mixed	**1.5**	645.7 ± 0.3	$(11.5 \pm 0.3) \times 10^{-6}$	$(3.51 \pm 0.08) \times 10^{-40}$
FeSn	**1.5**	323.9 ± 0.2	$(10.0 \pm 0.4) \times 10^{-6}$	$(6.16 \pm 0.06) \times 10^{-40}$
Combined	**1.5**	**1**	$(10.0 \pm 0.5) \times 10^{-6}$	–
Combined	1.7 ± 0.2	**1**	$(3 \pm 4) \times 10^{-6}$	–

Table 5.1: The fitted parameters for the three films and associated uncertainties. Values in bold were fixed parameters during the fitting.

Due to the work of section 4.4 in the previous chapter, we know the Fe_3Sn_2 content of these films (97.1%, 67.5% and 10.3%). If we assume that the remaining content is entirely FeSn, with no contribution towards the magnetisation, then we arrive at a discrepancy as the M_s values presented in the table indicate that the Mixed film has 0.73 ± 0.02 and the FeSn film has 0.30 ± 0.03 of the magnetisation of the Fe_3Sn_2 film. As a reminder, the bulk saturation from the literature for Fe_3Sn_2 was found to be 700 ± 100 emu/cm^3 [23, 62] which forms a strong agreement with our pure Fe_3Sn_2 film. We would generally associate this with the binary phase mapping having been set to assume an FeSn structure when the confidence value of a pattern matching is low, which is discussed in more detail in section 4.6.

The spin-wave stiffness in the Fe_3Sn_2 film is reasonably close to that reported in the literature by Dally *et al.* [34] which was 3.70×10^{-40} J/m^2. It is worth noting that this literature result was calculated through high temperature measurements that was then extrapolated

backwards to predict the 0 T value, and so the work presented here should be seen as validating that method. In the Mixed film, a reduction in spin wave stiffness is expected as the presence of disordered boundaries between the Fe_3Sn_2 and FeSn regions would mean that the overall average interatomic exchange interaction has been reduced. Slightly harder to explain is the increase again as the FeSn phase becomes dominant. A working hypothesis is that this is a result of the ferromagnetic Fe_3Sn layers that exist within both the Fe_3Sn_2 and FeSn structures. Since we are measuring the net magnetisation, we know that there are uncompensated moments from these layers present. These layers may still be crystallographically well formed, even if the stacking is not quite perfect enough to produce the full antiferromagnetic effect. This is corroborated by the XRD patterns of section 4.2 which shows that the FeSn film has the highest intensity and narrowest FWHM on its diffraction peaks, likewise indicating good crystallographic structure.

5.3 Coercivity

As well as the magnetisation vs. temperature, it is also possible to extract the coercivity vs. temperature for the three films as shown in Figure 5.6. Here, the behaviour of the three samples is markedly different. The Fe_3Sn_2 film has an initial high coercivity at low temperature that rapidly drops at above 50 K to an almost constant 1.5 mT for the rest of the temperature range. The FeSn film has a more gradual reduction in coercivity which eventually forms a low plateau beginning at 400 K. The Mixed sample has by far the most drastic behaviour, with an initial drop of coercivity that forms a minimum at about 375 K, before beginning to rise again. The initial assumption was that a crystallographic change was occurring in the film due to the high temperature, but repeated measurements of the same sample found that the low temperature behaviour remained unchanged and the minima in coercivity could be reproduced on multiple temperature sweeps. Currently this behaviour is not understood, with the potential cause being some kind of interaction occurring at the ferromagnetic-antiferromagnetic boundary regions within the Mixed phase film.

For both the Fe_3Sn_2 and FeSn film, there was no discontinuity in coercivity when switching from the regular SQUID measuring stick to the oven stick, however a discontinuity did arise for the Mixed sample. As a result, the regular mode measurements for the Mixed sample had to be performed on the oven stick which limited the minimum temperature that could be achieved to 150 K.

Since coercivity is the field required to induce reversal in the magnetisation direction, the

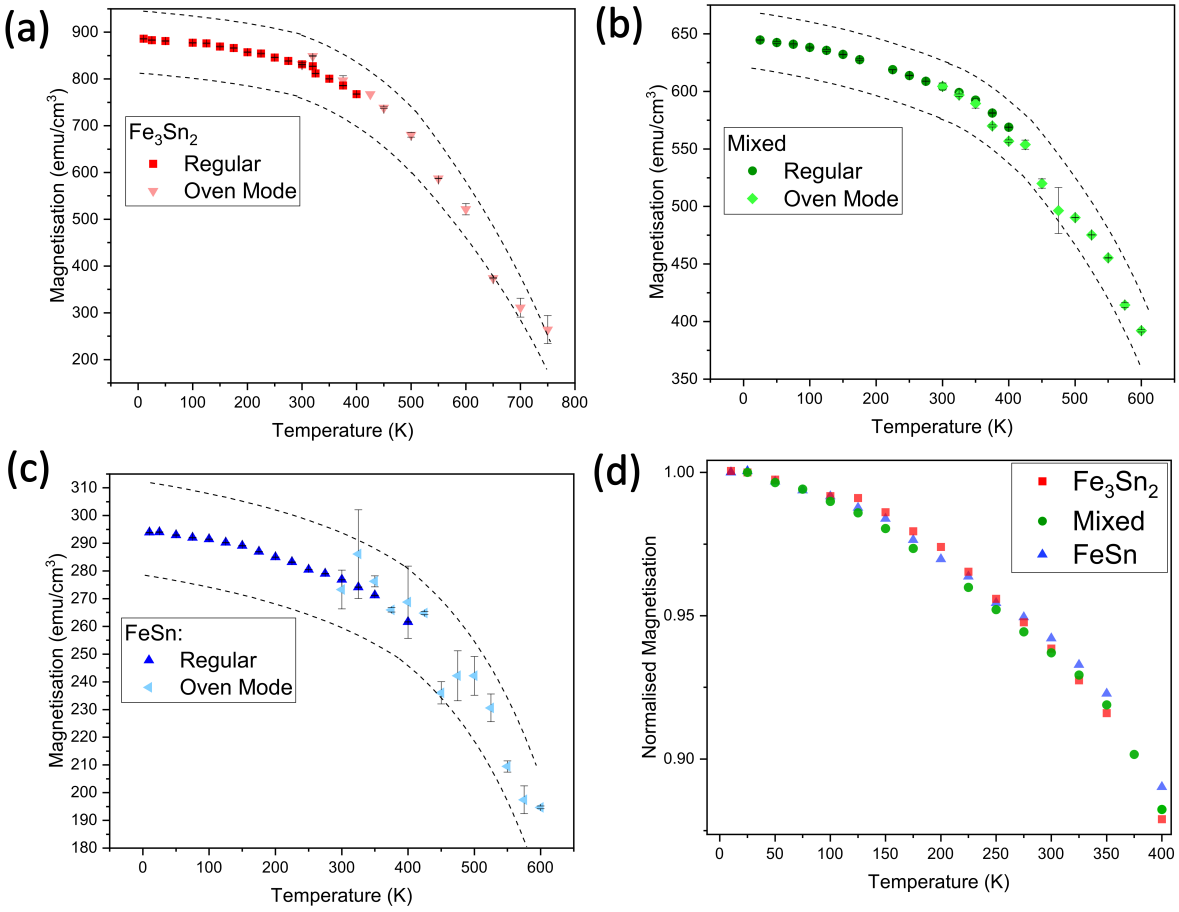

Figure 5.4: Saturation magnetisation vs temperature curves for (a) Fe_3Sn_2, (b) Mixed, and (c) FeSn films. The measurements taken with the SQUID magnetometer in regular and oven mode are indicated. Error bars indicate individual uncertainties associated with measuring a particular saturation moment from the hysteresis loop. The dotted lines indicate the systematic uncertainty introduced by dividing the moments by the volumes of the films.

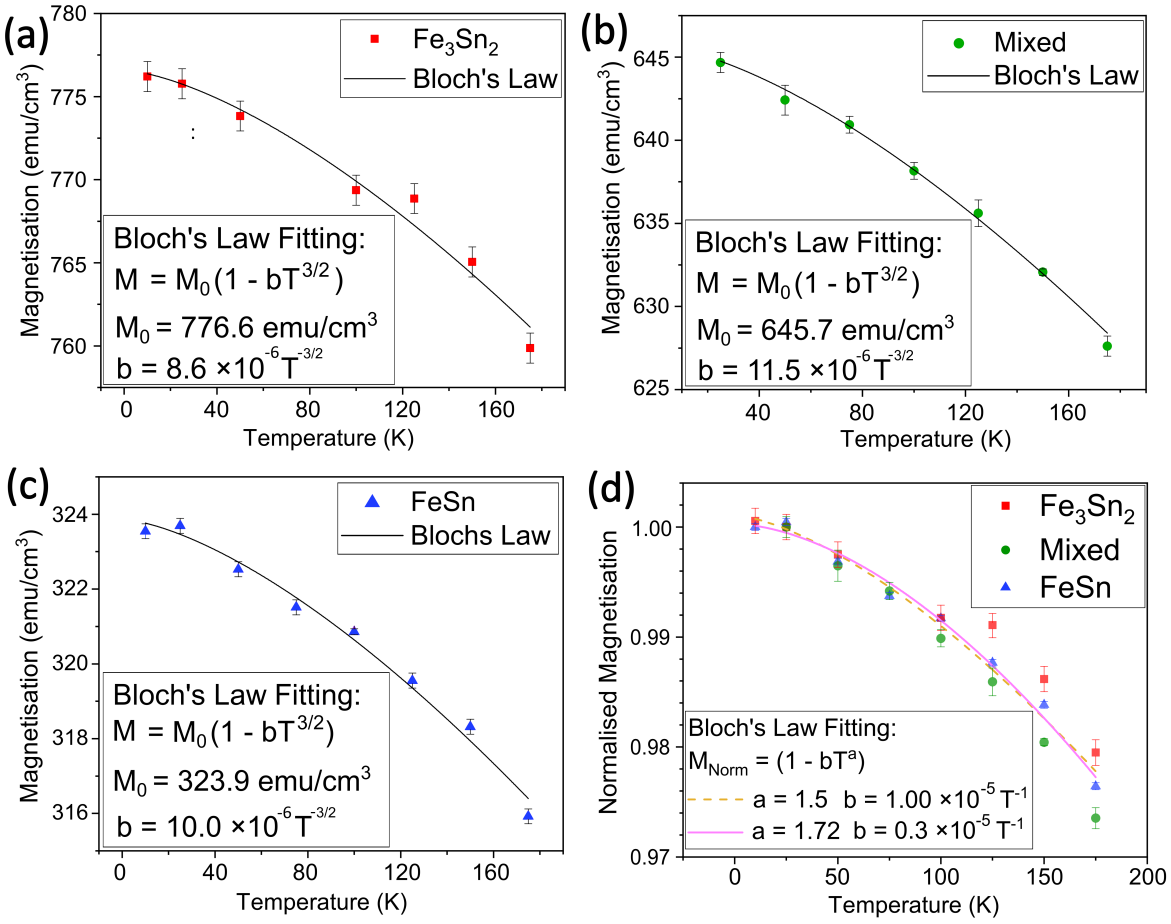

Figure 5.5: Saturation magnetisation vs. temperature curves for (a) Fe_3Sn_2, (b) Mixed, and (c) FeSn films in the region 10 to 175 K. Error bars indicate individual uncertainties associated with measuring a particular saturation moment from the hysteresis loop. In (d) the three data sets are normalised for comparison. Fitting according to the Bloch-$\frac{3}{2}$ law has been performed with the fitting parameters presented in Table 5.1. For the normalised magnetisation vs. temperature in (d), both a $\frac{3}{2}$ exponent and a free exponent has been fit to the combined dataset for comparison.

sudden drop in the Fe_3Sn_2 film's coercivity and the subsequent steady value past 75 K implies a distinct magnetic change occurred within this film. This should be compared to the much more gradual reduction in coercivity seen in the FeSn film in Figure 5.6 (c), which follows Kneller's law for magnetic nanoparticles [125] which would be expected as the FeSn film is likely composed of regions of ferromagnetic Fe_3Sn_2 whose coercivity is being measured. Due to the reported frustrated state of bulk Fe_3Sn_2 a likely explanation for the Fe_3Sn_2 thin film is that this transition is caused by a low temperature spin-glass state, in which all the spins have been "frozen" into a random distribution of misalignment by rapidly cooling, which is then "melted" back to a ferro/paramagnet by the application of temperature. After being energetically freed from the spin-glass, the moments can then reorientate freely and the coercivity drops to its relatively low value.

Figure 5.6 (d) shows a comparison between all three films, as well as the full temperature range for the Mixed film, with the inset showing the normalised values for all three films. This comparison indicates just how large the scale for the change in coercivity in the FeSn film is. The temperature at which coercivity stops changing ranges from 75 K for the Fe_3Sn_2 film to 400 K in the FeSn film.

Figure 5.7 shows an attempt to confirm the presence of a spin glass transition through the measuring of the AC susceptibility for the Fe_3Sn_2 film. Unfortunately, the strong presence of a peak at 40 K (which we associate with the oxygen content of the sapphire substrate, Al_2O_3 [126]) means that observation of a susceptibility change during a spin-glass transition at low temperature was not possible. No other notable features were observed at higher temperatures, except for a general increase in susceptibility. Future work that could reproduce thin films on a different substrate would not have this limitation.

5.4 Magnetocrystalline Anisotropy and Spin Reorientation

By integrating the area between IP and OOP hysteresis curves, as discussed in section 3.6, it is possible to extract the effective anisotropy, K_{eff} as a function of temperature. This anisotropy has two main components, the shape anisotropy, $K_{\text{s}} = \frac{1}{2}\mu_0 M_{\text{s}}^2$, which is caused by the geometry of the thin film, as well as the magnetocrystalline anisotropy, K_{mc}, that arises from the fundamental anisotropy of the crystal structure.

The relationship between magnetocrystalline anisotropy and magnetisation is often phenomenologically associated with a power law, with the exact coefficient varying heavily based on crystal structure and which orbitals are contributing [127, 128]. Figure 5.8 shows the

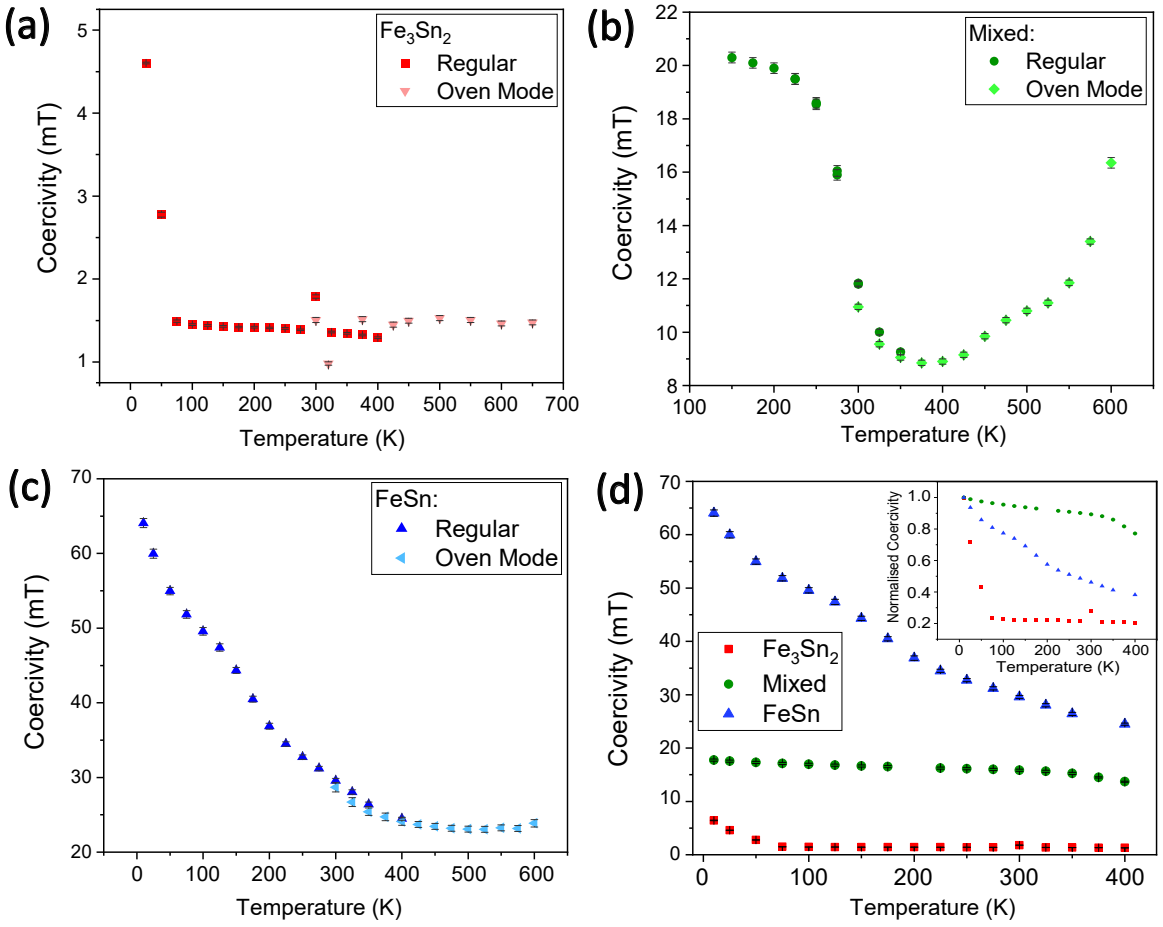

Figure 5.6: Coercivity vs. temperature curves for (a) Fe_3Sn_2, (b) Mixed, and (c) FeSn films. The measurements taken with the SQUID magnetometer in regular and oven mode are indicated. Error bars indicate individual uncertainties associated with measuring a particular coercive field from the hysteresis loop. The comparison between the coercivities taken in regular mode is shown in (d) with the inset showing the shape of the normalised coercivity curves.

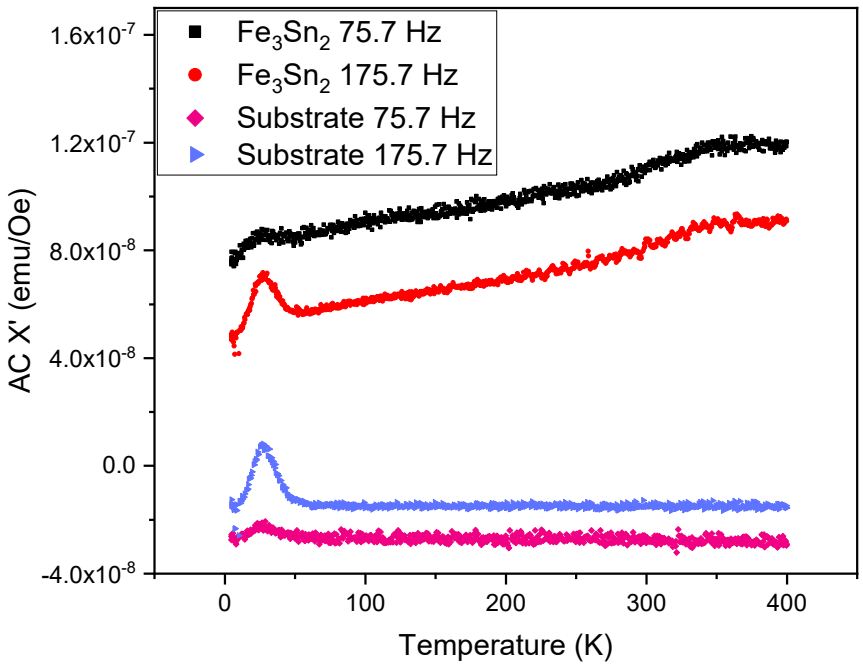

Figure 5.7: AC susceptibility for both the Fe_3Sn_2 film as well as a bare Al_2O_3 substrate measured with applied AC field amplitude of 0.6 mT upon cooling. The distinctive feature at 40 K is associated with the oxygen content of the substrate making the analysis of other features in this temperature region difficult.

magnetocrystalline anisotropy vs. the saturation magnetisation squared for the thin films (which are themselves of course both functions of temperature). The theory of exchange discussed in section 2.2.1 is completely isotropic, though in real crystals, the symmetry of the environment can cause an anisotropy in the exchange interaction which is called two-ion anisotropy. This magnetisation squared dependance for the Callen-Callen scaling matches well with the two ion anisotropy reported in the literature [129] and so we can conclude in all three films that the Fe moments are experiencing this effect.

Another method to examine the magnetic ordering within the films is the use of Zero-Field Cooled/Field Cooled measurements as discussed in section 3.6.2. In Figure 5.9 results of both ZFC and FC measurements are shown for all three films in both regular and oven mode. The demagnetisation procedure was generally least successful on the Fe_3Sn_2 film due to its significantly lower coercivity making the introduction of magnetic disorder very difficult. In (a) we can see that at low temperatures a disordered state was frozen within the film that is rapidly melted through the rising temperature, having fully melted by 50 K. Comparison with the coercivity curve in Figure 5.6 shows that this simultaneously occurs with the rapid drop in coercivity within the Fe_3Sn_2 film and so could be considered complementary evidence for the spin glass state. It is however hard to discern whether this rapid increase in magnetisation is being caused by the freedom being introduced to the spins to realign or the freedom of the domain walls to begin moving and resizing the magnetised regions within the film. As the temperature continues to rise the expected decrease in magnetisation occurs as discussed in section 5.2. On the FC sweep the curve follows the expected magnetisation vs. temperature dependence with no significant deviation. The oven-mode measurements are shown in (b) for the Fe_3Sn_2 film with a much more gradual rise over a change of 200 K which I much more strongly associate with the gradual thermal excitation of the most stubbornly pinned domain walls. A small dislocation is visible at 575 K on both ZFC and FC curves. There is the possibility that this is a signature of the spin reorientation transition that is shown in bulk Fe_3Sn_2 [65]. Even at high temperatures the film still maintains an IP easy axis, but the data of Figure 5.8 does not extend to these high temperatures, due to the lack of an OOP oven mode for the SQUID, so it is not possible to know if the in-plane anisotropy is significantly reducing which we might expect for a spin reorientation transition.

For the Mixed film, we can see that the ZFC curve only ever increases in Figure 5.9 (c) before plateauing at 380 K. In Figure 5.9 (d) the ZFC curve has a broad peak at 475 K before the magnetisation begins to reduce again. The exact interpretation in the Mixed phase film is

difficult due to the likely interaction of the AFM and FM FeSn and Fe_3Sn_2. It is interesting to note again, however, that 380 K corresponds to the minimum in the Mixed film's coercivity curve shown in Figure 5.6 (b), as well as 475 K being the location of a kink in the increasing coercivity.

For the FeSn film, a clear kink is seen in both ZFC and FC measurements in the regular mode, and in the ZFC measurement in the oven mode. This corresponds very closely with the reported Néel temperature of FeSn at 370 K, and so likely indicates the transition of the FeSn from antiferromagnetic to paramagnetic [117]. Normally this transition in an antiferromagnet would be associated with a decrease in magnetisation on the high temperature side of the kink [130] but in this case, the presence of the ferromagnetic Fe_3Sn_2 impurities likely explains the continued increase, although with reduced gradient. In the oven mode measurement the sharp kink remains at 370 K but is also accompanied by a less severe one at 450 K.

The Néel temperature of 370 K would also correspond with the minima in the coercivity seen for the Mixed sample in Figure 5.6. It seems reasonable then to conclude that this phenomenon is being induced by the antiferromagnetic-paramagnetic transition although the exact mechanism is still unknown.

5.5 High Temperature Annealing

Since the samples were grown at 400 °C (673 K), the thermal stability was expected to be good up to around this point. Figure 5.10 shows a hysteresis loop for the Fe_3Sn_2 sample at 750 K as well as a repeat measurement taken an hour later. Over the course of one loop there is a significant magnetisation drift of about 20 ± 5 emu/cm^3 which is visible as the end point being above the start point and the loop not "closing".

This drift becomes even more noticeable when the sample is left at a temperature of 750 K with a rise in M_s of 170 ± 10 emu/cm^3 after the hour had passed. If there was a significant temperature lag between the actual sample temperature and the recorded temperature, we would expect this magnetisation to reduce over the course of an hour (as the sample catches up with the recorded temperature of 750 K). This increase can only be explained through a change occurring within the film, likely a crystallographic change. This is confirmed by Figure 5.11 which shows the XRD pattern before and after the high temperature treatment has occurred. The absence of the Pt peak as well as the emergence of a series of three sharp equal intensity peaks at 39°, 42° and 44°, indicate that the Pt has formed an alloy with Sn as discussed in section 4.4 and matching with XRD patterns for Pt-Sn alloys reported by R. Srinvasan *et al.*

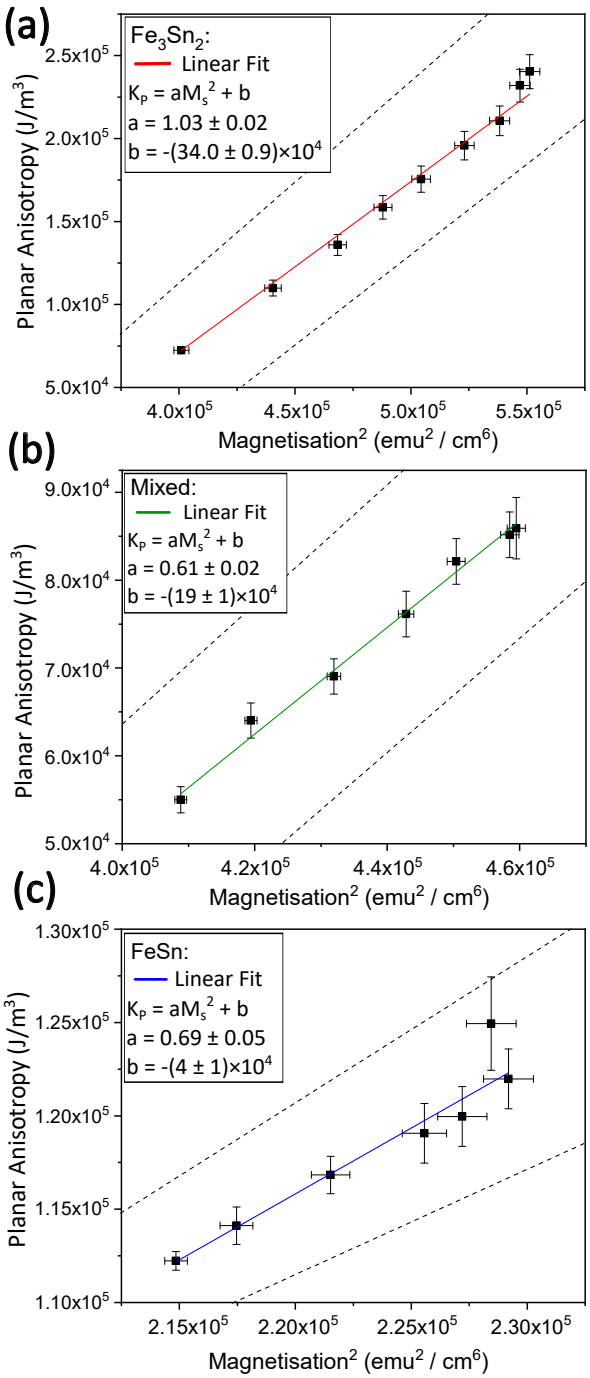

Figure 5.8: Uniaxial magnetocrystalline anisotropy vs. saturation magnetisation squared for the (a) Fe_3Sn_2 film, (b) Mixed film, (c) FeSn film. The dotted lines indicate the systematic uncertainty introduced by dividing the moments by the volumes of the films.

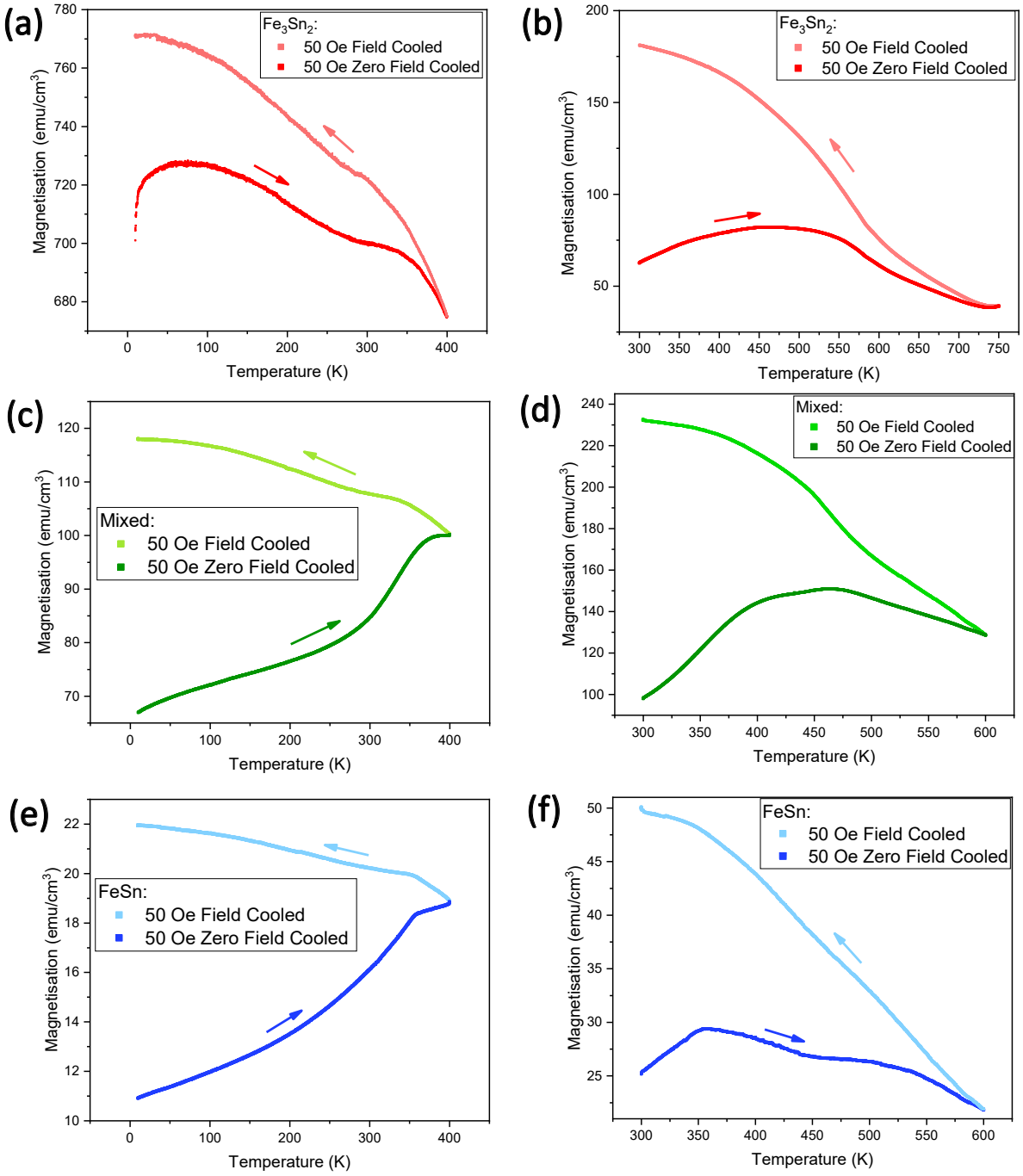

Figure 5.9: ZFC/FC curves for the (a) Fe_3Sn_2 film with the SQUID in regular mode; (b) Fe_3Sn_2 film with the SQUID in oven mode; (c) Mixed film with the SQUID in regular mode; (d) Mixed film with the SQUID in oven mode; (e) FeSn film with the SQUID in regular mode; (f) FeSn film with the SQUID in oven mode. All samples were first demagnetised at high temperature and then cooled in no field as a preparatory step. Then, a 5 mT field was applied and the sample was warmed, then cooled again.

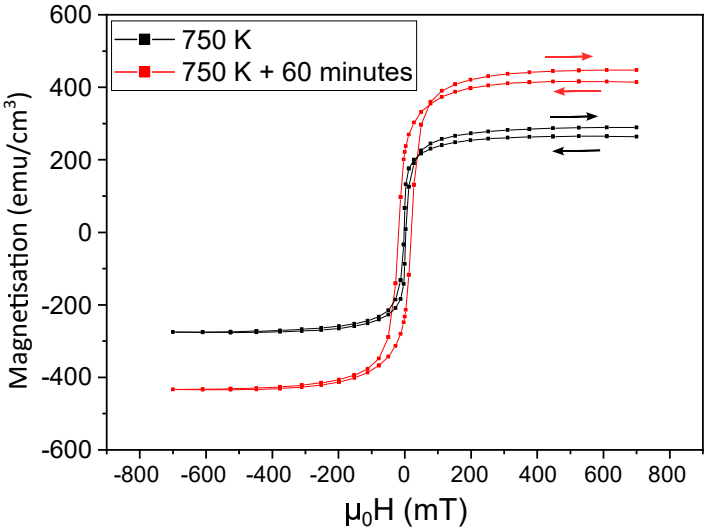

Figure 5.10: Hysteresis loop for the Fe_3Sn_2 film taken at 750 K with an hour between the measurements. Over the course of one loop there is a significant magnetisation drift of 20 emu/cm^3 which becomes even more noticeable when the two loops' saturation magnetisations are compared with a change in M_s of 170 emu/cm^3.

[131]. A Pt-Sn alloy formation could also act to explain the increase in magnetisation due to the fact that any regions of Fe_3Sn_2 or FeSn will have their Sn content leached away leaving a sample containing regions of pure Fe and Fe_5Sn_3 which in turn will increase the overall magnetisation of the film. There is also the possibility that, since 750 K is far above the 510 K melting point of Sn [132], there is significant evaporation/sublimation of the Sn into the high vacuum of the SQUID oven.

In Figure 5.12 we see that the high-temperature treatment has also introduced a significant transition in the ZFCFC measurement at low temperatures. The step at 120 K exists in both ZFC and FC branches though with different magnitudes. There is the strong possibility that it is caused by some crystallographic phase change that has been introduced now that the film is some mix of Fe_3Sn_2, PtSn and likely Fe_5Sn_3, although no exact match to this transition has been found in the literature to date.

5.6 Conclusion

The thin films of the Fe-Sn alloys have distinct magnetic properties beyond those seen in bulk samples. Through the measuring of hysteresis loops over a range of temperatures, the change

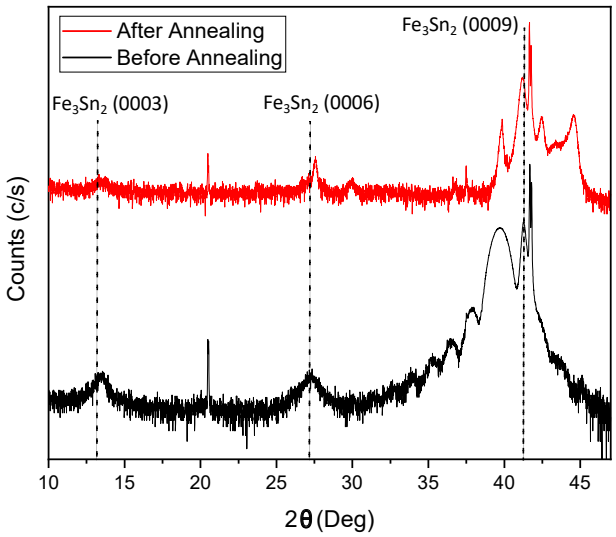

Figure 5.11: XRD measurements of the Fe_3Sn_2 film before and after being brought to 750 K in the SQUID magnetometer. Signs of the original Fe_3Sn_2 remain, indicated by the dotted lines. The loss of the Pt XRD peak at $40°$, as well as the presence of further higher angle peaks in the annealed sample, likely implies the formation of a Pt-Sn alloy.

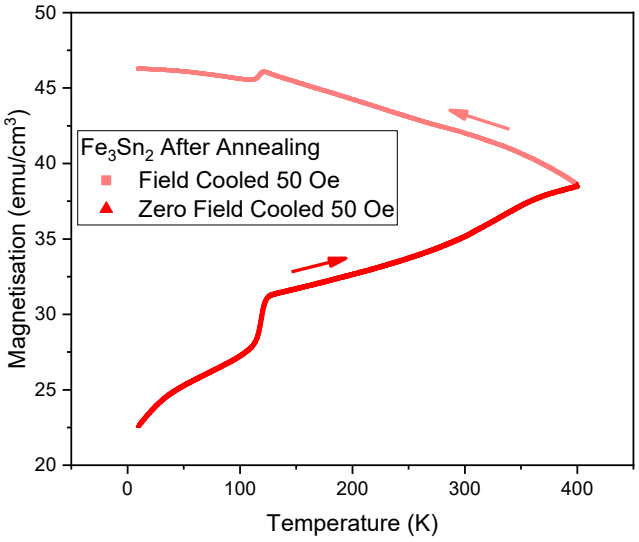

Figure 5.12: ZFCFC measurement of the Fe_3Sn_2 film after being brought to 750 K in the SQUID magnetometer. A distinctive transition is now visible at 120 K in both branches.

in saturation magnetisation as a function of temperature has been shown to agree well to the Bloch-$\frac{3}{2}$ model for magnon excitation, which allows the spin-exchange stiffness to be extracted and compared to results from the literature. Beyond this, tangential evidence for a spin-glass state in Fe_3Sn_2 film has been presented, while the FeSn film shows clear signs of the expected Néel temperature.

The Mixed film, likely due to the interplay between FM and AFM regions, shows a unique and unexpected minimum in its coercivity. The introduction of an exchange bias model to try and explain this is an avenue for future work.

The temperature instability of these thin films at high temperature has also been demonstrated. Temperatures above 700 K were shown to permanently alter the crystallographic properties of the thin films leading to the formation of undesired phases and Pt alloys.

Chapter 6

The Electronic Properties of Fe_3Sn_2 Thin Films

6.1 Introduction

This chapter contains the work of measuring the electrical properties of an ultra-thin Fe_3Sn_2 film with $t = 5$ nm, produced in the same way as described in section 3.2. An XRD pattern for this film, presented in Figure 6.1 (a), shows that this film has a high proportion of Fe_3Sn_2 content, and corresponds well to the Fe_3Sn_2 film discussed in the characterisation of Chapter 4. Hall bars were produced using the methodology discussed in section 3.7. By scribing the substrate before growth, the expected orientation of the resulting grown film can be used to produce a Hall bar that will lie (to within a few degrees) aligned to the underlying crystal structure. In this case, as shown in Figure 6.1 (b), the Hall bar is orientated so that current will flow down the **a** direction of the crystal lattice.

The seed layer of this film is 3 nm of Pt which means a considerable fraction of the current density passes through this seed layer. All data was corrected according to the equations and methods laid out in section 3.8.1. The values for the Pt resistivity were measured from a pure Pt thin film, grown in the same method as the seed layer, and fashioned into an identical geometry as the full Fe_3Sn_2 film. Figure 6.2 shows the resistivity of the Pt seed layer, ρ_s, the total measured resistivity, ρ_T, and the extracted resistivity of just the Fe_3Sn_2 film, ρ_f. This film was capped with a 20 nm layer of Al_2O_3. Since Al_2O_3 is an insulator, current flow through this cap will be minuscule compared to current through the metal layers and completely ignorable.

6.2 Temperature Dependent Resistance

By measuring the resistance of a sample as the temperature is changed, it is possible to extract a value known as the Residual Resistivity Ratio (RRR) which is the ratio of the resistivity at a high temperature with the resistivity at a low temperature. Most resistance in a metal at high temperatures is produced by electron-phonon scattering but at low temperatures, where phonon population numbers rapidly reduce, the resistance eventually becomes dominated by the scattering from impurities within the material which is temperature independent. The RRR (between 290 K and 5 K) was found to be 2.055 ± 0.003, which for a thin film is a reasonably high value. By fitting the Bloch-Grüneisen formula to the low temperature (≤ 100 K) region, shown in Figure 6.3, values for the residual resistivity, ρ_0, electron-phonon coupling parameter, A, and the Bloch-Grüneisen temperature, Θ, can be extracted. These were found to be $\rho_0 = (1.2778 \pm 0.0002) \times 10^{-7}$ Ωm, $A = (3.92 \pm 0.01) \times 10^{-7}$ Ωm, and $\Theta = 179.2 \pm 0.2$ K. Although not exactly matching, Θ is often approximately the Debye temperature of the

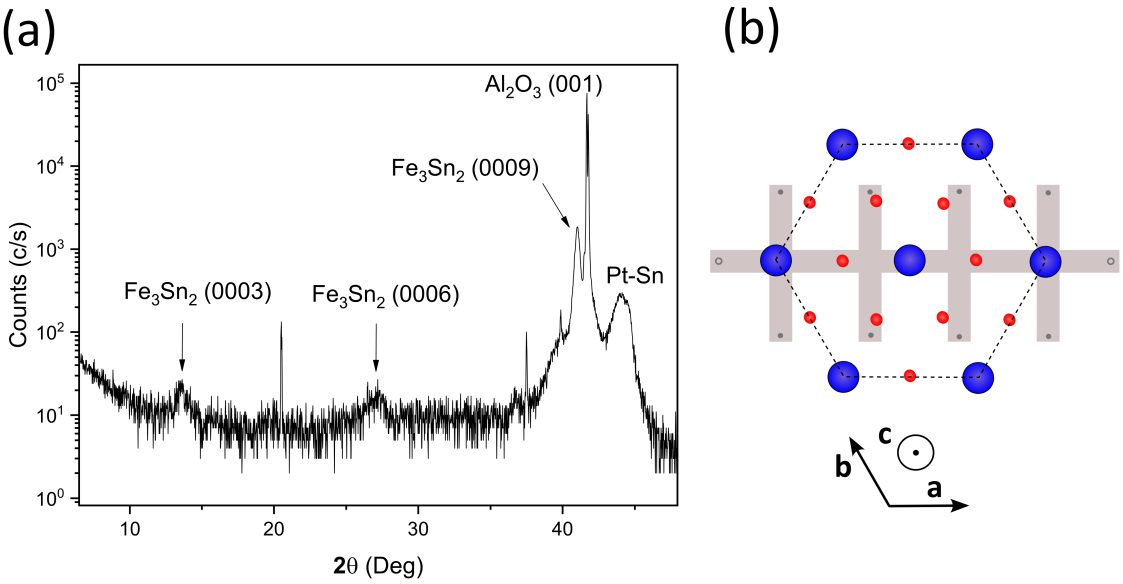

Figure 6.1: (a) XRD pattern for the 5 nm Fe_3Sn_2 film with a 3 nm Pt seed layer used in the transport measurements in this chapter. (0003), (0006) and (0009) Fe_3Sn_2 reflections are visible. (b) Orientation of the produced Hall bar relative to the expected underlying crystal structure assuming perfect epitaxial growth (compare to Figure 3.13 for the detailed Hall bar diagram).

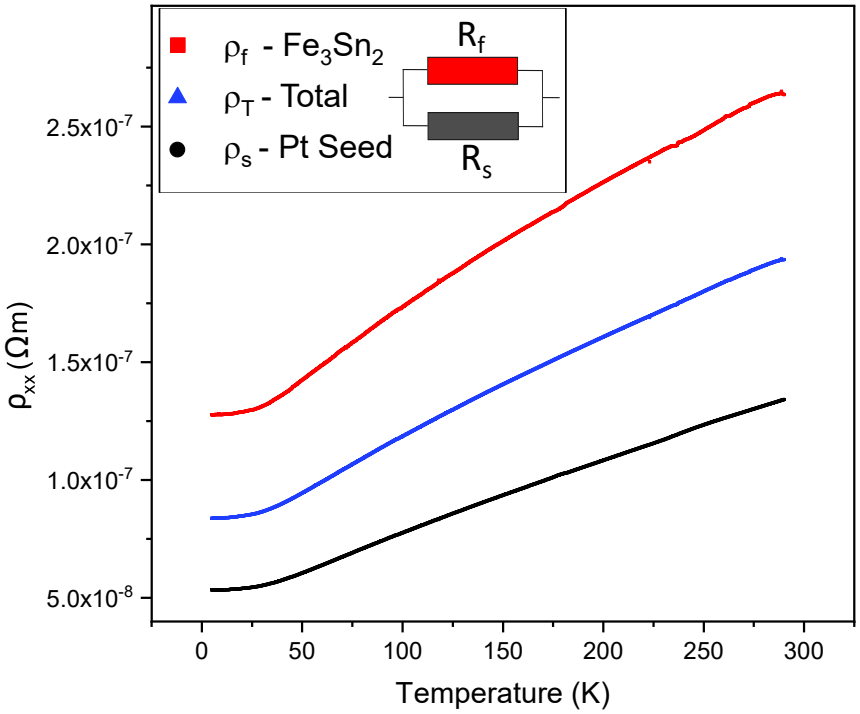

Figure 6.2: Resistivity of the Fe_3Sn_2 film, ρ_f, the total measured film, ρ_T, and the Pt seed layer alone, ρ_s, against temperature. The inset shows a rough schematic of the two resistor model.

material. Under this approximation we can use:

$$k_B\Theta = \hbar\omega_D = \hbar v_s \left(6\pi^2 n\right)^{\frac{1}{3}}, \tag{6.1}$$

to estimate the speed of sound in Fe_3Sn_2, where k_B is the Boltzmann constant, $\hbar$ is the reduced Planck constant, ω_D is the Debye frequency, v_s is the speed of sound in the material, and n is the number density of atoms. Using this equation, we can calculate the speed of sound in Fe_3Sn_2 as $v_s = 2244 \pm 2$ ms^{-1}. This is significantly less than the speed of sound in pure Fe, $v_s = 3537$ ms^{-1}, and very close to that of pure Sn, $v_s = 2220$ ms^{-1} (these values obtained by doing the weighted average of longitudinal and transverse wave speeds in [132]). As a result, this value seems very much as expected, and it could be indicating that the primary mode of vibration in the a-b plane is through the stanene layers, though it is again worth noting that the Debye model assumes an isotropic crystal structure, which we know is highly inaccurate for Fe_3Sn_2, and so we expect this speed of sound itself to be some weighted average of the speed of sound along the a-b plane and c-plane.

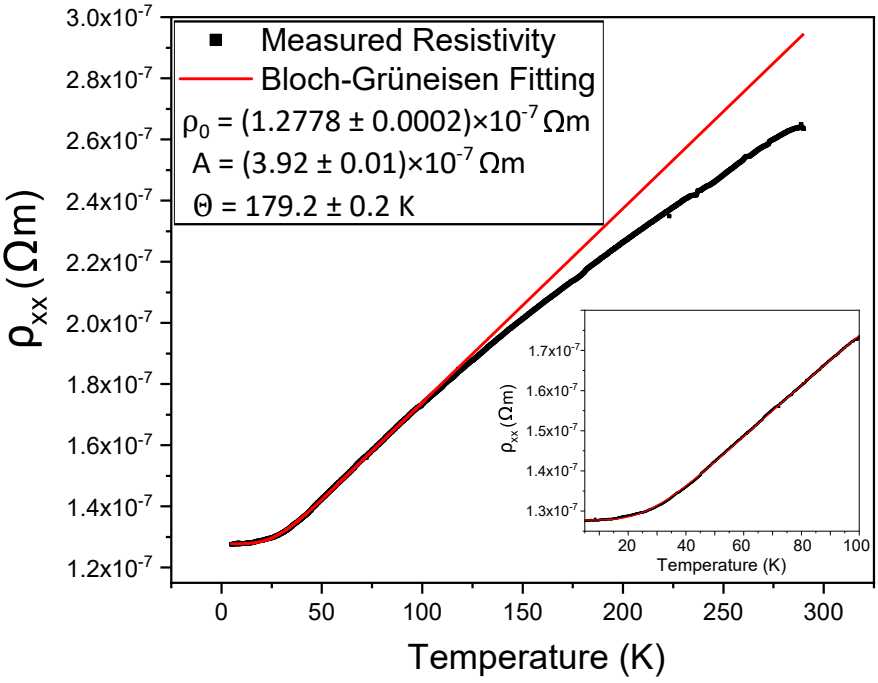

Figure 6.3: Resistivity of the Fe_3Sn_2 thin film while varying temperature. The Bloch-Grüneisen law has been fitted to the data less than 100 K.

The fitting works very well for low temperatures, but deviation from the expected linear Bloch-Grüneisen fit can be seen at higher temperatures, with magnetic interactions offering a possible explanation, as there is no magnetic contribution within the Bloch-Grüneisen formula, and we expect magnon excitation to play a more significant role at higher temperatures, as explained in section 2.2.3.

6.3 Resistance Vs Field

By measuring the transverse resistivity, ρ_{xy}, and the longitudinal resistivity, ρ_{xx} as a field is applied in the Out-Of-Plane (OOP) orientation, we are able to measure the effects this magnetic field is having on electron trajectories in the material, as discussed in section 2.5. From ρ_{xy} we can find the Anomalous Hall Effect (AHE) and the Ordinary Hall Effect (OHE) and from ρ_{xx} we can find the percentage Magnetoresistance (MR). Then, by repeating these measurements at different temperatures, changes in the dominant charge carrier type and their behaviour with temperature can be revealed.

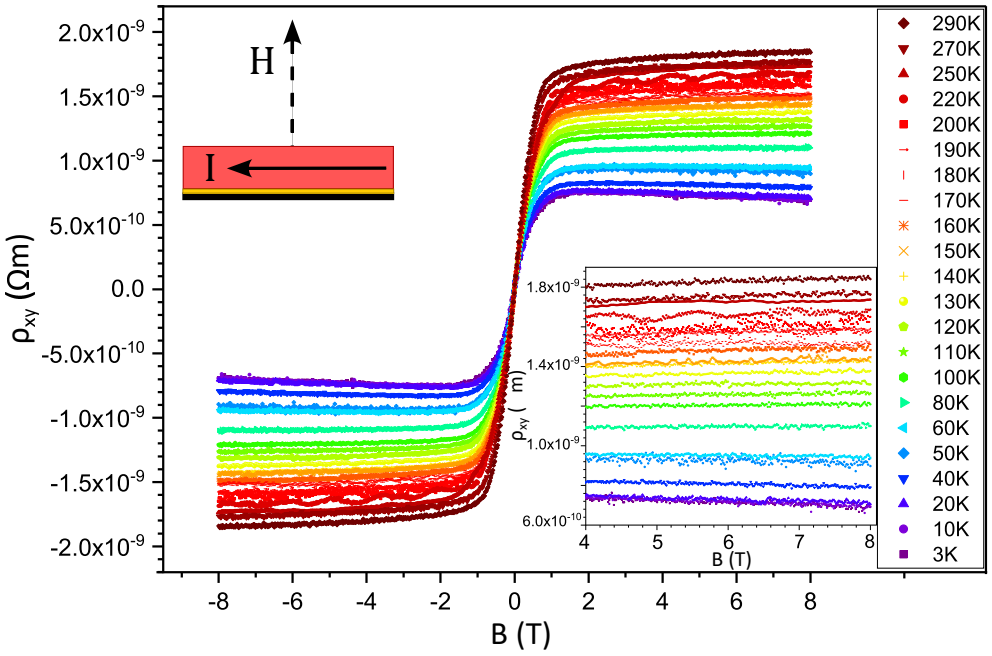

Figure 6.4: Transverse resistivity (or Hall resistivity), ρ_{xy}, as a function of field measured for a range of temperatures. A large anomalous Hall resistivity is present which saturates allowing the ordinary Hall resistivity to become apparent at high fields as seen in the diagram inset. Also shown in the inset is the current-magnetic field orientation during the measurement.

6.3.1 Anomalous and Ordinary Hall Effect

Figure 6.4 shows the measurements of ρ_{xy} for the 5 nm film across a large range of temperatures. The strong ferromagnetic nature of the film means that there is also a strong AHE. We see this saturates at the 2 T point, which is consistent with the OOP saturation field in section 5.2. Beyond this, a linear OHE is observed with a small positive gradient of at most $R_o = 1.5\times10^{-11}$ Ωm T^{-1} which is achieved at 290 K. This is comparable, yet still smaller than the room temperature OHE for pure Fe, $R_o = 2 \times 10^{-11}$ ΩmT^{-1} [133].

This gradient, and therefore the resulting OHE, reduces as temperature is reduced until a change-over point where the gradient reduces to $R_o \approx 0$ at 75 K and becomes negative for temperatures below this point. This sign change in R_o indicates that a change of the dominant carrier type has occurred, with holes being dominant at temperatures above 75 K and electrons being dominant below 75 K.

Further analysis of a "one carrier" model is shown in Figure 6.5. The extracted AHE

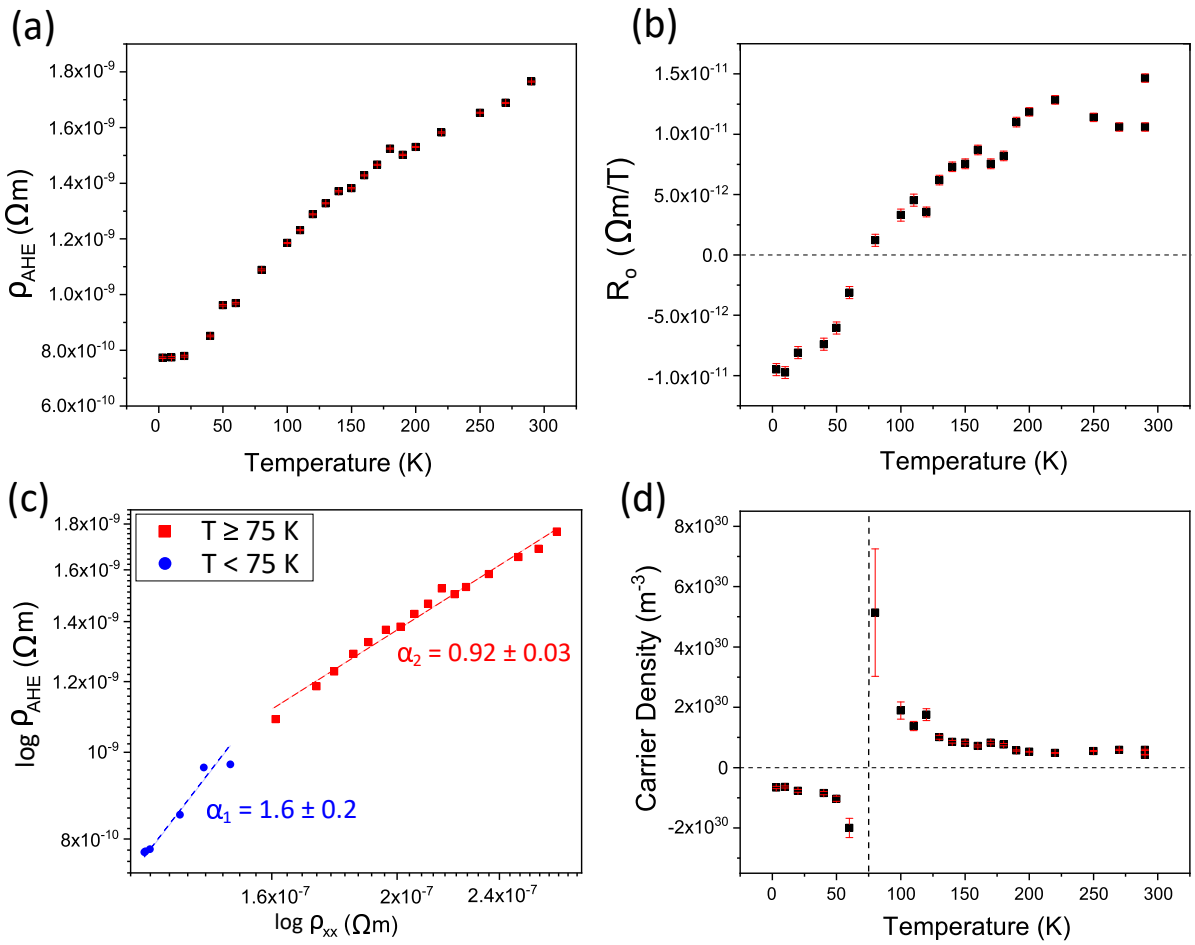

Figure 6.5: Figures showing: (a) the anomalous Hall effect vs temperature. (b) The ordinary Hall effect vs temperature showing a sign-change. (c) The AHE plotted on a log-log scale against the longitudinal resistivity, ρ_{xx}. The exponent is found to change significantly from low to high temperature. (d) The carrier density calculated using a single carrier model from (b) vs temperature showing a non-physical divergence in carrier density.

resistivity, ρ_{AHE} and the OHE, R_{o}, are shown in Figure 6.5 (a) and (b) respectively. The AHE is strongly temperature dependent, increasing as temperature increases. Eventually, above the Curie temperature, we expect the AHE to drop to zero and so this temperature dependance will arise from an intrinsic, side jump, or skew scattering mechanism [52]. The origin can be explored by examining the scaling between ρ_{AHE} and ρ_{xx} which is shown in Figure 6.5 (c). The log-log plot reveals a change in the exponent α in $\rho_{\text{AHE}} = \rho_{\text{xx}}^{\alpha}$, which is found to be $\alpha_1 = 1.6 \pm 0.2$ below 75 K and $\alpha_2 = 0.92 \pm 0.03$ above 75 K. In section 2.5.1 the work of Q. Wang *et al.* [79] and T. Kida *et al.* [92] are discussed, who present a scaling law of $\alpha = 1.93$ and $\alpha = 3.15$, with the discrepancy put down to sample quality differences from their single crystal growth methods. Since this scaling is not reported elsewhere in the literature for other material systems, these papers associate it with extraordinary origin due to the spin frustrations. In our case, a scaling law of $\alpha \approx 1.6$ is discussed in the review article by N. Nagoasa [134] and was found to exist in ultra thin sputter deposited Fe and ferrite films, though the exact origin is still an "open issue" according to Nagoasa [52], though the fact it is present in a range of ferromagnetic films might indicate it is some anisotropic effect.

At temperatures above 75 K, we observe a change in scaling coefficient. No correspondence can be found in the review article of N. Nagoasa [134], but the work by Q. Wang *et al.* [79] reports a jump at 100 K in their ρ_{AHE} vs ρ_{xx} data, though with no significant change in scaling coefficient. They associate this with the spin reorientation in their films occurring at this temperature. Our results indicate that this may be a misattribution, with some more fundamental change in the AHE being responsible for this reported jump, since it also coincides with the carrier type change-over and does *not* cleanly coincide with the temperature of spin reorientation which will be discussed in section 6.5. The coefficient $\alpha_2 = 0.92 \pm 0.03$ is close to linear, which can be indicative of a skew scattering mechanism at temperatures $\gtrapprox \Theta$, the Debye temperature of the material. From section 6.2, we believe $\Theta = 179.2 \pm 0.2$, which doesn not correspond well to this 75 K change transition, but could indicate that there is some crossover regime where multiple AHE mechanisms are present of an extraordinary nature. A small note should be made of the possibility of a sublinear contribution to the AHE scaling at high temperature. There is again discussion by N. Nagoasa [52] of scaling coefficients between $0.2 - 1.0$ being associated with electron hopping in materials containing a Berry curvature, though this is present almost exclusively in non-metallic materials.

For the OHE, shown in Figure 6.5 (b), we see a linear change of R_{o} as the temperature is increased with the change from negative gradient (electron type) to positive (hole type)

carriers at 75 K. Reports of a carrier type change-over are present, though highly inconsistent in the literature. It is discussed in section 2.5.1 and highlighted again in 2.6.3. Here, I come squarely on the side of a carrier type change-over which has been a highly consistent feature of many samples grown over the course of this work. However, the way the carrier type change occurs is not a form that is expected. In a simple model, where only one carrier type is dominant and is responsible for all the measured conductivity or resistivity, we would be able to calculate the carrier density, n, from the OHE coefficient, R_o, from:

$$n = \frac{1}{R_o e}\,, \tag{6.2}$$

where e is the elementary charge. Figure 6.5 (d) shows the values for n, though due to the linear change of R_o through 0, the carrier density calculated from 6.2 diverges at 75 K. Even at temperatures far from this divergence, the carrier density is unphysically large, with the carrier density approaching $n = -(6.5 \pm 0.3) \times 10^{29}\ m^{-3}$ at low temperatures and $n = (5.0 \pm 0.5) \times 10^{29}\ m^{-3}$ at high temperature. When compared to the atomic number density of $6.034 \times 10^{28}\ m^{-3}$ from section 2.3, each atom would need to delocalise $8 - 10$ electrons or holes to account for these carrier densities. Since this has no physical basis, the explanation is that the underlying assumption of this model, that a single carrier type dominates all the others and is responsible for the vast majority of electrical transport, is wrong. The sign change of the OHE tells us that both an electron and hole band are intersecting the Fermi surface, and so are contributing to the conductivity, and it appears that a two carrier model would be required to extract the true carrier density at all temperatures below room temperature.

However, the two carrier model requires either a small non-linearity in ρ_{xy} at high field, which we do not observe, or a simultaneous fit to the longitudinal ρ_{xx} resistivity. In our case, as we shall discuss in the next section, these films have a large negative MR due to their ferromagnetic nature, which means a fit to the two carrier model (which only predicts positive MR) is not possible.

6.3.2 Transverse Magnetoresistance

Figure 6.6 shows the transverse MR with the field applied OOP of the ultrathin film across a range of temperature. At low temperatures the strong negative MR eventually saturates, and likely the standard Lorentz MR proportional to B^2 would become apparent if we had access to higher fields. At higher temperatures above 200 K, we observe a small positive MR to be

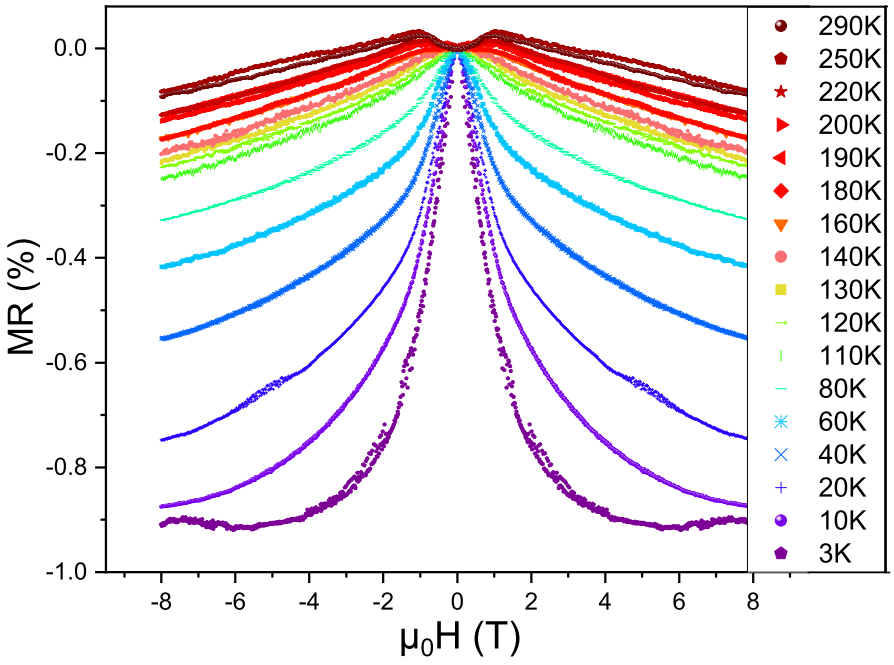

Figure 6.6: Magnetoresistance (MR) as a percentage change for a range of temperatures. At low temperatures, we can see an eventual saturation of the negative MR.

present below 2 T. Since this is the OOP saturation field, the likely explanation is that this is an effect arising due to the Anisotropic Magnetoresistance (AMR) which will be discussed later. We would expect an AMR effect to be present at all temperatures, but since the magnitude of the negative MR reduces as temperature increases, 200 K is simply the first measurement where the positive AMR can overcome the negative MR to produce a slight positive MR. This is evidenced by the fact that all the field sweeps have a slight kink visible just below 2 T.

An exact quantitative model of negative MR is difficult to find in the literature. Instead, a phenomenological argument is provided based on the qualitative source of negative MR discussed by S. Blundell [29] and the results of B. Raquet *et al.* [35] which were discussed in section 2.2.4. There, it is argued that ferromagnets experience negative MR due to the magnetic field suppressing the magnon scattering within the material. Here, we will represent this by subtracting a term proportional to $|B|$ from the positive quadratic MR, leading to the expression:

$$\frac{\Delta\rho}{\rho} = aB^2 - b|B|\,, \tag{6.3}$$

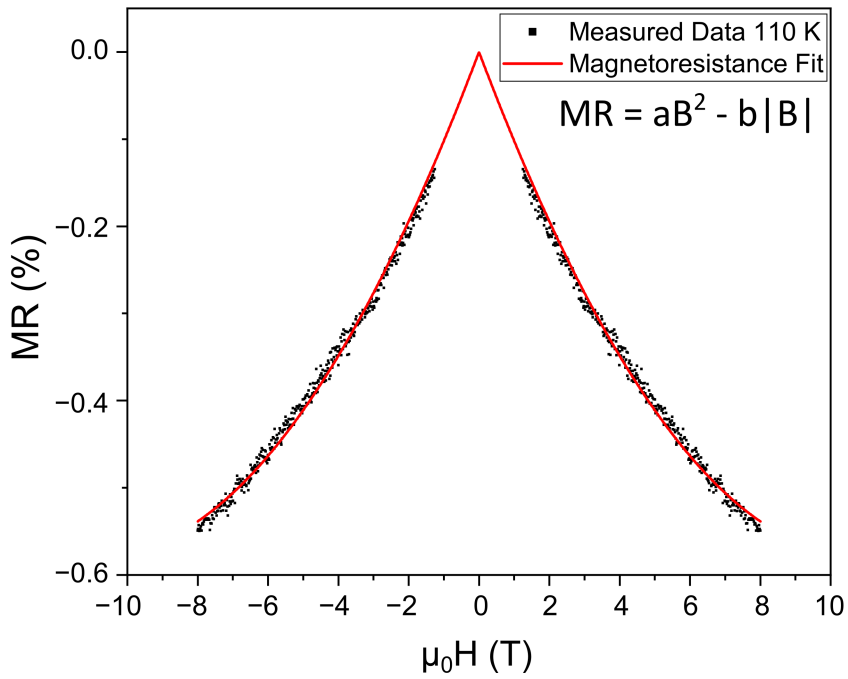

Figure 6.7: Example of the phenomenological fitting of the MR data. Two coefficients, a and b, are extracted corresponding to the positive Lorentz MR and the negative ferromagnetic MR respectively. Data between -2 T and 2 T is not fitted to remove the effect of changing magnetisation to the transport properties.

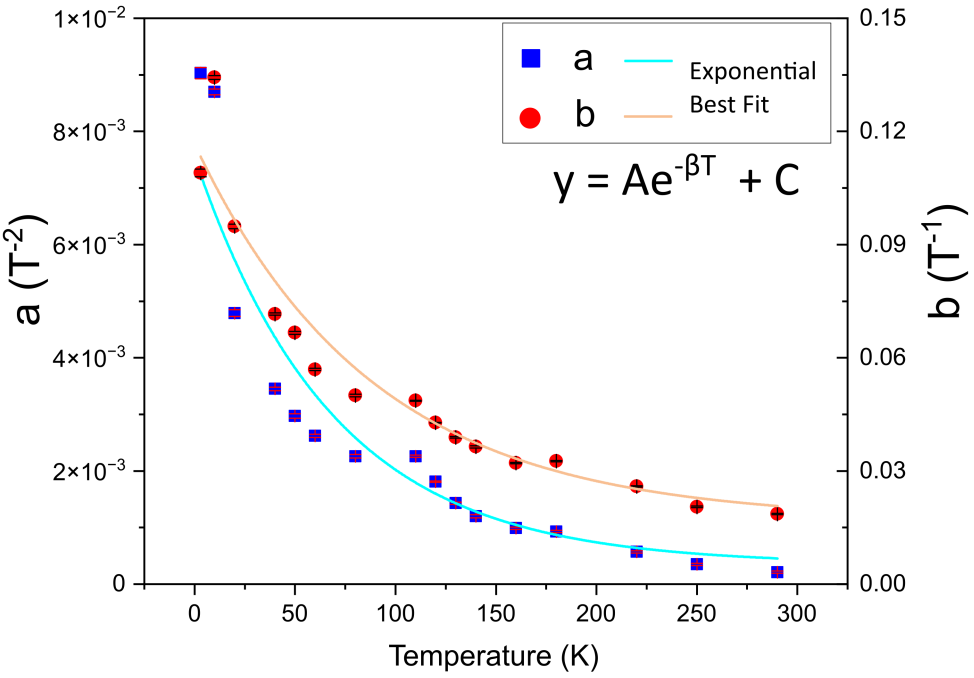

Figure 6.8: The fitting parameters a and b from the phenomenological model varying as a function of temperature. An exponential function is fitted, though the agreement to the low temperature data is poor.

where a represents the strength of the Lorentz MR and b the strength of the magnetic suppression of the spin scattering. This is not without precedent as combination of linear and quadratic forms for the MR in Fe_3Sn_2 is discussed by N. Kumar [36], again in section 2.2.4. An example of this functional fitting is shown in Figure 6.7 for the data at 110 K. Data in the region $|B| < 2$T has been removed from the fitting, due to the strong effect the changing magnetisation is believed to be having on the MR. Beyond 2 T, the magnetisation is a constant saturated value, and so no longer varies as a function of field (apart from some slight change due to the magnon gapping discussed in section 2.2.3).

The equation 6.3 was fitted to the MR data of Figure 6.6 and the parameters a and b extracted. Plotting these as a function of temperature is shown in Figure 6.8. Both a and b decrease exponentially with increasing temperature with an amplitude, A, decay rate, β, and constant offset C, given in Table 6.1. Attempts at using a function form with a $\frac{1}{T^n}$ dependence had very poor fitting.

For low temperatures, we can see that the exponential fit of 6.8 underestimates the steepness of ascent, however it is worth noting that the phenomenological fit is most poor for these low temperature values.

At high temperatures, from the value C, we see that the Lorentz MR parameter a seems to be approaching 0 as the curvature of the MR measurements reduces to a practically immeasurable degree. It is interesting to see that the spin scattering suppression, b, is also approaching a value, though this seems to be the non-zero value of $(1.7 \pm 0.5) \times 10^{-2}$. It seems then, that for temperatures above room temperature and likely up until the Curie temperature is reached, Fe_3Sn_2 will have a negative MR with a highly consistent MR gradient of $(1.7 \pm 0.5) \times 10^{-2}$ T^{-1} with curvature of $(4 \pm 3) \times 10^{-4}$ T^{-2}, which is less than the uncertainty in the gradient itself for these measurements.

It is worth comparing the MR data in Figure 6.6 with that presented in section 2.2.4 for the negative MR of Fe thin films in the work of B. Raquet *et al.* [35]. At high temperatures, the data has similarities such as showing a purely linear negative MR, but the change in gradient

Parameter	A	β	C
a	$(7.2 \pm 0.1) \times 10^{-3}$ T^{-2}	$(1.5 \pm 0.3) \times 10^{-2}$ K^{-1}	$(4 \pm 3) \times 10^{-4}$ T^{-2}
b	$(10.0 \pm 0.8) \times 10^{-2}$ T^{-1}	$(1.1 \pm 0.2) \times 10^{-2}$ K^{-1}	$(1.7 \pm 0.5) \times 10^{-2}$ T^{-1}

Table 6.1: The exponential fitting parameters, amplitude, A, decay constant, β, and constant, C, for the magnetoresistance phenomenological parameters a and b.

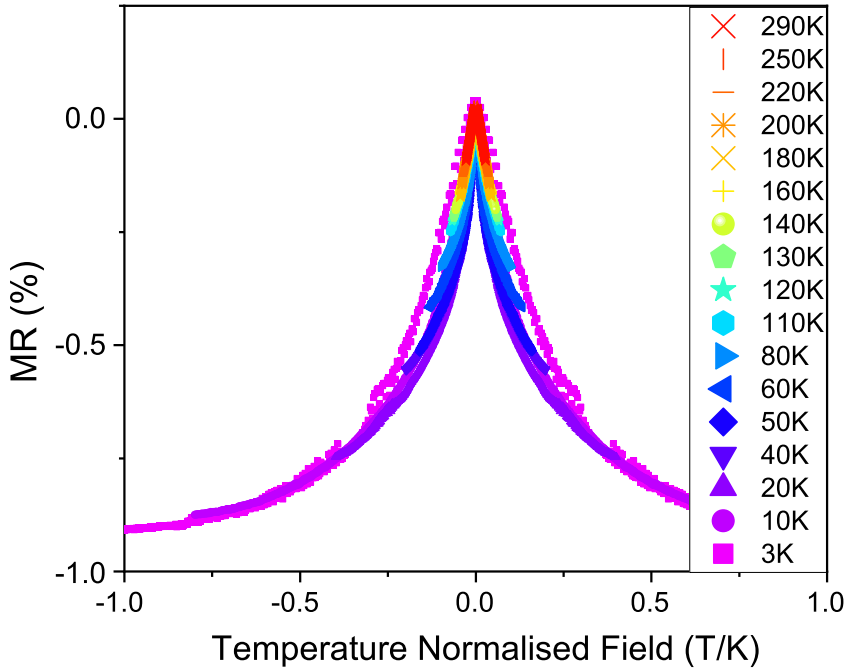

Figure 6.9: Magnetoresistance plotted against the magnetic field divided by temperature (the temperature normalised field).

for this linear slope as a function of temperature is completely reversed. Raquet found that higher temperatures lead to exponentially higher gradients as shown in the inset of Figure 2.4, while here we see the exact opposite trend in Figure 6.6. The reason for such a strong disagreement is still an open question. The MR in Fe_3Sn_2 films of N. Kumar [36] likewise show a linear negative MR, but they report a much stronger Lorentz MR at lower temperatures that has completely overwhelmed the negative MR by 60 K. We can explain this difference due to the nature of the samples of N. Kumar being highly pure single crystals grown through vapour deposition, that naturally would have more complete Lorentz orbits and a resulting stronger positive quadratic MR.

6.3.3 Universal Scaling

In order to investigate the transverse MR further, the curves of Figure 6.6 were scaled by dividing the field axis by the temperature the measurement was taken at. The result is the temperature normalised MR curves of Figure 6.9. It can be seen that there is a collapse of all the curves towards one shared function that depends only on $\frac{B}{T}$, i.e. the MR could be written

as:

$$\mathrm{MR} = f\left(\frac{B}{T}\right) , \tag{6.4}$$

which means that we can estimate the field needed to observe a notable curvature in the MR for a given temperature.

Close observation reveals that actually, this collapse into a single function is not exact. At low temperatures $\leq 50\,\mathrm{K}$, and at high temperatures, $\geq 160\,\mathrm{K}$, the correspondence is very good, but at intermediate temperatures, especially noticeable for $80\,\mathrm{K}$ and $110\,\mathrm{K}$, the resulting curve does not seem to be following the same function and has a greater than expected curvature. It is worth noticing that this temperature also corresponds to the change in AHE scaling and carrier type change-over found in section 6.3.1 and Figure 6.5, as well as also possibly being associated with a slight kink in the fitting parameters of Figure 6.8.

6.4 Orbital Anomalous Hall Effect

The cryostats described in section 3.8 have the ability to rotate the sample within the superconducting coil during measurement, effectively allowing magnetic field direction to be changed relative to the sample orientation. Although attempts are always made on loading to precisely align the sample to the field, since loading requires a moderate amount of physical effort, loss of alignment by a few degrees is an inevitability.

Following the work of L. Wang *et al.* [95] attempts were made to reproduce the measurements presented in section 2.5.2 which indicate a strong IP Hall effect in Fe_3Sn_2. Figure 6.10 (a) and (b) shows the result of measuring ρ_{xy} as the magnetic field is rotated into the plane of the film both parallel to the direction of the current, and perpendicular to the direction of current. (c) and (d) show that even slight misalignments of the field from the IP direction can produce sizeable increases in Hall resistivity, which accounts for the non-zero ρ_{xy} measurements at 90° in (a) and (b). At high field, unlike in Figure 2.17, the parallel and perpendicular rotations show no difference, once slight misalignment angles are taken into account. The samples measured by L. Wang were large μm scale single crystals grown through vapour transport, with a RRR of 12. It seems likely that the samples lacked the high crystal quality, especially considering they were only 5 nm thick, to produce an IP Hall effect that was a sizeable percentage of the OOP Hall effect.

At low fields, as shown in the insets, there is a subtle behaviour difference, in which the parallel arrangement experiences two peaks in resistivity as the field is swept in the direction

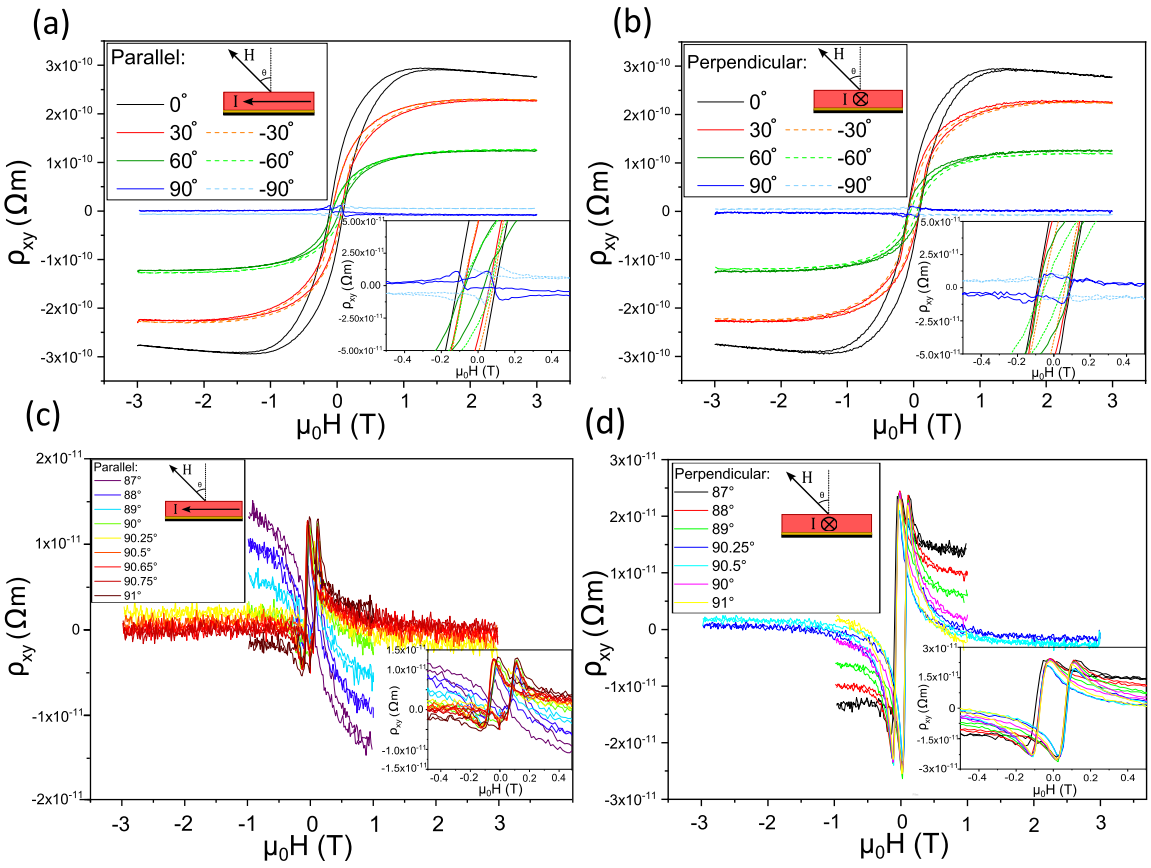

Figure 6.10: Hall resistivity, ρ_{xy}, measured as the magnetic field is rotated from OOP to IP at 3 K. Rotations are done parallel to the current direction for (a) and perpendicular to the current direction for (b). (c) and (d) are likewise parallel and perpendicular field rotations, with a very fine angular increment around the IP direction. Insets in all graphs show the zoomed in region around 0 T as well as the current-magnetic field orientation during the measurement.

Figure 6.11: Anisotropic Magnetoresistance (AMR) of the Fe_3Sn_2 thin film. (a) are the polar plots of the angular dependence of IP magnetoresistance at 10 K, for a range of fields. Current is directed down the $\theta = 0°$ direction. (b) is a schematic of the current-magnetic field orientation during the measurement. Graph (c) is the change of MR with angle for 3 and -3 T highlighting the unidirectional effect. The maximum AMR as a function of field shown in (d). Note that this is not a four fold symmetry, but in fact a two fold symmetry with a unidirectional component.

of the current, while the perpendicular orientation shows a more traditional hysteresis loop, with resistivity remaining constant until the field induces reversal of the magnetisation. These low temperature hysteretic effects are not observed in the work of L. Wang and are generally not discussed widely in the literature. Their origin is likely to be the magnetisation switching mechanism in the films. At high field, the expected result of $\rho_{xy} = 0$ is observed when properly orientated in both parallel and perpendicular cases. For the perpendicular orientation a symmetric, almost square, loop in ρ_{xy} is observed which is what is typically expected for a ferromagnet [135]. However for the parallel orientation, the ρ_{xy} is very much not symmetric about the field-axis with the central features, a pair of peaks at the IP saturation field, being both positive in resistivity. The most direct explanation, which is further explored in the next section, is that there is a unidirectional nature to the thin film which favours the magnetisation aligning in a specific direction, rather than just along a preferred axis.

6.5 Anisotropic Magnetoresistance, Hysteresis and Spin Reorientation

6.5.1 Anisotropic Magnetoresistance

Anisotropic Magnetoresistance (AMR) for the Fe_3Sn_2 film is presented in Figure 6.11 for an IP rotation in an IP field. AMR is calculated from equation 3.12, but instead of $\rho_{xx}(0)$, the average ρ_{xx} over the full 2π rotation is used.

It is worth comparing the results of Figure 6.11 to the results of section 2.5.2, in particular the paper by Y. Li *et al.* [96] which reports a highly anisotropic, almost unidirectional, magnetoresistance (for one out of a pair of samples, the other actually reports only a bias towards a particular direction, but mostly a uniaxial effect). In our results, the "forwards" (i.e. when the magnetisation lies along 0° direction) increase in magnetoresistance is not symmetric with the backwards (i.e. when the magnetisation lies along 180° direction), which corresponds very closely to these previous results. For a purely uniform ferromagnet the expectation is twofold symmetry from the graphs in Figure 6.11 (a) [136], and the breaking of this symmetry implies that the **a** axis of the crystal structure is magnetically preferred, which has been suggested by previous works such as that of L. Fenner [65]. However, there are difficulties in conclusively claiming this effect is purely a property of the Fe_3Sn_2 in our case, due to the presence of the Pt seed layer, that has been shown in ultra thin films to also contribute to a unidirectional magnetoresistance [137]. In Figure 6.11 (e) we see that growth and eventual saturation of AMR with increasing field. What's interesting is that a saturation field of 1.5 T is significantly higher than the IP magnetisation saturation measured in section 5.2, and is more similar to the OOP saturation field of $\sim$ 2 T. There are two possibilities. The first is that this is the true IP magnetisation saturation of this sample, which is possible but highly unlikely. It was not possible to extract and measure this specific Hall bar in the magnetometer after transport measurements were taken, but measurements on sister samples confirm saturation fields similar to those of Figure 5.1, and significantly less than 1.5 T. The second suggested option, is that there is a decoupling between the magnetisation vector and the AMR effect, which is possible in spin frustrated or textured systems [138].

Something worth noting is that Y. Li reports a shifting of the peak of the MR direction $\sim 20^\circ$ away from 0°, which is observed here, although the uncertainty in angle introduced when loading makes strongly claiming this to be the same effect slightly spurious.

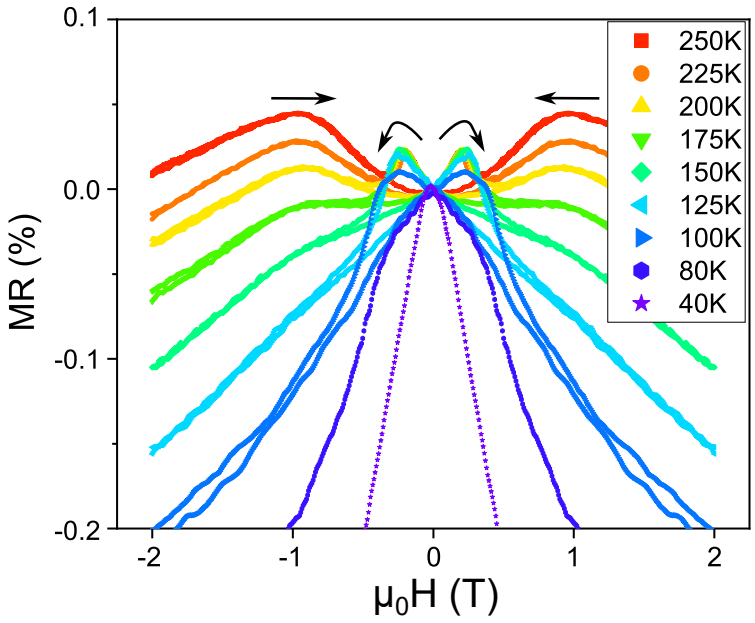

Figure 6.12: MR measurements highlighting the hysteresis present in the magnetotransport. Arrows indicate the direction of field sweep during measurement. As temperature is reduced the hysteresis remains only subtly changed until 100 K where it begins to transition and has completely vanished by 40 K.

6.5.2 Magnetotransport Hysteresis

Figure 6.12 shows measurements of the MR over a smaller field range than in Figure 6.6, where the hysteretic effects are more apparent. Samples were fully saturated with an OOP field of -3 T before the start of the positive field sweep. The amplitude of the hysteretic effects is remarkably consistent with temperature above 100 K, although there is some slight shifting in the field associated with the peak in the hysteresis by about 70 mT between 250 K and 125 K. At 100 K the hysteresis peaks have reduced and broadened significantly, and by 80 K they are no longer distinct, although they are likely responsible for some broadening in the features around 0 T. In the 40 K measurement, there is no longer any noticeable effect at all from the hysteresis. In order to explain the source of this hysteresis, it is worth considering these measurements in relation to those magnetometry measurements of Figure 5.1 (b). In these previous results we saw that in an OOP hysteresis loop, some easy axis switching still remained with a coercive field of $0.1\ T$, which was associated with some slight canting of moments from the IP direction to OOP. These coercive fields were also found to be highly temperature independent for the temperatures measured between 100 K and 300 K. It is therefore reasonable to conclude that these low field hysteretic features with positive MR are the result of OOP spin orientations, likely to be due to preference for c-axis alignment in Fe_3Sn_2 at high temperatures which is widely reported and discussed in section 2.3. As temperature is reduced, the broadening and eventual vanishing of the hysteresis is likely due to spin reorientation down into the a-b plane which begins below 125 K, is actively changing at 100 K and is largely finished at 80 K. The use of magnetotransport to detect spin orientation was the topic of the paper by N. Kumar [36], although they report no hysteresis in the MR measurements in their work and instead look at subtle changes in the MR trends with changing temperature.

6.6 Gating

By applying a voltage to the top gate, the electric field can, in theory, shift the Fermi surface within the Fe_3Sn_2. However, the free electrons in a metal will screen the electric field and cause it to decay in intensity with depth and so only a certain fraction of material will have its Fermi level shifted. The hope was that by using ultra thin films, a sufficient volume would experience the electric field to observe a change in the transport properties at key points.

Figure 6.13 shows the results of applying a ± 5 V bias voltage to the top gate while the sample was held at 160 K. Voltages higher than this incurred a significant leakage current as

the gate dielectric broke down. Up to this bias voltage, no change in the measured MR or Hall resistivity could be detected. It would be interesting to see if a more refined dielectric and top gate production process, of which there was not sufficient time for in the course of this project, could produce higher quality gated films and observe some effect under gating.

6.7 Conclusion

Through the measurement of thin film Fe_3Sn_2, we have successfully highlighted some previously overlooked features of its electrical transport. A carrier type change is shown at a temperature of 75 K, which has been previously reported, though inconsistently in the literature. Due to the work of Chapter 4 making us confident in the Fe_3Sn_2 content of these films, we believe this carrier type change is firmly established.

An AHE scaling of $\alpha = 1.6 \pm 0.2$ is shown, which is more similar to previously understood scaling in Fe based ferromagnets and significantly different than the scaling laws shown in the literature which have no previous parallel nor explanation. Previous papers, particularly the one by Q. Wang [93], report a discontinuity in their AHE vs ρ_{xx} at 100 K which they associate with spin reorientation. A discontinuity is also found, although in this work it is at 75 K and it corresponds more closely with the carrier type change, as well as a break-down of the universal scaling function $f\left(\frac{B}{T}\right)$. Combined with the fact that measurements of hysteresis reveal a spin reorientation likely occurring in the 80-125 K temperature range, we suggest that these are at most indirectly connected events.

The negative MR has also been explored across a wide temperature range of 3-290 K. The largely linear negative MR discovered is not completely unprecedented, but the exact temperature dependence is difficult to explain with current theory. Whether explained or not, the highly consistent linear MR at room temperature could offer applications in magnetic sensing technology, if the magnitude of the MR could be improved from the current 0.2% at 8 T to a value of about 4%.

Unfortunately attempts to explore the orbital Hall effect were unsuccessful, with the measured IP Hall effect being far too low to then continue and extract a possible orbital contribution. This is likely due to the films lacking enough long range crystal order in the a-b plane. Similarly, the attempts to gate the thin films did not work as the dielectric of the gates began to break down before a voltage was achieved that could induce an observable change in the transport properties of the film. I believe that with even more refined growth parameters, and more careful dielectric and gate production, both of these issues could be mitigated and

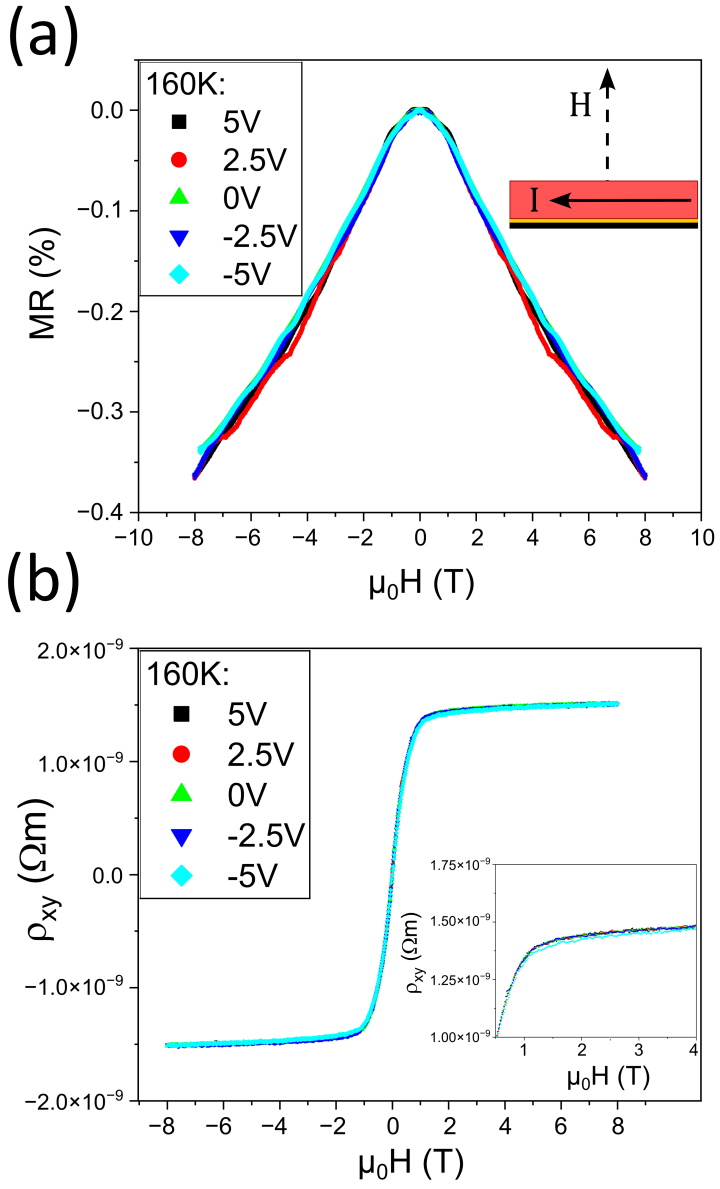

Figure 6.13: The effect of applying top gate voltages to (a) MR and (b) ρ_{xy} at 160 K. No significant variation under gating was observed, and higher gate voltages began to induce significant leakage through the gate.

offer avenues for future research.

Chapter 7

Conclusions and Future Outlook

Fe_3Sn_2 is a fascinating material, containing non trivial magnetic textures, with an ingrained fundamental frustration. This frustration is believed to have significant effects on the magnetic response and electrical transport of this material, and as a result, has been a source of theoretical and experimental interest with a particular acceleration in the last decade. The work reported in this thesis set out with the primary goal of producing high quality thin films of Fe_3Sn_2, and once produced, continue to measure their fundamental magnetic and electronic properties. Here, to conclude this work, the key steps used to reach this goal and the primary results discovered will be summarised.

7.1 Conclusion

In Chapter 4, the successful growth of epitaxial films of Fe_3Sn_2 are reported. Doubts over phase content and ambiguous XRD patterns were dispelled through the use of STEM to perform phase mapping revealing high content of the desired Fe-Sn phase, that could be tuned using Fe stoichiometric content as the only variable. These films follow the expected trends as Fe content is varied, and the resulting saturation magnetisation and coercivity for the pure Fe_3Sn_2 match well with values from the literature. Discrepancies with reported results for thin films are explained through film quality differences, with the thorough characterisation performed in this chapter forming a strong confidence in the quality of the films in this work. Three films were produced for further study, one with primarily FeSn content, one primarily Fe_3Sn_2 content, and one that was a mixed phase between the two.

In Chapter 5, the magnetic properties of these three films were examined in greater detail. The trends in saturation magnetisation, magnetic anisotropy, and coercivity were examined. An extraordinary trend in coercivity is found for the mixed phase film, perhaps indicating an antiferromagnetic-ferromagnetic interaction. Strong evidence of a discontinuity indicating the Néel temperature of FeSn was shown in the zero-field cooled measurements. Finally, a thermal instability of the Fe_3Sn_2 was reported at 750 K, with a rapid crystallographic and magnetic change when the film is taken above this temperature.

In Chapter 6, the electronic transport properties of Fe_3Sn_2 were examined. With the transport contribution of the seed layer removed, a transition point is discovered at 75 K which corresponds to both a carrier type change-over and a change in anomalous Hall effect scaling. Previous literature has implied such changes in scaling could be induced by spin reorientation, though further work of Chapter 6 implies a spin reorientation is occurring at closer to 100 K, matching well with previous literature and also providing evidence that these effects share

distinct origins.

In conclusion, the goal of producing high quality Fe_3Sn_2 films was achieved, with also initial evidence that these thin films contain some of the novel transport properties predicted in the literature, as well as features in the magnetoresistance that are not predicted and perhaps require a re-formulation of theory to be explained.

7.2 Future Outlook and Potential Further Work

The results of this thesis clearly indicate that the previously debated carrier type change-over in Fe_3Sn_2 is a real phenomena in high quality crystals. Although an intrinsic anomalous Hall effect of orbital origin could not be confirmed through the results presented here, the existence of a possible reorientation coupled scaling change is a new avenue of research.

In addition, the confirmation of an irreversible phase change in the Fe_3Sn_2 film at a temperature of 750 K, strongly indicating a Pt-Sn alloy formation, provides an upper temperature limit for the viability of films using a Pt seed or capping layer.

7.2.1 Growth Series

Although high-quality films were produced during this work, there were still consistency issues in their production. The temperature control for the sputter chamber was often temperamental, with large uncertainty in growth temperature caused by uneven heating to the different locations within the chamber. As a result, a thickness series for the Fe_3Sn_2, which would have been an interesting topic of study, was not able to be produced in a single growth session. An initial step of future work would be to perfect this growth process, either by reproducing the growth method in a different chamber, or by making alterations to the current one to reduce the temperature variations, which would allow for consistent growth series to be produced.

7.2.2 Lorentz Transmission Electron Microscopy

Due to time constraints and a series of failed planar lamellae, an initial plan of using Lorentz TEM to measure the magnetic structure in the Fe_3Sn_2 and provide further details about the mesoscopic magnetic structure in Chapter 5 did not come to fruition. The main difficulty was that the sapphire substrate was highly resistant to the focused ion beam that was used to produce the lamellae. An avenue of future work would be to attempt growth on other more suitable substrates, with options such as LAO allowing for a sacrificial layer to be used to

float off the grown thin film for planar TEM measurements. The hope would be that such measurements could reveal skyrmion, or skyrmion like, magnetic structures within the Fe_3Sn_2 thin films which would open the possibility for novel magnetic storage in these non DMI stabilised textures.

7.2.3 Gating

The process of attempting to produce a gated device which is detailed in section 3.7, with the measured results shown in section 6.6, was unsuccessful with no change being observable under gating. Over the course of the work, a dozen devices were produced and measured, with the vast majority suffering breakdowns in their dielectric at voltages of just a few V. With further work, a more reliable clean room process could be developed that allows for greater gate voltages and higher electric fields to be applied to the sample surface, which in turn opens the possibility of observing a gate dependent effect, which in turn would allow the exploration of the predicted complex band structure around the Fermi surface of Fe_3Sn_2.

Appendix A

The Fe-Sn Intermetallics

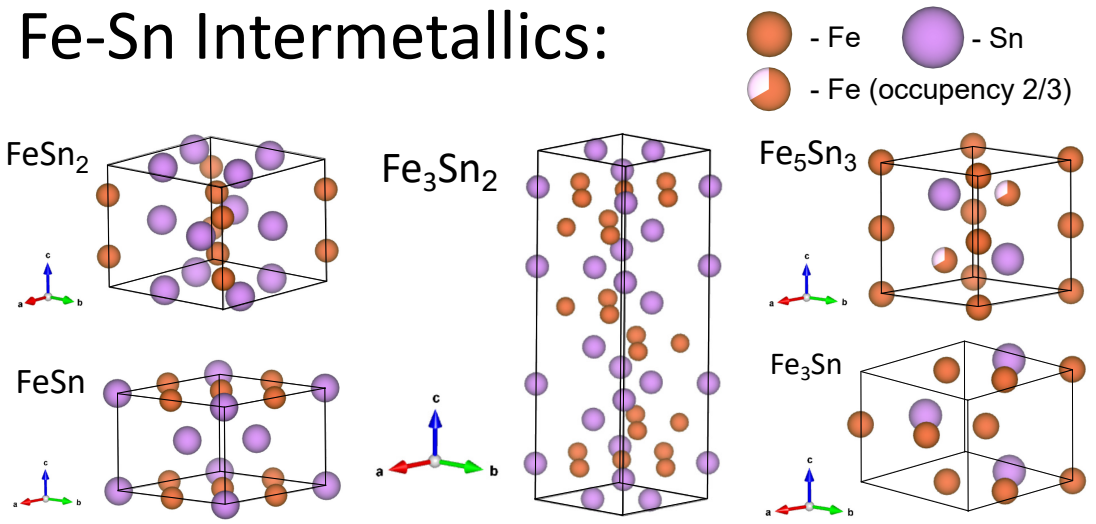

Figure A.1: The unit cells for the five Fe-Sn intermetallic alloys from [22]. Note that Fe_5Sn_3 is cubic while all other unit cells are trigonal.

This appendix is made for quick reference to the five Fe-Sn intermetallic alloys that exist. Unless otherwise stated, crystallographic data is taken from the work of Giefers and Nicols [22]. All figures were produced with the use of the Vesta software [139]. Included are diagrams of the five unit cells A.1; simulated XRD patterns from the five alloys A.2; and finally the tables showing the (hkl) values and associated angles for all the reflections from 0 to 50° for the five alloys.

Alloy	Space Group	$a-b$ (Å)	c (Å)	$\alpha-\beta$ (degrees)	γ (degrees)	Volume (Å^3)
$FeSn_2$	I 4/m c m	6.536	5.323	90	90	227.395
FeSn	P 6/m m m	5.298	4.448	90	120	108.123
Fe_3Sn_2	R -3 m	5.344	19.845	90	120	490.811
Fe_5Sn_3	P 63/m m c	4.220	5.246	90	120	80.907
Fe_3Sn	P 63/m m c	5.464	4.352	90	120	112.523

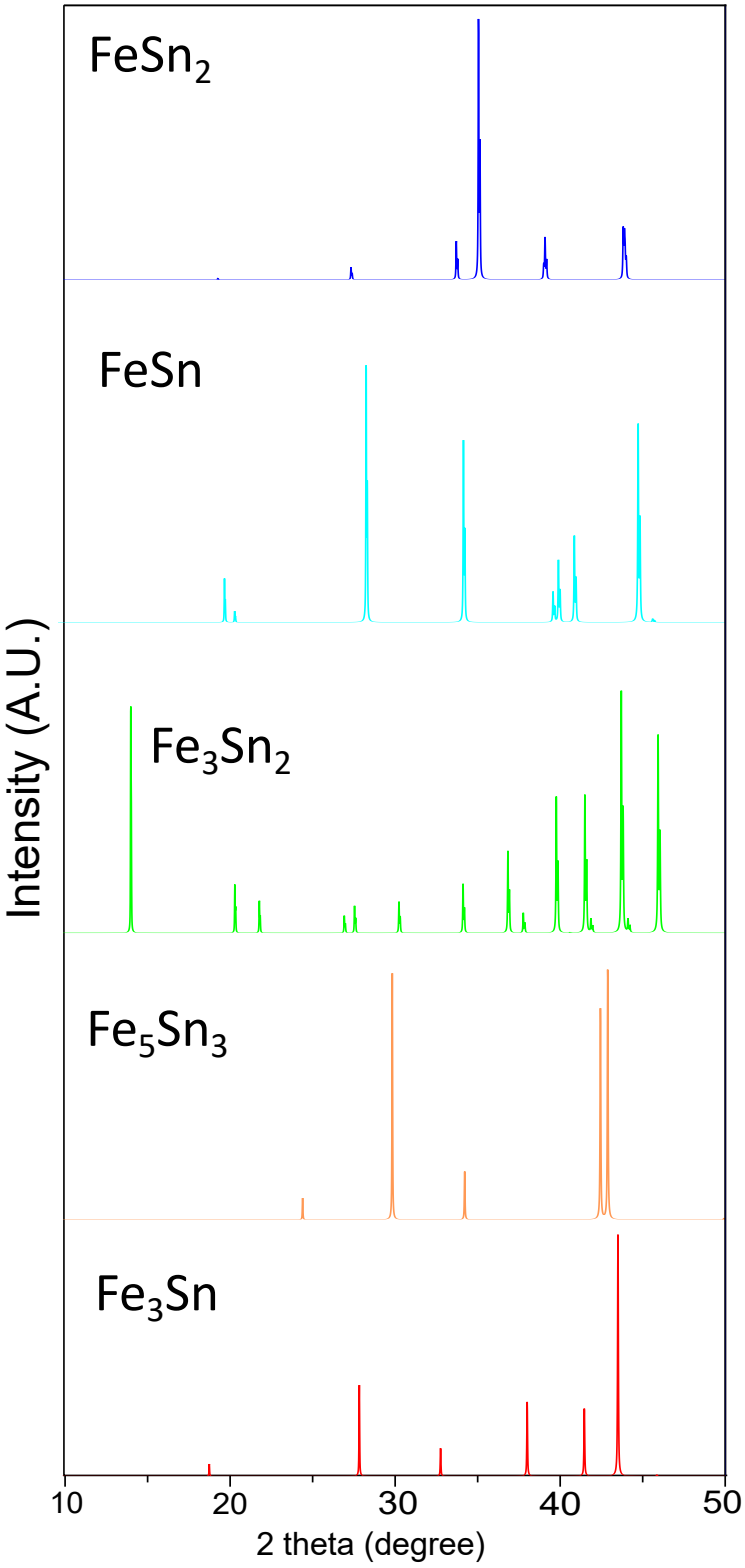

Figure A.2: Simulated powder XRD patterns from the five Fe-Sn intermetallics. Details of the specific angles and intensties can be found in the tables below.

FeSn2	hkl	d (Angstrom)	2 theta	Intensity
	110	4.62165	19.18868	0.27503
	200	3.268	27.26682	4.10959
	002	2.6615	33.6467	14.3366
	211	2.562116	34.99313	100
	220	2.310825	38.94357	5.66891
	112	2.306397	39.02136	15.46014
	310	2.066865	43.76303	22.28675
	202	2.063694	43.83373	17.9768

FeSn	hkl	d (Angstrom)	2 theta	Intensity
	100	4.588202	19.3299	13.12248
	001	4.448	19.94531	3.54847
	101	3.193627	27.91452	95.28541
	110	2.649	33.81023	72.7144
	200	2.294101	39.23906	13.50113
	111	2.275956	39.56489	28.70489
	002	2.224	40.52923	39.44564
	201	2.038892	44.39513	100
	102	2.001286	45.27515	1.72133

Fe3Sn2	hkl	d (Angstrom)	2 theta	Intensity
	003	6.615	13.40389	53.33631
	101	4.507099	19.72512	12.6593
	012	4.19425	21.21284	8.99142
	104	3.38419	26.37278	5.28521
	006	3.3075	26.99571	8.52909
	015	3.012811	29.69404	10.0934
	110	2.672	33.58688	16.88647
	113	2.477517	36.31163	29.72485
	107	2.417483	37.24608	7.39325
	021	2.298447	39.252	52.45084
	202	2.253549	40.06714	0.18625
	009	2.205	40.9885	55.93992
	018	2.186362	41.35384	5.52045
	024	2.097125	43.19982	100
	116	2.078487	43.60693	5.55139
	205	1.999071	45.43396	85.76493
	10 10	1.823893	50.08248	0.00732

Fe5Sn3	hkl	d (Angstrom)	2 theta	Intensity
	100	3.654627	24.3353	6.26
	101	2.998699	29.76966	75.54763
	002	2.623	34.15561	16.59319
	102	2.130956	42.38215	82.80461
	110	2.11	42.82371	100
	200	1.827314	49.86445	0.67436

Fe3Sn	hkl	d (Angstrom)	2 theta	Intensity
	100	4.731963	18.73726	3.15711
	101	3.203246	27.829	27.8037
	110	2.732	32.75364	9.51678
	200	2.365982	38.00042	27.49752
	002	2.176	41.46391	27.25073
	201	2.078656	43.50207	100
	102	1.976987	45.86315	0.51447

Appendix B

Darwin Shape Factor Correction

The shape of a sample within the SQUID VSM detector coils will have a significant impact on the moment the coils can detect. This can be seen from the simple intuition that a detector coil cannot detect flux lines that close entirely within the dimensions of the coil (or, equivalently, they can only detect flux lines whose enclosed area is intersected by the coil). Since the geometry of flux lines varies greatly with the shape of the sample, and also, varies relative to the detector coils between the IP and OOP alignment, some thought has to be put in for correcting this effect.

The original theoretical simulations for different sample geometries and orientations were performed and tested by Quantum Design [140], though this was limited to discrete sample dimensions and vibration amplitudes. This work was then extended by E. Darwin [113] to a general form that could be applied to thin films of known area. To produce the true moment, the raw moment m should be adjusted by $\frac{m}{f_x}$ with f_x given by:

$$\begin{aligned} f_{\text{OOP}} &= (0.00613 \times A) + 1.04738 \\ f_{\text{IP}} &= (-0.00292 \times A) + 1.0504 \end{aligned} , \tag{B.1}$$

where A is the area of the film in mm^2.

Appendix C

Bumps Fitting

In Figure 5.5 and table 5.1 the results of a Bumps fitting are presented. Using DREAM, a Markov Chain Monte Carlo (MCMC) algorithm first introduced by J. A. Vrugt *et al.* [141, 142], the simulation of many thousands of potential fitting curves can be produced [124]. This allows for more details about the fitting parameters relationships to each other and their uncertainties to be extracted. Figures C.1, C.2 and C.3 show the best fit for the Fe_3Sn_2 film, the Mixed film, and the FeSn film respectively. Also shown are the statistical distribution on the fitting parameters as well as the correlation plot between M_S and D.

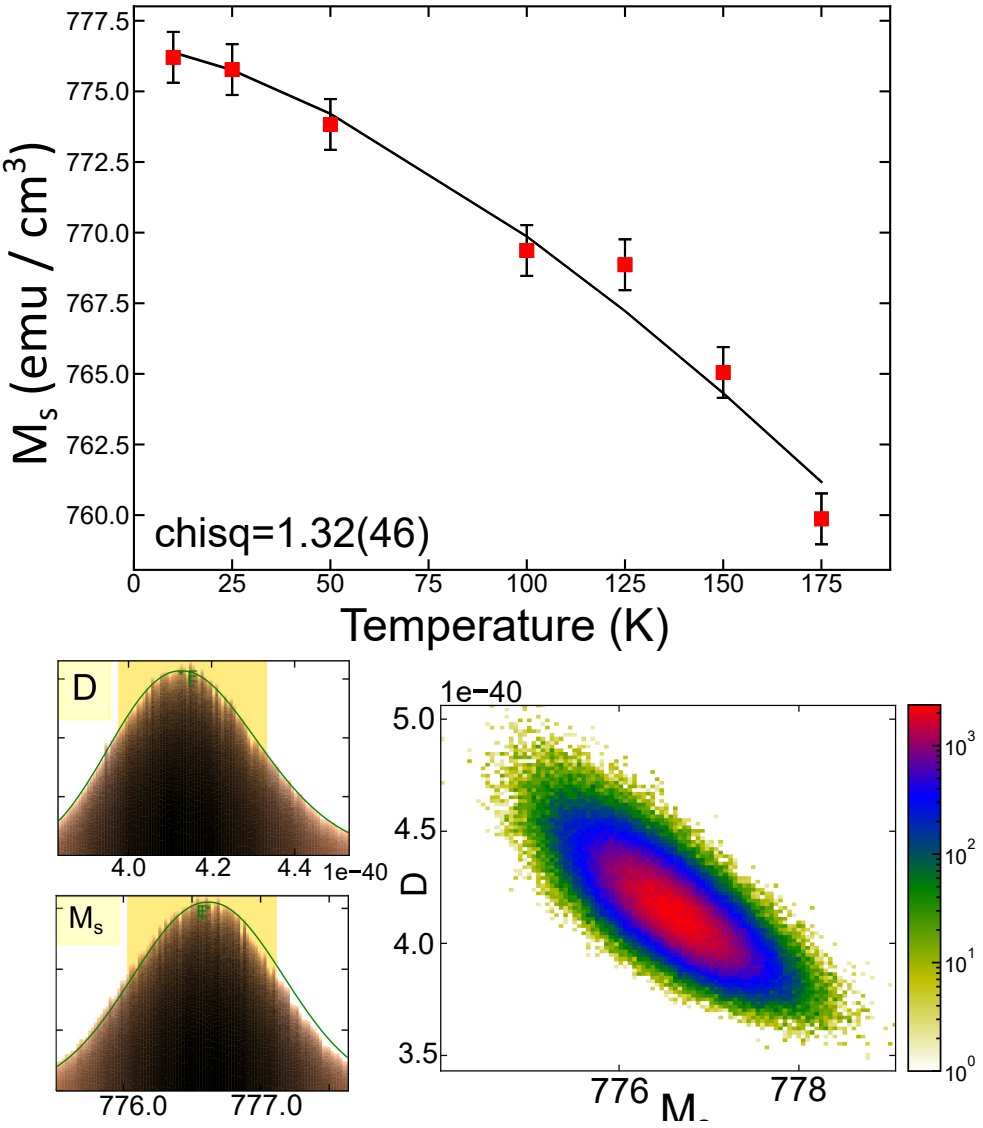

Figure C.1: Fitting of the Fe_3Sn_2 film's magnetisation vs temperature. Also shown are the simulated variable curves for D and M_s which provide the asymmetric uncertainties as well as the correlation between these fitting parameters.

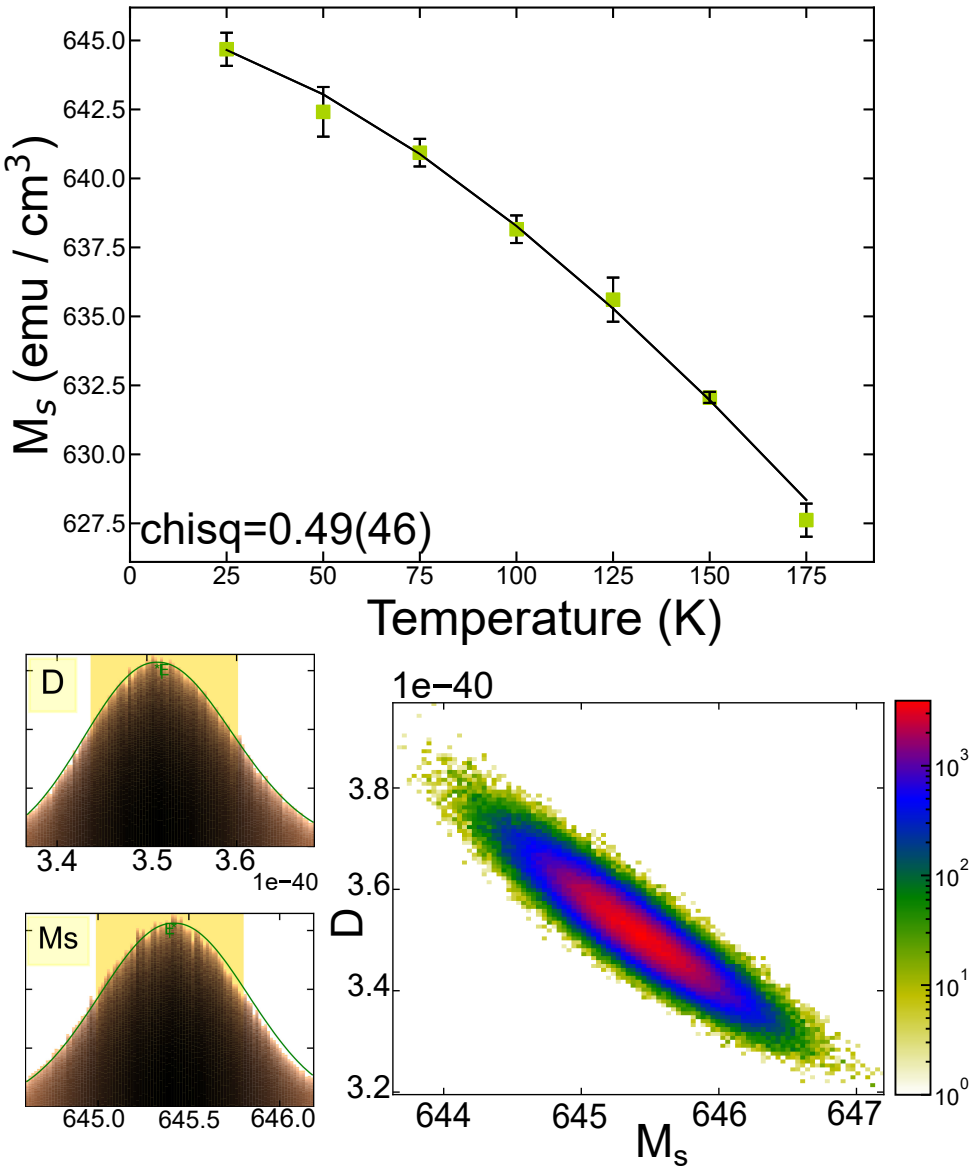

Figure C.2: Fitting of the mixed film's magnetisation vs temperature. Also shown are the simulated variable curves for D and M_s which provide the asymmetric uncertainties as well as the correlation between these fitting parameters.

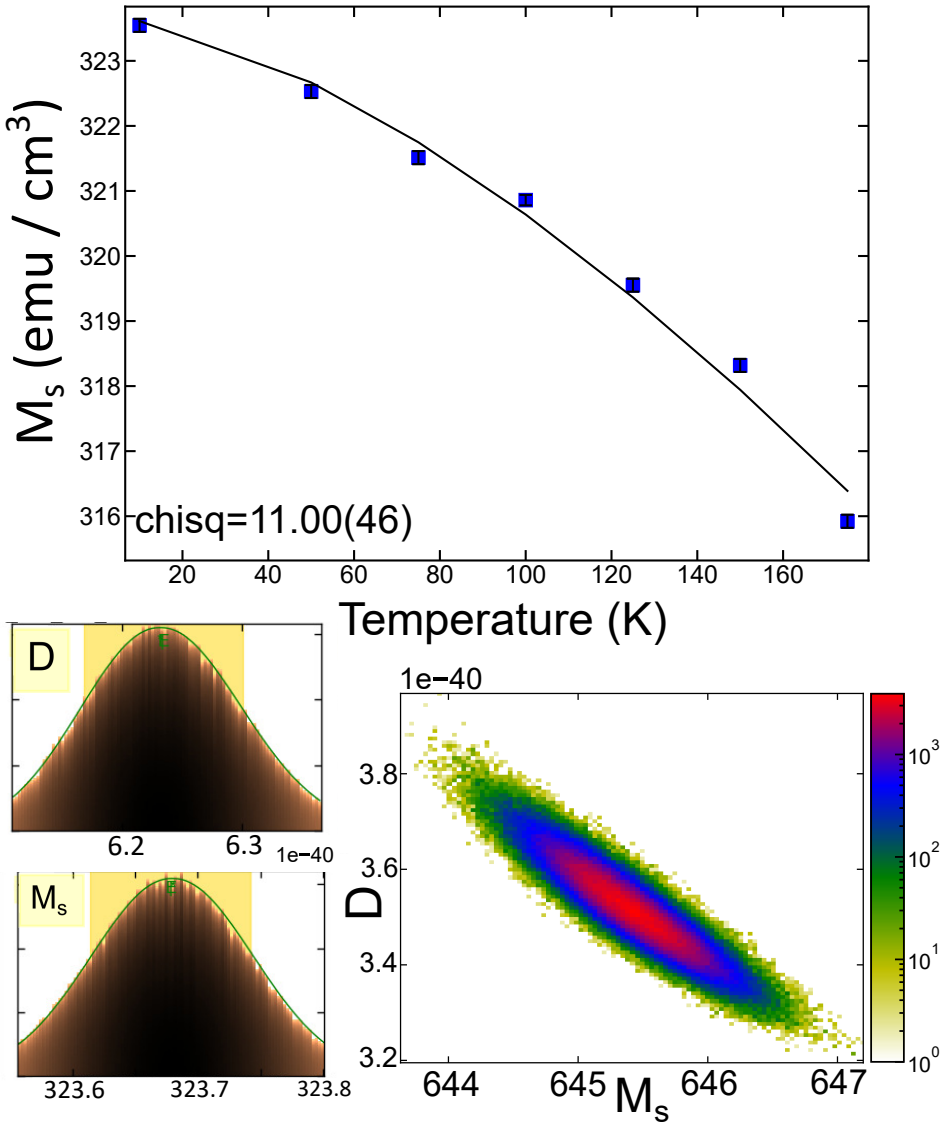

Figure C.3: Fitting of the FeSn film's magnetisation vs temperature. Also shown are the simulated variable curves for D and M_s which provide the asymmetric uncertainties as well as the correlation between these fitting parameters.

Appendix D

A Supplementary Poem

The Experimentalist

by Callum Brennan-Rich

An email came down, from up on high
I read it through thrice, and gave a sigh
The professors are having ideas again
Of what I should do, when will it all end
I guess I should try their latest scheme
Though first I'll need to repair that machine

First get a postdoc, from where they lurk
They'll have experience of how this thing works
I'll need some advice from the head engineer,
But he isn't free until June, next year
I really can't wait around that long,
I think I'll just start, I mean what can go wrong?

Well the piping is easy, just follow the labels
'Tis a pity that nobody marked up the cables
The computer's not starting, the power's not on
The interlock's tripping, the gauges are gone
I can scavenge some more, that's just a small bump
A bigger issue is: there's no roughing pump.

Alright I'm back, a pump I did find,
It took me three days to locate the right kind
It's all hooked up now and pumping away
But there's air in the system, the spectrometers say
I'll get round to fixing that, start of next week,
But just now the water pipes have started to leak.

So half the pipes were irregularly sized,
But now they're replaced, the leaks will subside
Next all the internals will need a sand blast
To clean the deposits from three decades past
I can open up soon, it should be a cinch,
Except all the machine's motors aren't moving an inch

When I pried the thing open, I screamed to see
The main thermocouple was broken in three
The list of air leaks is impossibly vast
The stepper motors have all stepped their last
The magnetron casings are cracked or smashed
And to top it all off, the software has crashed

I stumbled back home, my soul was in strife
At that horrid machine, the white whale of my life
Well at least they can't say that I failed to try
To the original email I sent a reply:
"This is the last you'll hear from me
"I'm off to do a theoretical degree"

References

[1] World Health Organisation, "WHO COVID-19 dashboard," 2025.

[2] British Academy (2021), "The COVID decade: Understanding the long-term societal impacts of COVID-19," tech. rep., The British Academy, 2021.

[3] F. Duarte, "Number of ChatGPT Users," 2025.

[4] D. Milmo, "ChatGPT reaches 100 million users two months after launch," 2023.

[5] J. Howarth, "Most Visited Websites In The World (July 2025)," 2025.

[6] A. Singla *et al.*, "How companies are organizing their gen AI deployment-and who's in charge," 2025.

[7] E. Amdur, "10 Areas Already Being Heavily Influenced By A.I.," 2024.

[8] S. Chen, "How much energy will AI really consume? The good, the bad and the unknown," *Nature*, March 2025.

[9] I. Wright, "ChatGPT Energy Consumption Visualized," 2025.

[10] C. Criddle and K. Bryan, "AI boom sparks concern over Big Tech's water consumption," 2024.

[11] K. Crawford, "Generative AI's environmental costs are soaring - and mostly secret," *Nature*, February 2024.

[12] P. Li *et al.*, "Making AI Less 'Thirsty'," *Communications of the ACM*, vol. 68, July 2025.

[13] I. ˇ Zutić, J. Fabian, and S. Sharma, "Spintronics: Fundamentals and applications," *Review of Modern Physics*, vol. 76, pp. 323–410, April 2004.

[14] M. N. Baibich *et al.*, "Giant Magnetoresistance of (001)Fe/(001)Cr Magnetic Superlattices," *Physical Review Letters*, vol. 61, pp. 2472–2475, November 1988.

[15] G. Florio, "Applications of Magnetic Materials," *Encyclopedia of Smart Materials*, vol. 5, pp. 24–31, 2022.

[16] A. Hirohata, "MRAM makes its mark," *Nature Electronics*, pp. 832–833, December 2022.

[17] Z. Guo *et al.*, "Spintronics for Energy- Efficient Computing: An Overview and Outlook," *Proceedings of the IEEE*, vol. 109, no. 8, pp. 1398–1417, 2021.

[18] C. Wang *et al.*, "Thin-film transistors for emerging neuromorphic electronics: fundamentals, materials, and pattern recognition," *Journal of Materials Chemistry C*, vol. 13, June 2021.

[19] S. Sakthinathan *et al.*, "A Review of Thin-Film Growth, Properties, Applications, and Future Prospects," *MDPI Processes*, vol. 13, p. 587, February 2025.

[20] C. Ha and Y. Chung, "Thin films as practical quantum materials: A status quo and beyond," *APL Materials*, vol. 12, p. 120901, December 2024.

[21] D. Hong *et al.*, "Molecular beam epitaxy of the magnetic Kagome metal FeSn on $LaAlO_3$ (111)," *AIP Advances*, vol. 10, no. 105017, 2020.

[22] H. Giefers and M. Nicol, "High pressure X-ray diffraction study of all Fe–Sn intermetallic compounds and one Fe–Sn solid solution," *Journal of Alloys and Compounds*, vol. 422, pp. 132–144, 2006.

[23] G. L. Caer, B. Malaman, and B. Roques, "Mössbauer effect study of Fe_3Sn_2," *Journal of Physics F: Metal Physics*, vol. 8, no. 2, p. 323, 1978.

[24] O. Hartmann and R. Wäppling, "Muon Spin Precession in the Hexagonal Antiferromagnet FeSn," *Physica Scripta*, vol. 35, April 1987.

[25] P. Kienzle, J. Krycka, N. Patel, and I. Sahin, "Hyperspy (v0.9.2)," 2025.

[26] S. Simon, *The Oxford Solid State Basics.* Oxford University Press, Usa, 2013.

[27] Ashcroft and Mermin, *Solid State Physics.* Holt-Saunders, 1976.

[28] C. Kittel, *Kittel's Introduction to Solid State Physics.* John Wiley and Sons, 1953.

[29] S. Blundell, *Magnetism in Condensed Matter.* Oxford University Press, Usa, 2014.

[30] J. Binney and D. Skinner, *The Physics of Quantum Mechanics.* Cappella Archive, 2008.

[31] E. C. Stoner, "Collective electron ferromagnetism," *Proceedings of the Royal Society of London*, vol. A 165, pp. 372–414, 1938.

[32] S. Parkin, M. Hayashi, and L. Thomas, "Magnetic Domain-Wall Racetrack Memory," *Science*, vol. 320, pp. 190–194, April 2008.

[33] P. Weiss, "L'hypothèse du champ molèculaire et la propriètè ferromagnètique," *Journal of Physics: Theories and Applications*, vol. 6, no. 1, pp. 661–690, 1907.

[34] R. Dally *et al.*, "Isotropic Nature of the Metallic Kagome Ferromagnet Fe_3Sn_2 at High Temperatures," *Crystals*, vol. 11, p. 307, March 2021.

[35] B. Raquet *et al.*, "Electron-magnon scattering and magnetic resistivity in 3d ferromagnets," *Physical Review B*, vol. 66, no. 024433, 2002.

[36] N. Kumar *et al.*, "Magnetotransport as a diagnostic of spin reorientation: Kagome ferromagnet as a case study," *Physical Review B*, vol. 100, p. 214420, December 2019.

[37] M. Hoffmann *et al.*, "Antiskyrmions stabilized at interfaces by anisotropic Dzyaloshinskii-Moriya interactions," *Nature Communications*, vol. 8, pp. 127–138, February 2017.

[38] T. H. R. Skyrme, "A non-linear field theory," *Proceedings of the Royal Society of London. Series A. Mathematical and Physical Sciences*, vol. 260, pp. 127–138, February 1961.

[39] A. N. Bogdanov and U. K. Rößler, "Chiral symmetry breaking in magnetic thin films and multilayers," *Phys. Rev. Lett.*, vol. 87, July 2001.

[40] U. K. Rößler, A. Bogdanov, and C. Pfleiderer, "Spontaneous skyrmion ground states in magnetic materials," *Nature*, vol. 442, pp. 797–801, August 2006.

[41] S. Mühlbauer *et al.*, "Skyrmion lattice in a chiral magnet," *Science*, vol. 323, pp. 915–919, February 2009.

[42] N. Romming *et al.*, "Writing and Deleting Single Magnetic Skyrmions," *Science*, vol. 341, pp. 636–639, August 2013.

[43] S. Möuhlbauer *et al.*, "Skyrmion lattice in a chiral magnet," *Science*, vol. 323, pp. 915–919, 2009.

[44] X. Yu *et al.*, "Real-space observation of a two-dimensional skyrmion crystal," *Nature*, vol. 465, pp. 901–904, 2010.

[45] S. Li, X. Wang, and T. Rasing, "Magnetic skyrmions: Basic properties and potential applications," *Interdiciplinary Materials*, vol. 2, pp. 260–289, March 2023.

[46] I. Dzyaloshinsky, "A thermodynamic theory of 'weak' ferromagnetism of antiferromagnetics," *J. Phys. Chem. Solids*, vol. 4, p. 241, 1958.

[47] T. Moriya, "Anisotropic superexchange interaction and weak ferromagnetism," *Phys. Rev.*, vol. 120, p. 91, 1960.

[48] H. Yang *et al.*, "Anatomy of Dzyaloshinskii-Moriya Interaction at $\mathrm{Co/Pt}$ Interfaces," *Phys. Rev. Lett.*, vol. 115, p. 267210, December 2015.

[49] A. Fakhredine, A. Wawro, and C. Autieri, "Huge Dzyaloshinskii-Moriya interactions in Pt/Co/Re thin films," *Journal of Applied Physics*, vol. 135, p. 035303, January 2024.

[50] C. Ma *et al.*, "Electric Field-Induced Creation and Directional Motion of Domain Walls and Skyrmion Bubbles," *Nano Lett.*, vol. 19, no. 1, pp. 353–361, 2019.

[51] S. Woo *et al.*, "Observation of room-temperature magnetic skyrmions and their current-driven dynamics in ultrathin metallic ferromagnets," *Nature Materials*, vol. 15, pp. 501–506, 2016.

[52] N. Nagaosa and Y. Tokura, "Topological properties and dynamics of magnetic skyrmions," *Nat. Nanotech*, vol. 8, p. 899, 2013.

[53] M. Trukhanova, "Skyrmion–electron interaction in the separated spin-up and spin-down quantum hydrodynamics approach," *Progress of Theoretical and Experimental Physics*, vol. 2020, no. 1, 2020.

[54] K. Zeissler *et al.*, "Diameter-independent skyrmion Hall angle observed in chiral magnetic multilayers," *Nature Communications*, vol. 11, 2020.

[55] A. Fert *et al.*, "Skyrmions on the track," *Nat. Nano*, vol. 8, pp. 152–156, 2013.

[56] R. Tomasello *et al.*, "A strategy for the design of skyrmion racetrack memories," *Sci. Rep.*, vol. 4, p. 6784, November 2014.

[57] A. Fert, N. Reyren, and V. Cros, "Magnetic skyrmions: advances in physics and potential applications," *Nature Reviews Materials*, vol. 2, 2017.

[58] X. Hu *et al.*, "Magnetic skyrmions and domain walls for logical and neuromorphic computing," *Neuromorphic Computing and Engineering*, vol. 3, p. 022003, May 2023.

[59] Z. Khodzhaev and J. Incorvia, "Voltage-controlled skyrmion manipulation chambers for neuromorphic computing," *Neuromorphic Computing and Engineering*, vol. 35, p. 101220, March 2025.

[60] K. Song *et al.*, "Skyrmion-based artificial synapses for neuromorphic computing," *Nature Electronics*, vol. 3, pp. 148–155, March 2020.

[61] T. Yokouchi *et al.*, "Pattern recognition with neuromorphic computing using magnetic field-induced dynamics of skyrmions," *Science Advances*, vol. 8, September 2022.

[62] G. Trumpy and E. Both, "Mössbauer-Effect Studies of Iron-Tin Alloys," *Physical Review B*, vol. 2, November 1970.

[63] K. Kumar, P. Wollants, and L. Delaey, "Thermodynamic evaluation of Fe-Sn phase diagram," *Calphad*, vol. 20, no. 2, pp. 139–149, 1996.

[64] T. Piesk, "Tiling 3-6 simple." https://commons.wikimedia.org/wiki/File:Tiling_-6_.svg. Accessed: 2025-04-04. Reproduced under GNU Free Documentation Licence.

[65] L. A. Fenner, A. A. Dee, and A. S. Wills, "Non-collinearity and spin frustration in the itinerant kagome ferromagnet Fe_3Sn_2," *Journal of Physics: Condensed Matter*, vol. 21, October 2009.

[66] O. Nial, "X-Ray Studies on Binary Alloys of Tin with Transition Metals," *Svensk Kemisk Tidskrift*, vol. 59, pp. 165–170, 1947.

[67] S. Saxena, R. P. Chaudhary, and S. Shukla, "Stanene: Atomically Thick Free-standing Layer of 2D Hexagonal Tin," *Scientific Reports*, vol. 6, August 2016.

[68] N. J. Ghimire and I. I. Mazin, "Topology and correlations on the kagome lattice," *Nature Materials*, vol. 19, pp. 137–138, December 2020.

[69] L. Häggström, T. Ericsson, R. Wäppling, and K. Chandra, "Studies of the Magnetic Structure of FeSn Using the Mössbauer Effect," *Physica Scripta*, vol. 11, no. 1, p. 47, 1975.

[70] B. Malaman, B. Roques, A. Courtois, and J. Protas, "Structure cristalline du stannure de fer Fe_3Sn_2," *Acta Crystallographica Section B: Structural Science, Crystal Engineering and Materials*, vol. 32, pp. 1348–1351, 1976.

[71] B. Malaman, D. Fruchart, and G. L. Caer, "Magnetic properties of Fe_3Sn_2. II. Neutron diffraction study (and Mössbauer effect)," *Journal of Physics F: Metal Physics*, vol. 8, no. 11, p. 2389, 1978.

[72] G. L. Caer, B. Malaman, L. Häggström, and T. Ericsson, "Magnetic properties of Fe_3Sn_2. III. A 119Sn Mössbauer study," *Journal of Physics F: Metal Physics*, vol. 9, no. 9, p. 1905, 1979.

[73] T. Okubo, S. Chung, and H. Kawamura, "Multiple-q States and the Skyrmion Lattice of the Triangular-Lattice Heisenberg Antiferromagnet under Magnetic Fields," *Physical Review Letters*, vol. 108, p. 017206, January 2018.

[74] A. O. Leonov and M. Mostovoy, "Multiply periodic states and isolated skyrmions in an anisotropic frustrated magnet," *Nature Communications*, vol. 6, p. 8257, September 2015.

[75] S. Hayami, S. Lin, and C. D. Batista, "Bubble and skyrmion crystals in frustrated magnets with easy-axis anisotropy," *Physical Review B*, vol. 93, p. 184413, May 2016.

[76] M. Periero *et al.*, "Topological excitations in a kagome magnet," *Nature Communications*, vol. 5, p. 4815, 2014.

[77] Z. Hou *et al.*, "Observation of Various and Spontaneous Magnetic Skyrmionic Bubbles at Room Temperature in a Frustrated Kagome Magnet with Uniaxial Magnetic Anisotropy," *Advanced Materials*, vol. 29, June 2017.

[78] Z. Hou *et al.*, "Current-Induced Helicity Reversal of a Single Skyrmionic Bubble Chain in a Nanostructured Frustrated Magnet," *Advanced Materials*, vol. 32, January 2020.

[79] Z. Hou *et al.*, "Current-Induced Reversible Split of Elliptically Distorted Skyrmions in Geometrically Confined Fe_3Sn_2 Nanotrack," *Advanced Science*, vol. 10, January 2023.

[80] Q. Du *et al.*, "Room-Temperature Skyrmion Thermopower in Fe_3Sn_2," *Advanced Quantum Technologies*, vol. 3, pp. 638–642, September 2020.

[81] D. Kong *et al.*, "Strain Engineering of Magnetic Anisotropy in the Kagome Magnet Fe_3Sn_2," *Physical Review B*, vol. 19, February 2025.

[82] L. Kong, J. Tang, *et al.*, "Observation of hybrid magnetic skyrmion bubbles in Fe_3Sn_2 nanodisks," *Physical Review B*, vol. 107, May 2023.

[83] J. Tang *et al.*, "Lorentz transmission electron microscopy for magnetic skyrmions imaging," *Chinese Physics B*, vol. 28, p. 087503, July 2019.

[84] A. D. Yaghjian, "Maxwell's Derivation of the Lorentz Force from Faraday's Law," *Progress In Electromagnetics Research*, vol. 93, pp. 35–42, 2020.

[85] N. A. Sinitsyn, "Semiclassical theories of the anomalous Hall effect," *Journal of Physics: Condensed Matter*, vol. 20, no. 2.

[86] S. C. Holb_k *et al.*, "Unconventional superconductivity protected from disorder on the kagome lattice," *Physical Review B*, vol. 108, October 2023.

[87] L. Ye *et al.*, "Massive Dirac fermions in a ferromagnetic kagome metal," *Nature*, vol. 555, pp. 638–642, March 2018.

[88] M. Kang, L. Ye, S. Fang, *et al.*, "Dirac fermions and flat bands in the ideal kagome metal FeSn," *Nature Materials*, vol. 19, February 2020.

[89] Z. Lin *et al.*, "Dirac fermions in antiferromagnetic FeSn kagome lattices with combined space inversion and time-reversal symmetry," *Physical Review B*, vol. 102, October 2020.

[90] M. Han *et al.*, "Evidence of two-dimensional flat band at the surface of antiferromagnetic kagome metal FeSn," *Nature Communications*, vol. 102, p. 5345, September 2021.

[91] D. Multer *et al.*, "Imaging real-space flat band localization in kagome magnet FeSn," *Communications Materials*, vol. 102, February 2023.

[92] T. Kida *et al.*, "The giant anomalous Hall effect in the ferromagnet Fe_3Sn_2-a frustrated kagome metal," *Journal of Physics: Condensed Matter*, vol. 23, p. 112205, March 2011.

[93] Q. Wang *et al.*, "Anomalous Hall effect in a ferromagnetic Fe_3Sn_2 single crystal with a geometrically frustrated Fe bilayer kagome lattice," *Physical Review B*, vol. 94, p. 075135, August 2016.

[94] Q. Du, Z. Hu, *et al.*, "Topological Hall Effect Anisotropy in Kagome Bilayer Metal Fe_3Sn_2," *Physical Review Letters*, vol. 129, p. 236601, November 2022.

[95] L. Wang *et al.*, "Orbital Magneto-Nonlinear Anomalous Hall Effect in Kagome Magnet Fe_3Sn_2," *Phys. Rev. Lett.*, vol. 132, p. 106601, March 2024.

[96] Y. Li *et al.*, "Magnetic-Field Control of Topological Electronic Response near Room Temperature in Correlated Kagome Magnets," *Physical Review Letters*, vol. 123, p. 196604, November 2019.

[97] E. Tang, J. Mei, and X. Wen, "High-Temperature Fractional Quantum Hall States," *Physical Review Letters*, vol. 106, p. 236802, June 2011.

[98] H. Inoue *et al.*, "Molecular beam epitaxy growth of antiferromagnetic Kagome metal FeSn, Appl. Phys. Lett," *Appl. Phys*, vol. 115, p. 072403, 2019.

[99] S. Cheng *et al.*, "Atomic layer epitaxy of kagome magnet Fe_3Sn_2 and Sn-modulated heterostructures," *APL Materials*, vol. 10, June 2022.

[100] Y. Satake *et al.*, "Fe-Sn nanocrystalline films for flexible magnetic sensors with high thermal stability," *Nature Scientific Reports*, vol. 9, p. 087503, March 2019.

[101] K. Khan *et al.*, "Intrinsic anomalous Hall effect in thin films of topological kagome ferromagnet Fe_3Sn_2," *Nanoscale*, vol. 14, June 2022.

[102] Z. H. D. Zhang and W. Mi, "Anomalous and topological Hall effects of ferromagnetic Fe_3Sn_2 epitaxial films with kagome lattice," *Applied Physics Letters*, vol. 120, June 2022.

[103] D. Khadkha *et al.*, "Anomalous Hall and Nernst effects in epitaxial films of topological kagome magnet Fe_3Sn_2," *Physical Review Materials*, vol. 4, p. 084203, August 2020.

[104] S. Gupta, "Electrically Switchable Ferromagnetic Josephson Junctions - Transfer report," *Leeds Internal Document*, March 2024.

[105] K. Oura, V. G. Lifshits, A. A. Saranin, A. V. Zotov, and M. Katayama, *Surface Science: An Introduction*. Berlin: Springer, 2003.

[106] R. Farrow, G. Harp, R. Marks, M. Toney, T. Rabedeau, D. Weller, and S. Parkin, "Epitaxial growth of Pt on basal-plane sapphire: a seed film for artificially layered magnetic metal structures," *Journal of Crystal Growth*, vol. 133, pp. 47–58, 1993.

[107] M. D. Rogers, "Growth of E-beam evaporated platinum," *White Rose Research Online*, 2020.

[108] P. Scherrer, "Bestimmung der größe und der inneren struktur von kolloidteilchen mittels röntgenstrahlen," *Nachrichten von der Gesellschaft der Wissenschaften zu Göttin, Mathematisch-Physikalische Klasse*, vol. 98, 1918.

[109] "International Tables for Crystallography," *H. ch*, vol. 5, no. 4, pp. 581–600, 2019.

[110] Tescan, "How Precession Enhances STEM Microscopy," 2025.

[111] S. Foner, "The vibrating sample magnetometer: Experiences of a volunteer (invited)," *Journal of Applied Physics*, vol. 79, p. 4740, 1996.

[112] A. Vettoliere, P. Silvestrini, and C. Granata, *Quantum Materials, Devices, and Applications*. Elsevier, 2023.

[113] E. Darwin, "Tuning Synthetic Antiferromagnetic and Ferromagnetic Multilayers for Hosting Skyrmions," *White Rose Research Online*, 2023.

[114] M. Banobre-Lopez *et al.*, "Magnetic properties of chromium (III) oxide nanoparticles," *Nanotechnology*, vol. 14, pp. 318–322, 2003.

[115] J. T. Batley, "Spin Transport in Lateral Spin Valves," *White Rose Research Online*, 2015.

[116] G. Williamson and W. Hall, "X-ray line broadening from filed aluminium and wolfram," *Acta Metallurgica*, vol. 1, 1953.

[117] H. Li *et al.*, "Spin-polarized imaging of the antiferromagnetic structure and field-tunable bound states in kagome magnet FeSn," *Scientific Reports*, vol. 12, no. 14525, 2022.

[118] C. Klewe *et al.*, "Static magnetic proximity effect in Pt/$Ni_{1-x}Fe_x$ bilayers investigated by x-ray resonant magnetic reflectivity," *Physical Review B*, vol. 93, 2016.

[119] S. Zhang *et al.*, "Coercivity induced by random field at ferromagnetic and antiferromagnetic interfaces," *Journal of Magnetism and Magnetic Materials*, pp. 198–199, 1999.

[120] H. T. Nembach *et al.*, "Linear relation between Heisenberg exchange and interfacial Dzyaloshinskii–Moriya interaction in metal films," *Nature Physics*, vol. 11, pp. 825–829, October 2015.

[121] J. B. Mohammadi *et al.*, "Reduced Exchange Interactions in Magnetic Tunnel Junction Free Layers with Insertion Layers," *ACS Applied Electronic Materials*, vol. 1, September 2019.

[122] L. Huang *et al.*, "Temperature gradient-driven motion of magnetic domains in a magnetic metal multilayer by entropic forces," *ArXiv*, June 2025.

[123] C. Lee *et al.*, "Spin wavepackets in the Kagome ferromagnet Fe_3Sn_2: Propagation and precursors," *Proceedings of the National Academy of Sciences*, vol. 120, p. e2220589120, May 2023.

[124] P. Kienzle, J. Krycka, N. Patel, , and I. Sahin, "Bumps (v0.9.2)," 2025.

[125] N. Osman and T. Moyo, "Temperature Dependence of Coercivity and Magnetization of $Sr_{1/3}Mn_{1/3}Co_{1/3}Fe_2O_4$ Ferrite Nanoparticles," *Journal of Superconductivity and Novel Magnetism*, vol. 29, pp. 361–366, November 2016.

[126] M. Mihalik *et al.*, "The Magnetic Properties of Single Crystal $SrCo_2Ti_2Fe_8O_{19}$ Compound," *Physics Procedia*, vol. 75, pp. 259–265, February 2015.

[127] C. Zener, "Classical Theory of the Temperature Dependence of Magnetic Anisotropy Energy," *Physical Review*, vol. 96, December 1954.

[128] E. Callen and H. Callen, "Magnetostriction, Forced Magnetostriction, and Anomalous Thermal Expansion in Ferromagnets," *Physical Review*, vol. 139, July 1965.

[129] K. Alshammari, "Scaling of Dzyaloshinskii-Moriya interaction with magnetization in Pt/Co(Fe)B/Ir multilayers," *Physical Review B*, vol. 104, p. 224402, December 2021.

[130] P. J. von Ranke *et al.*, "Understanding the inverse magnetocaloric effect in antiferro- and ferrimagnetic arrangements," *Journal of Physics: Condensed Matter*, vol. 21, p. 056004, January 2009.

[131] R. Srinivasan, R. D. Angelis, and B. H. Davis, "Alloy Formation in Pt-Sn-Alumina Catalysts: In Situ X-Ray Diffraction Study," *Journal of Catalysts*, vol. 106, pp. 449–457, 1987.

[132] W. Haynes, *CRC Handbook of Chemistry and Physics*. CRC Press/Taylor and Francis, 95 ed., 2014.

[133] C. Hurd, *The Hall Effect in Metals and Alloys.* Springer New York, 1 ed., 1972.

[134] N. Nagaosa *et al.*, "Anomalous Hall effect," *Reviews of Modern Physics*, vol. 82, pp. 1539–1592, May 2010.

[135] L. Wang *et al.*, "In-plane Hall effect in $Co_3Sn_2S_2$," *Physical Review B*, vol. 111, p. 054412, February 2025.

[136] T. R. McGuire and R. I. Potter, "Anisotropic Magnetoresistance in Ferromagnetic 3d Alloys," *IEEE Transactions of Magnetics*, vol. 11, pp. 1018–1038, July 1975.

[137] C. O. Avci *et al.*, "Unidirectional spin Hall magnetoresistance in ferromagnet/normal metal bilayers," *Nature Physics*, vol. 11, pp. 570–575, 2015.

[138] M. Trushin *et al.*, "Anisotropic magnetoresistance of spin-orbit coupled carriers scattered from polarized magnetic impurities," *Physical Review B*, vol. 80, p. 134405, October 2009.

[139] K. Momma and F. Izumi, "VESTA 3 for three-dimensional visualization of crystal, volumetric and morphology data," *Journal of Applied Crystallography*, pp. 1272–1276, 2011.

[140] "Accuracy of the reported moment: Sample shape effects," Tech. Rep. 1500-015, Quantum Design, 2010.

[141] J. A. Vrugt, C. G. H. Diks, and M. P. Clark, "Ensemble Bayesian model averaging using Markov Chain Monte Carlo sampling," *Environmental Fluid Mechanics*, vol. 8, pp. 579–595, October 2008.

[142] J. A. Vrugt and C. J. F. Ter Braak, "DREAM$_{(D)}$: an adaptive Markov Chain Monte Carlo simulation algorithm to solve discrete, noncontinuous, and combinatorial posterior parameter estimation problems," *Hydrology and Earth System Sciences*, vol. 15, pp. 3701–3713, April 2011.